Leibniz-Institut für
Astrophysik Potsdam

Spectroscopic Surface Brightness Fluctuations: Probing Bright Evolved Stars in Unresolved Stellar Populations

Martin Mitzkus

Leibniz-Institut für Astrophysik Potsdam (AIP)

Dissertation
zur Erlangung des akademischen Grades
Doktor der Naturwissenschaften (Dr. rer. nat.)
in der Wissenschaftsdisziplin Astrophysik

eingereicht an der
Mathematisch-Naturwissenschaftlichen Fakultät
der Universität Potsdam

Potsdam, den 4. Oktober 2017

Published online at the
Institutional Repository of the University of Potsdam:
URN urn:nbn:de:kobv:517-opus4-406327
http://nbn-resolving.de/urn:nbn:de:kobv:517-opus4-406327

Abstract

Galaxies evolve on cosmological timescales and to study this evolution we can either study the stellar populations, tracing the star formation and chemical enrichment, or the dynamics, tracing interactions and mergers of galaxies as well as accretion. In the last decades this field has become one of the most active research areas in modern astrophysics and especially the use of integral field spectrographs furthered our understanding. This work is based on data of NGC 5102 obtained with the panoramic integral field spectrograph MUSE. The data are analysed with two separate and complementary approaches: In the first part, standard methods are used to measure the kinematics and than model the gravitational potential using these exceptionally high-quality data. In the second part I develop the new method of surface brightness fluctuation spectroscopy and quantitatively explore its potential to investigate the bright evolved stellar population.

Measuring the kinematics of NGC 5102 I discover that this low-luminosity S0 galaxy hosts two counter rotating discs. The more central stellar component co-rotates with the large amount of H I gas. Investigating the populations I find strong central age and metallicity gradients with a younger and more metal rich central population. The spectral resolution of MUSE does not allow to connect these population gradients with the two counter rotating discs.

The kinematic measurements are modelled with Jeans anisotropic models to infer the gravitational potential of NGC 5102. Under the self-consistent mass-follows-light assumption none of the Jeans models is able to reproduce the observed kinematics. To my knowledge this is the strongest evidence evidence for a dark matter dominated system obtained with this approach so far. Including a Navarro, Frenk & White dark matter halo immediately solves the discrepancies. A very robust result is the logarithmic slope of the total matter density. For this low-mass galaxy I find a value of -1.75 ± 0.04, shallower than an isothermal halo and even shallower than published values for more massive galaxies. This confirms a tentative relation between total mass slope and stellar mass of galaxies.

The Surface Brightness Fluctuation (SBF) method is a well established distance measure, but due to its sensitive to bright stars also used to study evolved stars in unresolved stellar populations. The wide-field spectrograph MUSE offers the possibility to apply this technique for the first time to spectroscopic data. In this thesis I develop the spectroscopic SBF technique and measure the first SBF spectrum of any galaxy. I discuss the challenges for measuring SBF spectra that rise due to the complexity of integral field spectrographs compared to imaging instruments.

Since decades, stellar population models indicate that SBFs in intermediate-to-old stellar systems are dominated by red giant branch and asymptotic giant branch stars. Especially the later carry significant model uncertainties, making these stars a scientifically interesting target. Comparing the NGC 5102 SBF spectrum with stellar spectra I show for the first time that M-type giants cause the fluctuations. Stellar evolution models suggest that also carbon rich thermally pulsating asymptotic giant branch stars should leave a detectable signal in the SBF spectrum. I cannot detect a significant contribution from these stars in the NGC 5102 SBF spectrum.

I have written a stellar population synthesis tool that predicts for the first time SBF spectra. I compute two sets of population models: based on observed and on theoretical stellar spectra. In comparing the two models I find that the models based on observed spectra predict weaker molecular features. The comparison with the NGC 5102 spectrum reveals that these models are in better agreement with the data.

Zusammenfassung

Galaxien entwickeln sich auf kosmischen Zeitskalen. Um diese Entwicklung zu untersuchen und zu verstehen benutzen wir zwei verschiedene Methoden: Die Analyse der stellaren Population in Galaxien gibt Auskunft über die Sternentstehungsgeschichte und die Erzeugung von schweren Elementen. Die Analyse der Bewegung der Sterne gibt Auskunft über die dynamische Entwicklung, Interaktionen und Kollisionen von Galaxien, sowie die Akkretion von Gas. Die Untersuchung der Galaxienentwicklung ist in den letzten Jahrzehnten zu einem der wichtigsten Bereiche in der modernen Astrophysik geworden und die Einführung der Integral-Feldspektroskopie hat viel zu unserem heutigen Verständnis beigetragen.

Die Grundlage dieser Arbeit bilden Spektren von der Galaxie NGC 5102. Die Spektren wurden mit dem Integral-Feldspektrographen MUSE aufgenommen, welcher sich durch ein großes Gesichtsfeld auszeichnet. Die Daten werden mit zwei unterschiedlichen und sich ergänzenden Methoden analysiert: Im ersten Teil der Arbeit benutze ich etablierte Methoden um die Bewegung der Sterne zu vermessen und daraus das Gravitationspotential der Galaxie abzuleiten. Dieser Teil der Arbeit profitiert insbesondere von der ausgezeichneten Datenqualität. Im zweiten Teil der Arbeit entwickle ich erstmalig eine Methode für die Datenanalyse zur Extraktion von spektroskopischen Flächenhelligkeitsfluktuationen und quantifiziere deren Potential für die Untersuchung der hellen und entwickelten Sterne in Galaxien.

Durch die Analyse der Bewegung der Sterne in NGC 5102 habe ich entdeckt, dass diese S0 Galaxie aus zwei entgegengesetzt rotierenden Scheiben besteht. Durch die Kombination von meinen Ergebnissen mit publizierten Messungen der Rotation des H I Gases finde ich, dass dieses in die gleiche Richtung rotiert wie die innere Scheibe. Die Analyse der stellaren Population zeigt starke Gradienten im mittleren Alter und der mittleren Metallizität. Dabei ist die stellare Population im Zentrum jünger und hat eine höhere Metallizität. Die spektrale Auflösung von MUSE reicht nicht aus, um zu untersuchen, ob diese Gradienten in der Population mit den beiden entgegengesetzt rotierenden Scheiben verbunden sind.

Um das Gravitationspotential von NGC 5102 zu untersuchen, modelliere ich die gemessene Kinematik mit anisotropen Jeans Modellen. Keines der Modelle in dem ich annehme, dass die Massenverteilung der Verteilung des Lichts folgt, ist in der Lage die gemessene Kinematik zu reproduzieren. Nach meinem Wissen ist dies der bislang stärkste Hinweis auf Dunkle Materie, der mit dieser Methode in einer einzelnen Galaxie bisher erzielt worden ist. Durch das Hinzufügen einer sphärischen Dunkle Materie Komponente in Form eines Navarro, Frenk & White Halos kann die Diskrepanz zwischen Beobachtung und Modell gelöst werden. Fast modelunabhängig lässt sich die Steigung des logarithmischen Dichteprofils der gesamten (sichtbare und dunkle) Materie messen. In dieser massearmen Galaxie finde ich einen Wert von -1.75 ± 0.04. Diese Steigung ist flacher als die eines isotermen Dichteprofils und noch flacher als die Steigungen die für massereiche Galaxien veröffentlicht wurden. Diese Ergebnisse bestätigen eine bisher nur angedeutete Korrelation zwischen der Steigung des Dichteprofils und der stellaren Masse.

Flächenhelligkeitsfluktuationen (*Surface Brightness Fluctuations*, SBF) sind eine etablierte Methode zur Entfernungsbestimmung von Galaxien. SBF werden von den hellsten Sternen in einer Population verursacht und werden daher auch benutzt, um diese Sterne zu untersuchen. MUSE zeichnet sich durch die einmalige Kombination von einem großen Gesichtsfeld, mit einem guten räumlichen Sampling, und einer spektroskopischen Zerlegung des Lichts über das gesamte Gesichtsfeld aus. Dadurch kann die SBF Methode erstmalig auf Spektren angewendet werden. In dieser Arbeit entwickle ich die Methode der spektroskopischen SBF und messe das erste SBF Spektrum von einer Galaxie. Dabei diskutiere ich insbesondere die Herausforderungen die sich durch die Komplexität von Integral-Feldspektrographen verglichen mit bildgebenden Instrumenten für die SBF Methode ergeben.

Seit langem sagen stellare Populationsmodelle voraus, dass die SBF in stellaren Populationen, die älter

als etwa 0.5 Gyr sind, von Sternen auf dem roten und dem asymptotischen Riesenast erzeugt werden. Dabei ist insbesondere die Modellierung von Sternen des asymptotischen Riesenastes schwierig, weshalb diese wissenschaftlich besonders interessant sind. Der Vergleich des gemessenen SBF Spektrums von NGC 5102 mit Spektren von Riesensternen zeigt, dass das SBF Spektrum von Sternen mit dem Spektraltyp M dominiert wird. Nach allen Standardmodellen der stellaren Entwicklung sollten auch kohlenstoffreiche Riesensterne vom Spektraltyp C im SBF Spektrum sichtbar sein. Zu dem gemessenen SBF Spektrum tragen diese Sterne aber nicht signifikant bei.

Ich habe eine *stellar population synthesis* Software geschrieben, die zum ersten Mal auch SBF Spektrenmodelle berechnet. Mit dieser Software habe ich zwei verschiedene Versionen von Modellen berechnet: die eine basiert auf beobachteten Sternspektren, die andere auf theoretischen Modellen von Sternspektren. Die Version der SBF Modellspektren, die auf den beobachteten Sternspektren beruht, zeigt schwächere molekulare Absorptionsbanden. Der Vergleich mit dem SBF Spektrum von NGC 5102 zeigt, dass diese Modelle besser zu den Daten passen.

Contents

1 Introduction

Describing the evolution of galaxies is complicated and we are still far from having a complete and accepted theory of galaxy formation. However, many aspects of galaxy formation have been investigated and our knowledge has grown significantly. The wide spread use of integral field spectroscopy is advancing the galaxy evolution field.

To explain why galaxy evolution is so complex, it might be illustrative to compare to stellar evolution, as this is much better understood. The evolution of stars can be computed from a given initial mass, chemical composition and matter stratification (e.g. density and temperature stratification). In the following this mass evolves without further interactions with its surroundings with the only exceptions of mass-loss and binary evolution. Basically the evolution of a star can be calculated in isolation.

For galaxies such closed-box simulations cannot predict the galaxies we observe. The first reason is that galaxies evolve on cosmic time-scales and their evolution is tightly coupled to the evolution of the universe. The second reason is that galaxies do interact with their surroundings. Galaxies accrete gas from the circumgalactic and intergalactic medium and galactic winds drive matter out of the galaxy. Galaxies are observed to interact, in fact in the hierarchical galaxy formation picture large structures are formed by the merging of small structures. In our own Milky Way a number of small satellite galaxies, like Sagittarius and Aquarius, are currently accreted. There are the famous images of merging galaxies like the Antenna or the Mice galaxies. On the largest scales galaxy clusters are building-up by the accretion of hundreds to thousands of galaxies.

Also the processes inside galaxies are not well understood. We have not understood the details of the star formation. How is star formation triggered? What shapes the initial mass function? How does the stellar feedback impact the galaxy? What are the chemical yields of different stars and evolutionary phases? How does the mixing in the interstellar medium work? Many of these processes are chaotic, so that stochasticity is important in galaxy formation and evolution.

All these processes make galaxy evolution a challenging but very interesting subject. Every galaxy is an unique system, with an unique history and future. Coming back to the comparison with stellar evolution: While stars of a certain mass and chemical composition have a deterministic evolutionary path, galaxy evolutionary paths will always be understood as a statistical mean.

This chapter is structured as follows: In Section 1.1 a short summary of the ΛCDM cosmological model is given. Especially the tension between dark matter halo slopes in models and observations is discussed. In Section 1.2 the observational findings on multi-spin galaxies are discussed and what we learn from this class of objects about the merger and accretion history. In Section 1.3 the importance of stellar population modelling for interpreting the light of galaxies is described. Especially the uncertainties in modelling AGB stars and their significance for stellar population models is discussed. I conclude with the outline of the thesis in Section 1.4.

1.1 Cosmological model

In this section I will start with a short overview about the history of the most important observational findings that influenced our understanding of the evolution of the universe and our cosmological model. After that I will give a short summary of the evolution of the universe as predicted by the current standard model of cosmology, the ΛCDM model. In the last section I discuss the predicted dark matter halo slopes and present the observational results, focusing on the tension between observations and models, but also the disagreement between different observations.

1.1.1 Milestones in understanding the evolution of the Universe

Observing the night sky there are at least two morphologically distinct groups of objects: point-like light sources, i.e. stars like our own sun, and extended objects that have been termed nebulae. The stars in the sky are mostly confined to the Milky Way structure, our own Galaxy. But it was largely unknown whether the Milky Way is the universe or just a part of it. The key to answer this question was to reveal the nature of the nebulae. While some undoubtedly belong to the Milky Way, the nature of the spiral nebulae has been a long standing question in astronomy. This culminated in the so called Great Debate between Shapley and Curtis at the national Museum of Natural History in Washington D.C. in 1920. Shapley argued that the spiral nebulae are objects within the Milky Way while Curtis was arguing that these are objects outside but similar to the Milky Way.

This dispute was solved when Hubble (1925) used the period luminosity relation of Cepheid stars to measure the distance to the spiral nebulae M31 (Andromeda galaxy) and M33. The derived distances were so large that it was obvious that these two nebulae are objects outside the Milky Way. With the same technique Hubble (1929) showed that the recession velocities of galaxies are linearly correlated with their distance. This finding implies that the universe is expanding.

If the universe is expanding, this implies that it had to be smaller and therefore denser and hotter earlier. George Gamow's group in the 1940th worked out some important consequences. One question at that time was how the chemical composition of the universe has been set. Alpher et al. (1948) calculated the chemical mixture that was created when the hot plasma in the early universe cooled to temperatures where atoms became stable. This model failed to explain today's chemical composition of the universe, however, the idea of big bang (or primordial) nucleosynthesis was in place. Hoyle & Tayler (1964) realised that the He/H ratio in the Galaxy and local group galaxies is approximately constant and too high to be produced by stars. With this finding big bang nucleosynthesis started to be the accepted theory for the production of the primordial chemical abundance pattern. The idea that the universe consisted of a hot plasma that must have radiated like a black body, lead to the prediction of the Cosmic Microwave Background (CMB) radiation (Alpher & Herman, 1948). Fred Hoyle named this model, where the universe went through a singularity 'Hot Big Bang'.

It took more than a decade for the CMB radiation to be discovered. Penzias & Wilson (1965) found an excess radiation of 3.5 K temperature, that did not change with time or the direction the antenna pointed to. This was interpreted as the predicted CMB radiation by Dicke et al. (1965). The detection of the CMB is a major support for the big bang model. The isotropy of the CMB sets upper limits on the density fluctuations in the early universe. However, the fact that we observe structure in the universe today (i.e. stars, galaxies, galaxy groups and clusters) implies that at least at small scales the universe has to be anisotropic. Therefore it was expected that the CMB exhibits anisotropies. It took almost three decades to detect the anisotropy in the CMB using the COBE satellite (Smoot et al., 1992). The detected fluctuations are with $\Delta T/T \approx 10^{-5}$ very small, but important as they trace the density fluctuations at the time of recombination.

One of the important questions is what has caused the fluctuations that we see in the CMB and why is the CMB isotropic on large scales. The isotropy on large scales is unexpected, because regions in opposite directions could never have been in thermal contact. A very popular theory that solves this problem is the inflation theory proposed by Guth (1981). This theory predicts a short time of exponential growth of the universe. During this growth quantum fluctuations in the vacuum energy would have been grown to macroscopic scales and are the seeds for structure formation in the universe.

In the late 1990th two teams independently observed that the relation between the distance, measured from the luminosity of Supernovae (SNe) of type Ia, and the redshift of galaxies indicates an accelerating expansion of the universe (Perlmutter et al., 1999; Riess et al., 1998). This is the first observational evidence that we need a cosmological constant Λ (also called dark energy) in the equations of general relativity to describe the universe.

Zwicky (1933) was among the earliest to find ob-

servational evidence for dark matter (DM). He believed DM to be normal baryonic matter that is not radiating. Nowadays we still don't know the nature of the DM, but there is a vast amount of evidence for it's existence and it's nature is most likely not baryonic. Zwicky (1933) estimated the mass of the Coma cluster via the virial theorem from measured velocities of the individual galaxies. He concluded that the mass of the cluster has to be 400 times larger than the luminous mass inside the galaxies in order to be stable. While the numbers turned out to be wrong, the conclusion that the majority of mass needs to be dark was right. A similar analysis has been done by Smith (1936) for the Virgo cluster.

The impact of galaxy rotation curves on the question of DM in galaxies became famous with the work of Rubin & Ford (1970). While galaxy rotation curves have been measured out to large distances before in H I (e.g. Babcock, 1938), Rubin & Ford (1970) improved the quality by measuring Hα velocities of H II regions in M31 out to 110 arcmin. These measurements showed that the mass to light ratio increases systematically with radius and thus hints at a DM component in galaxies. Nowadays there are some other lines of evidence for DM: lensing studies predict mass to light ratios that cannot be reproduced with stellar mass to light ratios, the structure we see in the universe today can only form if we allow for a DM component that is more structured than the CMB anisotropies and the big bang nucleosynthesis needs considerable DM fractions in order to predict the observed He/H ratio.

1.1.2 The ΛCDM cosmology

The currently standard cosmological model is the ΛCDM model. It is based on Einstein's theory of general relativity and the principle that the universe is homogeneous and isotropic on large scales (cosmological principle). Under these assumptions the universe can only expand or collapse. The size of the universe is parametrized by the scale factor $a(t)$. The evolution of the scale factor is described by the two Friedmann equations. The Friedmann equations have a few free parameters that need to be determined from observations. In order to account for the accelerated expansion of the universe a cosmological constant Λ is added. We also need a model for the nature of the DM, currently the favoured one is the cold dark matter (CDM). Here cold means that the kinetic energy of the DM particle is negligible compared to its rest energy. As already mentioned above an inflation period is included in the model.

The structure of the universe is thought to be seeded by quantum fluctuations in the vacuum energy. These fluctuations are assumed to be Gaussian distributed and grow in size during a short phase of exponential expansion – the period of inflation. After this period these gravitational instabilities grow, because regions that are slightly over-dense attract matter from the surrounding under-dense regions. The growth of the overdensities is characterised by the density contrast $\Delta\rho/\rho$, with $\Delta\rho$ the difference between the density and the mean matter density ρ. As long as $\Delta\rho/\rho \ll 1$ the perturbations grow in size due to the expansion of space. Once $\Delta\rho/\rho > 1$ the region becomes dominated by self-gravity and starts to collapse (this is the non-linear regime of structure formation). The DM halo is stabilised via violent relaxation. This process is scale free and causes DM haloes to have an universal structure.

Before the recombination the radiation and the baryonic matter where strongly coupled by the radiation pressure. This radiation pressure was counteracting the gravitational forces and preventing the baryonic matter from clumping. After about 380 000 years electrons and protons recombined and formed the atoms. This suddenly removed the radiation pressure from the baryonic matter and the dominant force was the gravitation, dominated by the structure of the DM. So the baryonic matter settled in the DM potential.

At some point the cooling gas in the DM potential may become dominated by self-gravity. If cooling is efficient the cloud fragments and forms stars. Usually the baryonic matter has some non-zero angular momentum and while falling into the DM halo this causes the baryonic gas to settle in a disc. The first simulations indicated that cooling is very efficient and therefore star-formation is very efficient. This is however, in conflict with observations that show that only a small fraction of the baryonic matter is found in stars or cold gas. Therefore feedback mechanisms are needed to prevent the gas from cooling too efficiently. Two main feedback processes are discussed: SN and Active Galactic Nuclei (AGN) feedback. The role of the feedback is to reheat the gas and drive galactic winds. However, the details of many baryonic processes are very complicated and theoretically not well understood. We still have a poor understanding of the initial mass function of stars, we cannot predict the fraction of gas that forms stars or the time scales involved. And also the efficiencies of feedback mechanisms are debated.

Once stars have been formed, they start producing heavy elements and enrich the interstellar and also the intergalactic medium. The two main sources are SNe of type II in young populations and of type Ia in older populations.

The ΛCDM model needs six free parameters (among them the mass density of baryonic and dark matter and the amplitude of the temperature fluctuations) to describe the CMB power spectrum. The newest measurement of the CMB by the Planck satellite shows excellent agreement with this model (Planck Collaboration et al., 2016). The derived values put strong constraints on the baryonic and dark matter density in the universe. Also the galaxy distribution on large scales is in good agreement with the cosmological model (Percival et al., 2001; Doroshkevich et al., 2004).

1.1.3 Dark matter halo slopes

On small scales (galaxy sizes) some observations and predictions by the ΛCDM model are in tension. The most famous cases are the 'missing satellite' problem (Klypin et al., 1999; Moore et al., 1999b), i.e. the number of satellite galaxies predicted is an order of magnitude higher than those that are observed. The 'too big to fail' problem describes that ΛCDM models predict satellite haloes to be much more massive than observed. This was first found for Milky Way satellites (Boylan-Kolchin et al., 2011) and later confirmed for field dwarf galaxies (Papastergis et al., 2015). The problem I discuss in more detail is the 'cusp vs core' discrepancy. While simulations predict DM haloes with inner density $\rho \propto r^{\gamma}$ and $\gamma = -1$, so called cusps, observations find a much broader range of values, from $\gamma = 0$ (DM cores) to $\gamma < -1$.

DM only simulations have shown that the formation of DM haloes results in roughly universal profiles that are independent of the halo mass. The currently most popular parametrization is the so called NFW profile, named after the first letters of names of the discovering authors (Navarro, Frenk & White, 1996). These authors proposed a halo profile of the form $\rho \propto \frac{1}{(r/r_s)(1+r/r_s)^2}$, with $\rho \propto r^{-1}$ at small radii and $\rho \propto r^{-3}$ at large radii. However, other authors have suggested other slightly different profiles, e.g. Moore et al. (1999a) $\rho \propto \frac{1}{(r/r_s)^{1.5}(1+[r/r_s]^{1.5})}$. All these simulations agree on the fact that the predicted DM halo slope is cuspy. In detail the DM haloes are not universal, because of the phase-space-density relation (e.g. Taylor & Navarro, 2001) and the halo concentration-mass relation (e.g. Bullock et al., 2001).

All these simulations however, neglect the fact that in real galaxies the baryonic matter plays a role. Baryonic matter can cool efficiently and therefore condense to high densities. This means that the gravitational potential in the centres of galaxies is dominated by the baryonic matter and the DM reacts to the change in the gravitational potential. This process has been studied in analytical models (e.g. Cardone & Sereno, 2005) or via the 'adiabatic compression' parametrization (e.g. Gnedin et al., 2004) in simulations. A self-consistent numerical simulation is challenging, because the relevant scales of baryonic physics are hardly resolved in cosmological simulations (e.g. Duffy et al., 2010). In an N-body and smoothed particle hydrodynamic simulation Di Cintio et al. (2014) find that the inner halo slope depends on the halo mass of the galaxy.

Much observational effort has been put into measuring the inner DM halo slope in dwarf galaxies. These observations use H I and Hα rotation curves to constrain the halo slope and find logarithmic inner halo slopes larger −1 up to constant density profiles, i.e. DM cores (Moore, 1994; Flores & Primack, 1994; de Blok & McGough, 1997; de Blok et al., 2001b,a; de Blok & Bosma, 2002; Weldrake et al., 2003; Kuzio de Naray et al., 2006, 2008; Oh et al., 2008, 2015). At face value these measurements contradict CDM models, unless strong baryonic feedback processes are involved. However, also biases in the measurements are discussed. Spekkens et al. (2005) find that the distribution of measured halo slopes (the mean value of their sample is −0.2) of their sample of 165 low mass galaxies is compatible with an intrinsic halo slope of −0.5 as well as −1 (NFW like). Adams et al. (2014) compare gas and stellar velocity curves, finding that gas tracers tend to predict slightly more cored haloes than stellar tracers on average. However, the difference is not significant. For the ATLAS^{3D} early type galaxy sample (Cappellari et al., 2011) the fitting of the stellar kinematics yields a logarithmic slope of −1.55 for contacted halo models (Cappellari et al., 2013).

1.2 Accretion and mergers

Galaxies grow their baryonic mass via accretion of gas and satellite galaxies (minor mergers) and via major mergers. While major merger are violent events that destroy the structure of both galaxies to form a new object, gas accretion and minor mergers are smooth events (at least for the more massive galaxy). The kinematics of a galaxy are interesting because they trace the potential and they can reveal insights about the formation of the system. In a closed box or secular evolution picture for galaxies it is impossible to have different components with misaligned angular momentum vectors. So these multi-spin galaxies (Rubin, 1994) can reveal interesting insights into their formation history. Kinematic misalignments can be between gas and gas, gas and stars or stars and stars.

Misalignment between gas and stars in fast rotating early type galaxies (a class of galaxies defined by

Emsellem et al., 2007) is found in 30 to 40% of the objects (Davis et al., 2011). In slow rotating early types the distribution of the miss-alignment angle between the gas and stellar angular-momentum vectors is flat. In spiral galaxies gas and stars are usually better aligned (Pizzella et al., 2004).

A spectacular class of objects are polar ring galaxies. These galaxies are usually early types where a second stellar equilibrium component is found on a perpendicular orbit. This ring of material is often composed of young stars and large H I gas masses (Combes, 2006). Only about 0.5% of the S0 galaxies exhibit polar rings (Whitmore et al., 1990). There are two formation scenarios discussed: mergers and accretion. In the merger scenario the two galaxies have to be perpendicular oriented and at least one component has to be gas rich. However, the parameter space for creating a polar ring is quite small (Combes, 2006). The accretion scenario splits into two classes. During a galaxy passage on a hyperbolic orbit gas can be accreted due to tidal forces. This process is able to from highly inclined polar rings (see e.g. NGC 660) and probably transitions to strongly warped discs. The other mechanism is gas accretion from filaments. NGC 4650A might be an example for this because the stars are mainly in the host galaxy and the gas is mostly confined to the polar ring.

Many of the slow rotating massive early type galaxies in the ATLAS^{3D} survey have been found to have Kinematically Distinct Cores (KDC), while only a very minor fraction of the fast rotators falls into this category (Emsellem et al., 2007, 2011). There is a dichotomy between KDC: In slow rotators these are large (kpc scale structures) and made of old stellar populations that are typical for these galaxies (McDermid et al., 2006). In fast rotating galaxies the KDC are compact (less than a few hundred parsec in diameter), mostly counter rotating, and typically made of young stars. Often they are associated with central gas components. These small KDC will fade away as they age (McDermid et al., 2006).

Another class of multi-spin galaxies are the 2σ galaxies (Krajnović et al., 2011). These galaxies are characterised by the two off-centre maxima in the velocity dispersion map along the projected major axis. These galaxies are mad of two cospatial counter rotating stellar discs (Rubin et al., 1992; Rix et al., 1992; Cappellari et al., 2007). 2σ galaxies are more frequent in less massive systems ($< 5 \cdot 10^{10}\,\mathrm{M}_\odot$; Cappellari et al., 2013) and the appearance of the velocity map depends only on the intrinsic properties of the discs, their sizes and mass fractions. For a number of galaxies the two components can be separated and the stellar populations can be analysed separately. These investigations revealed that the gas is in counter rotation and the counter rotating stellar component is younger than the corotating component. No coherent picture has been found for the metallicities and α-element abundances (Coccato et al., 2011, 2013, 2015; Katkov et al., 2013, 2016; Johnston et al., 2013; Pizzella et al., 2014; Morelli et al., 2017).

1.3 Stellar populations

The light in a single CCD pixel of a galaxy image is contributed by up to 10^7 individual stars (Conroy et al., 2015). So whenever we analyse galaxies we are confronted with the fact that we see a mixture of several stars of different ages, masses and chemical compositions. The task in stellar population analysis is to decipher the information about the evolution of the galaxy from this integrated light. On the observational side we have two distinct observations: images, often taken in different bands, and spectra. On the analysis side there are many different approaches: Colour-magnitude diagram, SED, spectral index and full spectrum fitting to name a few (Burstein et al., 1984; Worthey, 1994; Cappellari & Emsellem, 2004; Cid Fernandes et al., 2005; Ocvirk et al., 2006; Koleva et al., 2009). However, all of these methods rely on stellar population modelling. Any uncertainty in the modelling will directly translate into uncertainties of the derived quantities like masses, mean ages, mean metallicities or star formation rates (Conroy et al., 2009, 2010; van Dokkum & Conroy, 2014).

Single-burst Stellar Population (SSP) models are often calibrated against Galactic and Magellanic Cloud cluster data (Worthey, 1994; Bruzual & Charlot, 2003; Maraston, 2005; Conroy et al., 2009; Vazdekis et al., 2010, 2015). Historically this is motivated by the fact that Globular Cluster (GC) have been assumed to be SSP populations. This turned out to be wrong (see review by Gratton et al., 2012), however, even today these are among the closest SSP equivalents we can find. The problem with Galactic GC is that they are all old and span only a limited range in metallicities. Other popular targets are open clusters in the Milky Way and the Magellanic Clouds (Maraston, 2005; Conroy et al., 2009). However, there are important parameter ranges that cannot be tested with these data and are therefore affected by uncertainties (van Dokkum & Conroy, 2014). For these reasons any new methods or observations that can constraint stellar population models are very important.

The above discussion clearly shows that the knowledge of stellar evolution is the backbone of the stellar population modelling. Our understanding of most evolutionary phases is quite precise. The

largest uncertainties are connected to the evolution of Asymptotic Giant Branch (AGB) and thermally pulsating Asymptotic Giant Branch (TP-AGB) stars. The AGB phase is the final stage in the evolution of low- and intermediate-mass stars. After formation and a pre-main-sequence evolution these stars burn hydrogen in their cores during the main-sequence evolution. When the H in the core is exhausted the core starts to contract due to the gravitational pull. At the same time the envelope expands, leading to a brightening of the stars. This is the turn-off from the main-sequence and the evolution on the sub-giant branch. Once the temperature is high enough the H burning starts in a shell around the He core. Now the star is ascending the Red Giant Branch (RGB). In this phase the envelope is fully convective and the so called first dredge-up brings processed material to the surface. The hydrogen burning shell deposits additional He to the core, increasing its mass and temperature. When the critical temperature is reached, He core burning starts. For stars with initial masses above $1.8\,M_\odot$ this is a gentle ignition, less massive stars have an electron degenerate He core and ignition leads to a flash. The star then settles on the horizontal branch. When the He-core is exhausted the star has a degenerate oxygen carbon core. Stars less massive than $8\,M_\odot$ cannot ignite carbon burning. These stars ignite He shell burning, while the H shell is still burning. During this early AGB phase the He shell is the dominant source of nuclear fusion. The early AGB phase ends when the He burning shell reaches the H burning shel. In the following TP-AGB evolution the He shell burning occures in thermo-nuclear flashes, with quiescent interpulse phases where the H burning shell deposits a new He shell. The He-flashes cause an extremely deep mixing event that brings processed material from the interior of the star to the surface (so called third dredge-up) and changes the element abundances in the atmosphere. The repeated dredge-up events increase the C/O abundance in the atmosphere from a value below one (AGB stars of spectral type M) to even values (S-type) and values larger than unity (C-type).

The AGB phase is quiet short, it lasts about 1/1000 of the main-sequence life-time. During this time the star experiences a number of thermal pulses. This means that modelling this evolutionary phase requires very good time resolution. At the same time the evolution is sensitive to the initial mass, chemical composition and mas-loss during the RGB phase. This makes the modelling very challenging. Many processes cannot be derived from first principles, but need to be parametrized (e.g. mass-loss). AGB stars are rare and therefore the observational constraints limited. Especially the fact that most AGB stars are observed in the local group (Milky Way, Magellanic Clouds and Andromeda and their dwarf galaxy population) also biases the comparison. For stellar population modelling the uncertainties are even more severe, because some considerable disagreement exists between the contribution of AGB stars to the integrated light. While Maraston (2005) predict that TP-AGB stars contribute up to 80% to the integrated infrared light for young populations (0.3 to 2 Gyr), Bruzual & Charlot (2003) predict much weaker contributions. These differences have significant consequences for the interpretation of galaxy observations: mass-to-light ratios, masses and ages are affected (Maraston et al., 2006; Conroy, 2013). Especially the fact that models seem to work systematically in the optical but not in the infrared and vice versa calls for additional observational constraints (Eminian et al., 2008; Zibetti et al., 2009; Taylor et al., 2011).

1.4 Outline

This thesis is based on data from the science verification of the *Very Large Telescope* (*VLT*) second generation instrument 'Multi-Unit Spectroscopic Explorer' (MUSE). I applied for these Integral Field Spectroscopy (IFS) data to measure the first surface brightness fluctuation spectrum. MUSE is the first and only IFS that provides a sufficiently large field of view with a sufficient spatial sampling to apply the Surface Brightness Fluctuation (SBF) method to its data. For this pilot study I decided to observe NGC 5102, the galaxy with the brightest SBF magnitude in the I-band SBF survey (Tonry et al., 1997, 2001) in the southern sky.

IFS data are very versatile and can be used for many different science cases. I used the NGC 5102 data to investigate the dynamics of this galaxy and learn about the population and DM halo properties. The dynamics of this galaxy have to my knowledge never been investigated, neither with long-slit nor with IFS data. With these high quality data of a low-mass S0 galaxy I am able to probe the low mass end of the larger surveys ATLAS^{3D} (Cappellari et al., 2011) and CALIFA (Sánchez et al., 2012), that necessarily have poorer data quality on individual galaxies.

The outline of this work is as follows. I start with the investigation of the dynamics of NGC 5102 in Chapter 2. In this chapter we discover that NGC 5102 is a 2σ galaxy. I model the stellar kinematics using axis symmetric Jeans anisotropic models (JAM; Cappellari, 2008). The models reveal that this galaxy cannot be described by the stellar mass distribution alone. The disagreement between the

stellar mass only models and the observed kinematics is the so far strongest evidence for the need of dark matter to explain the kinematics of a single galaxy with JAM models. Including a Navarro, Frenk & White (1996) dark matter halo solves the disagreement between the modelled and observed kinematics and leads to a heavy IMF and a DM fraction of 0.37 inside a sphere of one R_e. A very robust result is the logarithmic slope of the total matter density slope. I measure a value of -1.75 ± 0.04 that is shallower than an isothermal halo and agrees qualitatively with a tentative correlation in the literature of decreasing total mass density slope with decreasing mass.

Chapter 3 introduces the classical SBF method and gives a motivation for the benefits from SBF spectra. In this chapter a thorough introduction to SBF is given and in depth explained how SBF are measured from CCD observations. The literature on classical SBF is reviewed. The chapter is concluded with a discussion on the influence of stellar populations on SBF and the diagnostic potential of SBF for investigating bright (typically evolved) stars.

Chapter 4 introduces the stellar population synthesis code 'Stellar Populations for All Applications' (SPAA). This technical chapter explains the input data, initial mass function, isochrones and stellar spectral libraries, that are used to compute the population spectra. I go on with describing the synthesis algorithm is detail, especially the use of the mass-density diagram (so called Hess-diagram) and the spectrum interpolation routine. The unique feature of SPAA is the prediction of SBF spectra. I discuss the computation of those, why complex stellar population SBF spectra are not a linear combination of SSP SBF spectra and how this problem is solved in SPAA.

The first SBF spectrum of a galaxy is presented in Chapter 5. I explain how the SBF spectrum is measured from the MUSE data. Stellar population models predict that the SBF spectrum is dominated by giant stars. I verify this by comparing the SBF spectrum with stellar spectra. The contribution from M and C type giant stars is evaluated. To be able to compare the SBF spectrum with proper stellar population models I present the SPAA model spectra and validate the new models by comparing with existing stellar population models. The comparison of the stellar population models with the integrated and the SBF spectrum reveals that the models can reproduce the observed spectrum. I use the SBF data spectrum to investigate inconsistencies between different sets SBF model spectra.

Bibliography

Adams J. J., et al., 2014, ApJ, 789, 63
Alpher R. A., Herman R., 1948, Nature, 162, 774
Alpher R. A., Bethe H., Gamow G., 1948, Phys. Rev., 73, 803
Babcock H. W., 1938, PhD thesis, UNIVERSITY OF CALIFORNIA, BERKELEY.
Boylan-Kolchin M., Bullock J. S., Kaplinghat M., 2011, MNRAS, 415, L40
Bruzual G., Charlot S., 2003, MNRAS, 344, 1000
Bullock J. S., Kolatt T. S., Sigad Y., Somerville R. S., Kravtsov A. V., Klypin A. A., Primack J. R., Dekel A., 2001, MNRAS, 321, 559
Burstein D., Faber S. M., Gaskell C. M., Krumm N., 1984, ApJ, 287, 586
Cappellari M., 2008, MNRAS, 390, 71
Cappellari M., Emsellem E., 2004, PASP, 116, 138
Cappellari M., et al., 2007, MNRAS, 379, 418
Cappellari M., et al., 2011, MNRAS, 413, 813
Cappellari M., et al., 2013, MNRAS, 432, 1709
Cardone V. F., Sereno M., 2005, A&A, 438, 545
Cid Fernandes R., Mateus A., Sodré L., Stasińska G., Gomes J. M., 2005, MNRAS, 358, 363
Coccato L., Morelli L., Corsini E. M., Buson L., Pizzella A., Vergani D., Bertola F., 2011, MNRAS, 412, L113
Coccato L., Morelli L., Pizzella A., Corsini E. M., Buson L. M., Dalla Bontà E., 2013, A&A, 549, A3
Coccato L., et al., 2015, A&A, 581, A65
Combes F., 2006, in Mamon G. A., Combes F., Deffayet C., Fort B., eds, EAS Publications Series Vol. 20, EAS Publications Series. pp 97–104 (arXiv:astro-ph/0508434), doi:10.1051/eas:2006054
Conroy C., 2013, ARA&A, 51, 393
Conroy C., Gunn J. E., White M., 2009, ApJ, 699, 486
Conroy C., White M., Gunn J. E., 2010, ApJ, 708, 58
Conroy C., van Dokkum P. G., Choi J., 2015, Nature, 527, 488
Davis T. A., et al., 2011, MNRAS, 417, 882
Di Cintio A., Brook C. B., Macciò A. V., Stinson G. S., Knebe A., Dutton A. A., Wadsley J., 2014, MNRAS, 437, 415
Dicke R. H., Peebles P. J. E., Roll P. G., Wilkinson D. T., 1965, ApJ, 142, 414
Doroshkevich A., Tucker D. L., Allam S., Way M. J., 2004, A&A, 418, 7
Duffy A. R., Schaye J., Kay S. T., Dalla Vecchia C., Battye R. A., Booth C. M., 2010, MNRAS, 405, 2161
Eminian C., Kauffmann G., Charlot S., Wild V., Bruzual G., Rettura A., Loveday J., 2008,

MNRAS, 384, 930
Emsellem E., et al., 2007, MNRAS, 379, 401
Emsellem E., et al., 2011, MNRAS, 414, 888
Flores R. A., Primack J. R., 1994, ApJ, 427, L1
Gnedin O. Y., Kravtsov A. V., Klypin A. A., Nagai D., 2004, ApJ, 616, 16
Gratton R. G., Carretta E., Bragaglia A., 2012, A&ARv, 20, 50
Guth A. H., 1981, Phys. Rev. D, 23, 347
Hoyle F., Tayler R. J., 1964, Nature, 203, 1108
Hubble E. P., 1925, Popular Astronomy, 33
Hubble E., 1929, Proceedings of the National Academy of Science, 15, 168
Johnston E. J., Merrifield M. R., Aragón-Salamanca A., Cappellari M., 2013, MNRAS, 428, 1296
Katkov I. Y., Sil'chenko O. K., Afanasiev V. L., 2013, ApJ, 769, 105
Katkov I. Y., Sil'chenko O. K., Chilingarian I. V., Uklein R. I., Egorov O. V., 2016, MNRAS, 461, 2068
Klypin A., Kravtsov A. V., Valenzuela O., Prada F., 1999, ApJ, 522, 82
Koleva M., Prugniel P., Bouchard A., Wu Y., 2009, A&A, 501, 1269
Krajnović D., et al., 2011, MNRAS, 414, 2923
Kuzio de Naray R., McGaugh S. S., de Blok W. J. G., Bosma A., 2006, ApJS, 165, 461
Kuzio de Naray R., McGaugh S. S., de Blok W. J. G., 2008, ApJ, 676, 920
Maraston C., 2005, MNRAS, 362, 799
Maraston C., Daddi E., Renzini A., Cimatti A., Dickinson M., Papovich C., Pasquali A., Pirzkal N., 2006, ApJ, 652, 85
McDermid R. M., et al., 2006, MNRAS, 373, 906
Moore B., 1994, Nature, 370, 629
Moore B., Quinn T., Governato F., Stadel J., Lake G., 1999a, MNRAS, 310, 1147
Moore B., Ghigna S., Governato F., Lake G., Quinn T., Stadel J., Tozzi P., 1999b, ApJ, 524, L19
Morelli L., et al., 2017, A&A, 600, A76
Navarro J. F., Frenk C. S., White S. D. M., 1996, ApJ, 462, 563
Ocvirk P., Pichon C., Lançon A., Thiébaut E., 2006, MNRAS, 365, 74
Oh S.-H., de Blok W. J. G., Walter F., Brinks E., Kennicutt Jr. R. C., 2008, AJ, 136, 2761
Oh S.-H., et al., 2015, AJ, 149, 180
Papastergis E., Giovanelli R., Haynes M. P., Shankar F., 2015, A&A, 574, A113
Penzias A. A., Wilson R. W., 1965, ApJ, 142, 419
Percival W. J., et al., 2001, MNRAS, 327, 1297
Perlmutter S., et al., 1999, ApJ, 517, 565
Pizzella A., Corsini E. M., Vega Beltrán J. C., Bertola F., 2004, A&A, 424, 447
Pizzella A., Morelli L., Corsini E. M., Dalla Bontà E., Coccato L., Sanjana G., 2014, A&A, 570, A79
Planck Collaboration et al., 2016, A&A, 594, A12
Riess A. G., et al., 1998, AJ, 116, 1009
Rix H.-W., Franx M., Fisher D., Illingworth G., 1992, ApJ, 400, L5
Rubin V. C., 1994, AJ, 108, 456
Rubin V. C., Ford Jr. W. K., 1970, ApJ, 159, 379
Rubin V. C., Graham J. A., Kenney J. D. P., 1992, ApJ, 394, L9
Sánchez S. F., et al., 2012, A&A, 538, A8
Smith S., 1936, ApJ, 83, 23
Smoot G. F., et al., 1992, ApJ, 396, L1
Spekkens K., Giovanelli R., Haynes M. P., 2005, AJ, 129, 2119
Taylor J. E., Navarro J. F., 2001, ApJ, 563, 483
Taylor E. N., et al., 2011, MNRAS, 418, 1587
Tonry J. L., Blakeslee J. P., Ajhar E. A., Dressler A., 1997, ApJ, 475, 399
Tonry J. L., Dressler A., Blakeslee J. P., Ajhar E. A., Fletcher A. B., Luppino G. A., Metzger M. R., Moore C. B., 2001, ApJ, 546, 681
Vazdekis A., Sánchez-Blázquez P., Falcón-Barroso J., Cenarro A. J., Beasley M. A., Cardiel N., Gorgas J., Peletier R. F., 2010, MNRAS, 404, 1639
Vazdekis A., et al., 2015, MNRAS, 449, 1177
Weldrake D. T. F., de Blok W. J. G., Walter F., 2003, MNRAS, 340, 12
Whitmore B. C., Lucas R. A., McElroy D. B., Steiman-Cameron T. Y., Sackett P. D., Olling R. P., 1990, AJ, 100, 1489
Worthey G., 1994, ApJS, 95, 107
Zibetti S., Charlot S., Rix H.-W., 2009, MNRAS, 400, 1181
Zwicky F., 1933, Helvetica Physica Acta, 6, 110
de Blok W. J. G., Bosma A., 2002, A&A, 385, 816
de Blok W. J. C., McGough S. S., 1997, in Persic M., Salucci P., eds, Astronomical Society of the Pacific Conference Series Vol. 117, Dark and Visible Matter in Galaxies and Cosmological Implications. p. 39 (arXiv:astro-ph/9610216)
de Blok W. J. G., McGaugh S. S., Rubin V. C., 2001a, AJ, 122, 2396
de Blok W. J. G., McGaugh S. S., Bosma A., Rubin V. C., 2001b, ApJ, 552, L23
van Dokkum P. G., Conroy C., 2014, ApJ, 797, 56

Dominant dark matter and a counter rotating disc: MUSE view of the low luminosity S0 galaxy NGC 5102*

2

The kinematics and stellar populations of the low-mass nearby S0 galaxy NGC 5102 are studied from integral field spectra taken with the Multi-Unit Spectroscopic Explorer. The kinematic maps reveal for the first time that NGC 5102 has the characteristic 2σ peaks indicative of galaxies with counter-rotating discs. This interpretation is quantitatively confirmed by fitting two kinematic components to the observed spectra. Through stellar population analysis, we confirm the known young stellar population in the centre and find steep age and metallicity gradients. We construct axisymmetric Jeans anisotropic models of the stellar dynamics to investigate the Initial Mass Function (IMF) and the dark matter halo of the galaxy. The models show that this galaxy is quite different from all galaxies previously studied with a similar approach: even within the half-light radius, it cannot be approximated with the self-consistent mass-follows-light assumption. Including a Navarro, Frenk & White dark matter halo, we need a heavy IMF and a dark matter fraction of 0.37 ± 0.04 within a sphere of one R_e radius to describe the stellar kinematics. The more general model with a free slope of the dark matter halo shows that slope and IMF are degenerate, but indicates that a light weight IMF (Chabrier-like) and a higher dark matter fraction, with a steeper (contracted) halo, fit the data better. Regardless of the assumptions about the halo profile, we measure the slope of the total mass density to be -1.75 ± 0.04. This is shallower than the slope of -2 of an isothermal halo and shallower than published slopes for more massive early-type galaxies.

2.1 Introduction

NGC 5102 is a low-luminosity S0 galaxy in the Centaurus group (Karachentsev et al., 2002) at a distance of 4.0 ± 0.2 Mpc, as determined via the surface brightness fluctuation method by Tonry et al. (2001). There is some uncertainty about the distance to NGC 5102: values based on the planetary nebula luminosity function tend to find shorter distances of 3.1 Mpc (McMillan et al., 1994). The distances obtained from tip of the red-giant branch measurements scatter: Karachentsev et al. (2002) find a distance of 3.4 Mpc, Davidge (2008) measures 3.2 Mpc and Tully et al. (2015) find 3.74 Mpc. The choice of the distance (throughout this paper we will use $D = 4.0 \pm 0.2$ Mpc by Tonry et al., 2001) does not influence our conclusions but sets the scale of our models in physical units. Specifically, lengths and masses scale as D, while M/L_* scales as D^{-1}.

The photometry of NGC 5102 shows the typical features of an S0 galaxy: a bulge that follows a $r^{1/4}$ profile and a disc with a flatter profile at larger radii (Pritchet, 1979; Davidge, 2015). The central deviation from the $r^{1/4}$ profile builds the nucleus. Other observations show that NGC 5102 is an unusual S0 galaxy: the nucleus has an unusually blue colour (first mentioned by Freeman in Eggen, 1971) for S0 galaxies and is interpreted as a star cluster with an age of $\sim 10^8$ yr (e.g. Gallagher et al., 1975; van den Bergh, 1976; Pritchet, 1979).

The second peculiarity about NGC 5102 is the relatively large H I content of $3.3 \times 10^8\,M_\odot$ (Gallagher et al., 1975). van Woerden et al. (1993) map the spatial and spectral properties of the H I and find a ring-like structure with a prominent central depression with a radius of 2.2 kpc. The rotation curve is aligned with the

* This chapter is published in Martin Mitzkus, Michele Cappellari and C. Jakob Walcher, *Monthly Notices of the Royal Astronomical Society*, 2017, Volume 464, pages 4789-4806.

stellar disc and flattens at lager radii at $95\,\mathrm{km\,s^{-1}}$ (van Woerden et al., 1993; Kamphuis et al., 2015). The H I profile with at 50% intensity is $W_{50} = 200\,\mathrm{km\,s^{-1}}$ (van Woerden et al., 1993; Kamphuis et al., 2015), given that the flat rotation curve regime is reached this gives a measure of the maximum radial rotational velocity $V_\mathrm{m} = W_{50}/2$.

The last notable unusual finding is the significant gas emission structure, first detected in Hα by van den Bergh (1976). Later McMillan et al. (1994) imaged the gas emission in Hα and [O III] finding a ring-like structure as well. Based on the line ratios, McMillan et al. (1994) conclude that the gas is ionized by a shock, moving with $\sim 60\,\mathrm{km\,s^{-1}}$. This structure has a diameter of 1.3 kpc and an estimated age of $\sim 10^7$ yr. Based on this age estimate, the authors conclude that this supershell is not associated with the blue nuclear star cluster. From the mass and the energy of the shell, McMillan et al. (1994) conclude that a few hundred supernovae are enough to form this supershell.

Observing NGC 5102 in X-ray, Kraft et al. (2005) find that the number of X-ray point sources is smaller than expected from galaxies of similar morphological type. The significance of these results is unclear due to contamination with background Active Galactic Nuclei (AGN) and low number statistics. One of the X-ray point sources coincides with the optical centre of NGC 5102, hinting at weak AGN activity. This is in contrast to the findings of other authors that do not see AGN activity in NGC 5102 (e.g. Bendo & Joseph, 2004). The diffuse X-ray component is centrally peaked and centred on the optical galaxy centre. The authors suggest that this is the supershell detected by McMillan et al. (1994) and their mass and energy estimates roughly agree with the values of McMillan et al. (1994).

The star formation history of NGC 5102 has been investigated many times. Using *Hubble Space Telescopes* (*HST's*) 'Faint Object Camera', Deharveng et al. (1997) detected a population of resolved blue stars in the centre of NGC 5102. The authors interpret these as young stars from a star formation burst that occurred 1.5×10^7 yr ago, but they cannot exclude that these stars are much older post-Asymptotic Giant Branch (AGB) stars. In line with this, Beaulieu et al. (2010) find a stable Star Formation Rate (SFR) over the last 0.2 Gyr with a recent (20 Myr) star formation burst in the centre. A star formation burst a few 10^7 yr ago is in remarkable agreement with the estimated time-scale of the superbubble detected by McMillan et al. (1994). Using long slit-spectra, with the slit oriented along the minor axis of the galaxy, Davidge (2015) determines a luminosity weighted Single-burst Stellar Population (SSP) age for the nucleus and bulge of $1^{+0.2}_{-0.1}$ and $2^{+0.5}_{-0.2}$ Gyr, respectively. From Lick index measurements, Davidge (2015) find a (spatially) roughly constant metallicity of $Z = 0.004$ for NGC 5102.

For the disc, Beaulieu et al. (2010) find a declining SFR over the last 0.2 Gyr and a recently quiescent SFR. Davidge (2008) determines the SFR of the disc in the last 10 Myr to be $0.02\,\mathrm{M_\odot\,yr^{-1}}$. However, during intermediate epochs the SFR was higher and 20% of the disc mass formed within the last 1 Gyr.

Davidge (2010) finds hints for a merger in NGC 5102: at a projected distance of 18 kpc from the galaxy centre along the minor axis, he finds a concentration of AGB stars and suggests this might be the remnant of a companion galaxy. On the one hand, this interpretation is supported by the warped H I in the outer disc (van Woerden et al., 1993). Davidge (2010) points out that this warp is also traced by the OAGB stars. On the other hand the author mentions that this interpretation is challenged by the current isolation of NGC 5102. Karachentsev et al. (2007) determine the nearest neighbour being ESO383-G087 at a projected distance of 0.3–0.4 Mpc. Davidge (2015) determines an SSP age of 10 ± 2 Gyr for the disc and finds the stellar population to be metal-poor at $Z = 0.004$, like the one in the nucleus and bulge.

The mass of NGC 5102 was estimated by different authors: van Woerden et al. (1993) find the total mass inside a radius of 6.1 kpc from the H I rotation curve to be $1.2 \times 10^{10}\,\mathrm{M_\odot}$. Davidge (2008) subtracts a mean dark matter (DM) density and derives a stellar mass of $7.0 \times 10^9\,\mathrm{M_\odot}$ within the same region. Beaulieu et al. (2010) estimate the stellar mass by combining the photometry of NGC 5102 with the M_*/L_B models by Bell & de Jong (2001) and find it to be $(5.6 \pm 0.8) \times 10^9\,\mathrm{M_\odot}$.

In this paper, we analyse new high-quality integral-field observations of the NGC 5102 to study the stellar population and kinematics of this low-mass galaxy in more detail. We construct dynamical models to study the DM content.

2.2 Observations and data reduction

NGC 5102 was observed with the new second generation Very Large Telescope (VLT) instrument Multi-Unit Spectroscopic Explorer (MUSE; Bacon et al., 2010) during the science verification run [programme 60.A-9308(A), PI: Mitzkus] in the night from 2014 June 23 to 24. The data were taken in the wide field mode with a 1 arcmin × 1 arcmin field of view

and a plate scale of 0.2 arcsec. The normal mode covers the spectral range from 4750 to 9340 Å with a fixed sampling of 1.25 Å, the spectral Full Width at Half Maximum (FWHM) is 2.5 Å over the whole wavelength range.

The data set consists of four dithered exposures, each rotated by 90° with 960 s exposure time, centred on NGC 5102. In total we have a time on target of 3840 s. The complicated image slicer system of MUSE leaves residual structures in the data. We applied the dither and rotation pattern to smoothly distribute these residuals. The observations were split into two observing blocks, scheduling between the two object exposures of each block a 300 s offset sky exposure. The calibration frames were taken according to the standard European Southern Observatory (ESO) calibration plan for MUSE.

The MUSE NGC 5102 data were reduced using the dedicated MUSE data reduction system (DRS; Weilbacher et al., 2012) version 1.0.1 through the ESOREX[1] program. For most of the reduction steps, we followed the standard procedure as outlined in the MUSE data reduction cookbook shipped with the DRS. The sky subtraction for this data set is complicated because NGC 5102 extends over the full field of view, thus the sky cannot be estimated from the object exposure. The sky continuum and the sky lines were measured from the aforementioned sky exposures and then subtracted from the object exposures that were taken directly before and after the sky exposure.

The response curve is usually measured from the spectrophotometric standard star observed during the night the data were obtained. This would be the spectrophotometric standard star CD-32, but the reference calibration spectrum of this star is labelled as 'bad resolution, should not be used' in the MUSE data reduction cookbook. Therefore, we used the standard star GD153, observed in the following night. All other steps to measure and apply the response curve follow the standard procedure described in the MUSE data reduction cookbook.

2.3 NGC 5102 kinematics

2.3.1 Voronoi binning

To make sure that all spectra have sufficient signal-to-noise ratio (S/N) for an unbiased kinematic extraction, especially at large radii, we used the Voronoi binning method[2] (Cappellari & Copin, 2003) to co-add spatially adjacent spectra. We use a white-light image in the wavelength range from 4800 to 6000 Å as signal input and the square root of the mean pipeline propagated variances in the same wavelength range as noise input to the Voronoi binning routine. Because the pipeline uncertainties are not always reliable, due to the difficulty of propagating covariances, we verified the S/N after the binning. We derived the S/N as the ratio between the mean signal and the rms of the residual from a penalized pixel fitting code (PPXF) fit (see Section 2.3.2). For the spectral range from 4760 to 7400 Å, the median is S/N = 113 per spectral pixel of 50.6 km/s (see Table 2.1 for details). Finally all spectra falling on to the same Voronoi bin are added up, resulting in nearly 1300 Voronoi-binned spectra.

2.3.2 One component kinematic fit

We determine the line-of-sight velocity distribution (LOSVD) by using the PPXF[2] (Cappellari & Emsellem, 2004). In PPXF the LOSVD is parametrized as a Gauss–Hermite function, allowing us to measure departures from a pure Gaussian LOSVD. The input spectrum is fitted with a linear combination of spectra from a template library and additive or multiplicative polynomials might be used to correct for continuum mismatch. As template library, we use the ∼ 1000 stellar spectra of the MILES library (Sánchez-Blázquez et al., 2006; Falcón-Barroso et al., 2011) for fits in the 4760–7400 Å wavelength range, where the blue cut is set by the spectral coverage of MUSE and the red cut by the MILES library. For the wavelength region 8440–8810 Å around the Ca II triplet (referred to as Ca II triplet region in the following), the ∼ 700 stars from the CaT library (Cenarro et al., 2001) are used. The MUSE spectral FWHM is 2.5 Å, which matches the instrumental resolution of the MILES stars (Beifiori et al., 2011; Falcón-Barroso et al., 2011). Therefore, this library is not convolved with an instrumental FWHM. Since the spectral resolution of the CaT library is higher (1.5 Å), we degrade the resolution of these stars to match the MUSE spectral resolution of 2.5 Å.

We logarithmically rebin the galaxy (for the MILES range we use a velocity step of 50.6 km s^{-1}, for the Ca II region the velocity step is 42.5 km s^{-1}) and the template spectra before the fit and mask regions of gas emission (including Hα and Hβ) and telluric emission lines. We use additive polynomials to account for the response function and template mismatch, as well as to account for spatial variation in the stellar line strength. For the 4760–7400 Å region, we use a seventh-order polynomial, the much shorter Ca II triplet region is fitted with a first-order polynomial. For the fitting, we use a two-step approach:

[1] ESOREX stands for ESO Recipe Execution Tool, a command line based tool to execute data reduction software for ESO-VLT data.

[2] Available from http://purl.org/cappellari/software.

Table 2.1: Parameters from the kinematic fits.

	$V_{\rm sys}^{a}$ (km s^{-1})	$V_{\rm ampl}^{b}$ (km s^{-1})	$\Delta V_{\rm sampling}^{c}$ (km s^{-1})	PA^{d} (°)	$\Delta\sigma^{e}$ (km s^{-1})	δ_{σ}^{f} –	S/N^{g} –
MILES two moment	473.3	17.5	50.6	45.5	–	–	113
MILES four moment	474.5	20.6	50.6	47.0	1.2	1.04	113
Ca II triplet two moment	472.7	16.9	42.5	44.5	7.3	1.05	109
Ca II triplet four moment	472.5	21.4	42.5	44.5	6.8	1.04	110

[a] $V_{\rm sys}$ is the systemic velocity of NGC 5102, determined with the FIT_KINEMATIC_PA routine, a PYTHON implementation of the method Krajnović et al. (2006) describe in Appendix C to measure the global kinematic position angle.
[b] $V_{\rm ampl}$ is the amplitude of the rotation velocity, determined as 1/2 of the sum of absolute values of the minimum and maximum values of the symmetrized velocity field (using the PYTHON routine CAP_SYMMETRIZE_VELFIELD).
[c] The logarithmically rebinned spectra have a constant sampling step in the velocity space. $\Delta V_{\rm sampling}$ is this sampling size.
[d] PA is the kinematic position angle, also determined with the aforementioned FIT_KINEMATIC_PA routine.
[e] $\Delta\sigma$ is the mean of the difference MILES two moment extraction dispersion and the dispersion from the kinematic extraction under consideration.
[f] δ_{σ} is the factor the velocity dispersion field under consideration needs to be scaled to minimize the absolute difference to the MILES two moment dispersion.
[g] S/N is as the ratio between the mean signal and the rms of the residual from a PPXF fit.

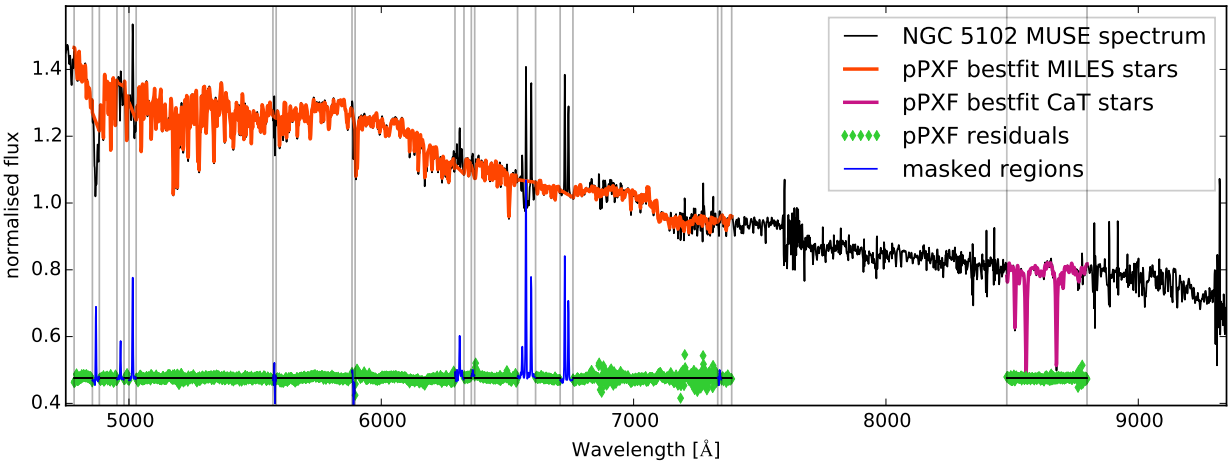

Figure 2.1: The collapsed NGC 5102 MUSE spectrum is shown in black. The best-fitting PPXF model, a linear combination of the MILES (red) or CaT (magenta) stars is shown in the respective wavelength ranges. The residuals between observed and model spectrum are shown in green, in masked regions these are blue. The grey vertical lines mark the masked intervals.

the collapsed spectrum (adding all MUSE spectra together) is fitted with all stars in the corresponding library. From this fit a template is computed by computing the weighted sum of the stellar spectra, using the weights PPXF determined. The collapsed NGC 5102 spectrum and the two template spectra are shown in Fig. 2.1 This spectrum is then used to fit the LOSVD of each Voronoi bin. Given the significant population gradient we observe in NGC 5102 (see Section 2.4), we checked that the kinematics are not biased by the fixed template and computed the kinematics also from a fit where the full set of MILES stars is used as input template to PPXF. These extractions are qualitatively similar to the kinematics obtained with a fixed best-fitting template, but are noisier and less symmetric. Therefore, we base the further discussion on the kinematics obtained with the fixed best-fitting template.

We fit a two moment (V and σ) and a four moment (V, σ and the Gauss–Hermite h_3 and h_4 parameters) LOSVD to the data. The uncertainties on the spectrum are assumed to be constant with wavelength. The reason for this is that the pipeline propagated errors contain noise themselves and this extra noise can potentially increase the uncertainties in the kinematics. The assumption of constant errors can be cross checked against the residuals (difference between input and best-fitting spectrum) of the fit: Fig. 2.1 shows that these residuals are constant with wavelength, thus justifying the assumption of constant errors.

The resulting two-dimensional maps of the LOSVD in the four moment extraction are shown in Fig. 2.2. The velocity field is plotted relative to the systemic velocity of $V_{\rm sys} = 474.5\,{\rm km\,s^{-1}}$. We compute the systemic velocity with the FIT_KINEMATIC_PA routine[2], a PYTHON implementation of the method Krajnović et al. (2006) describe in Appendix C to measure the global kinematic position angle. The structure of the velocity field (Fig. 2.2) is complicated: a clear rotation pattern is visible in the centre and there is an indication that the rotation reverses at larger radii. Looking at the velocity dispersion map, we see a central peak and a rise of the dispersion towards the outer parts of the field of view along major axis. This peculiar rise of the stellar velocity dispersion at large radii along the galaxy projected major axis was first observed and interpreted by Rix et al. (1992) in the S0 galaxy NGC 4550 with counter-rotating discs discovered by Rubin et al. (1992). Detailed dynamical models of this galaxy, as well as of the similar one NGC 4473, based on integral-field kinematics, were presented in Cappellari et al. (2007). They confirmed the original interpretation of this class of galaxies, having 2σ peaks along the projected major axis, as due to counter-rotating discs of comparable light contribution. The ATLAS^{3D} survey (Cappellari et al., 2011) observed a volume-limited sample of 260 early-type galaxies (ETGs) with stellar mass $M_* \gtrsim 1 \times 10^{10}\,{\rm M}_\odot$ and found that 11 of them (4%) belong to this class of counter-rotating disc galaxies, which they aptly named 2σ galaxies (Krajnović et al., 2011). Dynamical models of six of them, for a range of counter-rotating mass fraction, are shown in fig. 12 of Cappellari (2016). NGC 4473 is an example where the 2σ peaks were predicted using dynamical models (Cappellari et al., 2007), but only later actually observed with more spatially extended observations (Foster et al., 2013, fig. 1). To our knowledge, this is the first time this rotation pattern is observed in NGC 5102. The previous dynamical modelling result strongly suggests this galaxy also contains two counter-rotating discs, and this interpretation is actually confirmed in Section 2.6.4.

The fit of the Ca II region is in broad agreement with the results obtained from the 4760–7400 Å wavelength range and the MILES library. In Table 2.1, we compare key parameters of the four velocity extractions: the systemic velocity $V_{\rm sys}$, the amplitude of the inner rotation pattern $V_{\rm ampl}$, the position angle (PA), the additive offset of the dispersion maps $\Delta\sigma$ and the scaling factor δ_σ that minimizes the residuals between two dispersion maps (we compare to the blue two moment kinematics). The amplitude of the rotation is larger in the four moment kinematic extractions, indicating that the LOSVD is non-Gaussian. This is to be expected when two counter-rotating components are present in the system. The velocity dispersion in this galaxy is expected to vary appreciably as a function of wavelength. This is because the width of the absorption lines will depend on the relative contribution the two counter-rotating components add to each wavelength range. This gets amplified by the quite different populations (see Section 2.4).

2.3.3 Fitting for two components

As mentioned in the previous section, the stellar kinematics indicate two counter-rotating populations in NGC 5102. The median *observed* velocity difference of the two stellar components (derived from the results presented in Fig. 2.4) is $\sim 75\,{\rm km\,s^{-1}}$. This suggests that the LOSVD of the two stellar components will not be resolvable by the MUSE spectral resolution of $\sigma_{\rm instr} \approx 65\,{\rm km\,s^{-1}}$ around the strong Hβ feature. This makes the actual extraction of two kinematic components particularly challenging from these data, even though the presence of two components is quite clear from the σ maps. However,

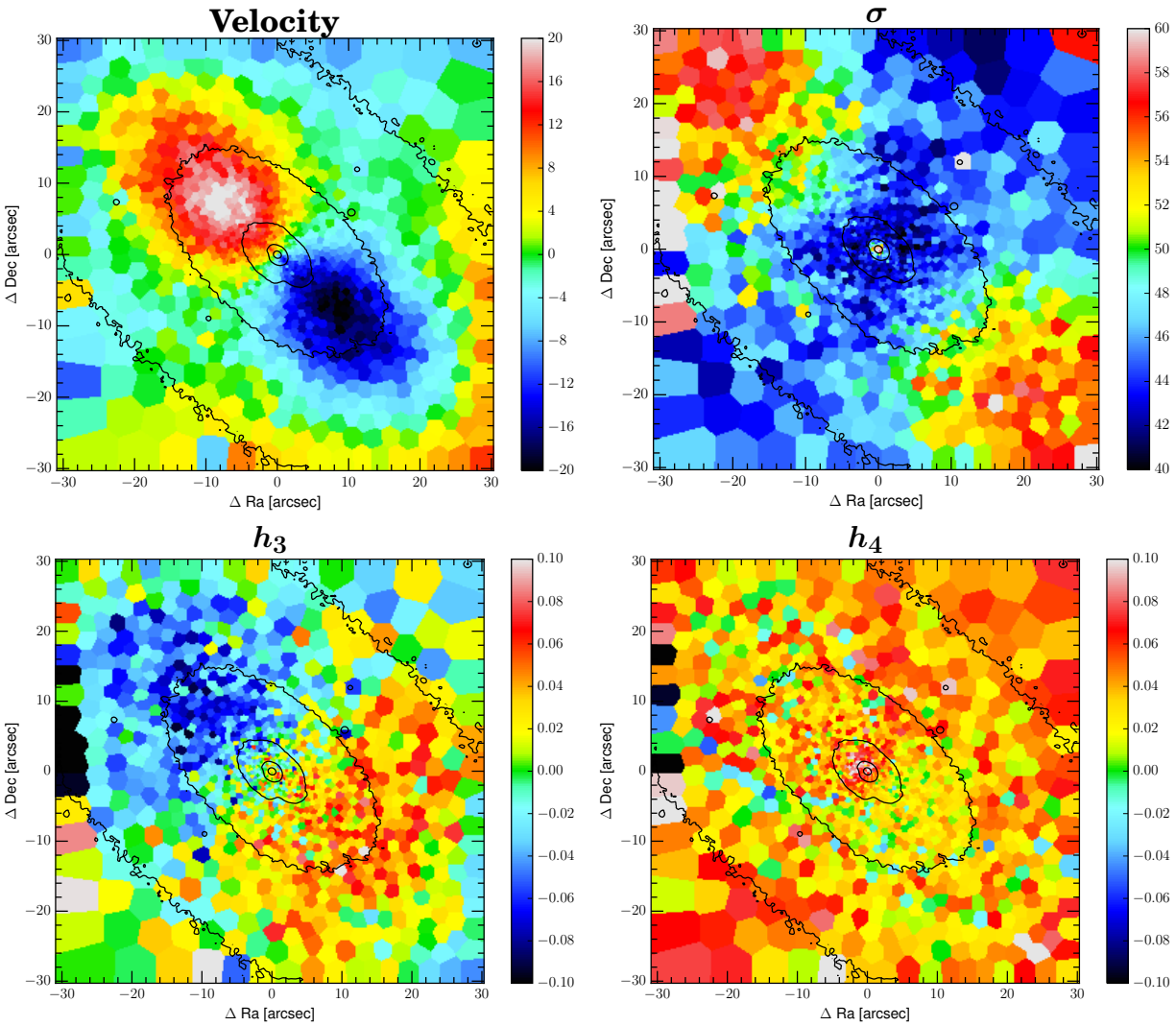

Figure 2.2: From top left to bottom right: velocity, velocity dispersion σ, h_3 and h_4 fields of the four moment kinematic fit to the 4760–7400 Å wavelength region. The median value of -0.019 has been subtracted from the h_3 map. The asymmetry of the h_3 field is indicative for residual template mismatch. To exclude that this is caused by the single template spectrum used to extract this kinematics, we checked the h_3 map of the full MILES spectrum fit for structure in the h_3 map. This map has an even stronger structure and is less symmetric. Black lines are the isophotes of the galaxy's integrated light.

in the red part of the spectrum the chances of separating the two components are actually quite good, given the $\sigma_{\rm instr} \approx 37\,{\rm km\,s^{-1}}$. We therefore use the Ca II triplet and the MIUSCAT library to separate the two components. PPXF has the option to fit an arbitrary number of different kinematic components (e.g. Coccato et al., 2011; Johnston et al., 2013), so we use for each kinematic component an identical set of templates. Our template consists of those eight MIUSCAT spectra that contribute most to the integrated NGC 5102 spectrum.

Finding the suspected two kinematic solutions using PPXF requires precise starting values, because PPXF uses a local minimization algorithm. When two kinematic components are present, the single-component solution is necessarily, by symmetry, a saddle point in the $\Delta\chi^2$ landscape. Moreover one should expect a cross-like degeneracy centred on the single-component fit. Due to these degeneracies imprecise starting velocities can lead PPXF to converge prematurely to the single-component solution. To make sure we do not miss the global minimum of the two-component fit, we need to employ a global rather than local optimization approach. The approach we adopt is straightforward but brute force. For each Voronoi bin spectrum, we scan a region of starting velocities for both components: all combinations of starting velocities in the range from $V_{\rm sys} - 100$ to $V_{\rm sys} + 140\,{\rm km\,s^{-1}}$ are tested in steps of $V_{\rm step} = 15\,{\rm km\,s^{-1}}$ for both components. This results in 289 different starting velocity combinations that we fit. In each fit, we constrain in PPXF the velocity range to $V_{i,\rm start} - V_{\rm step}/2 \leq V_i \leq V_{i,\rm start} + V_{\rm step}/2$, where $i = 1, 2$ is the index for the two components. This means we force PPXF find the best solution in the interval around the starting value.

The result of this fitting are two-dimensional maps of $\Delta\chi^2$ (see left-hand panel of Fig. 2.3) and for each component maps of the weight (see right-hand panel of Fig. 2.3), velocity and dispersion. The $\Delta\chi^2$ map in the left-hand panel of Fig. 2.3 actually shows the cross-like structure centred on the single-component solution. The interpretation of this cross-like structure as the single-component solution is supported by the fact that in these regions mostly one component contributes to the fit, as the weight map indicates. The lowest $\Delta\chi^2$ region is symmetrically above and below the one-to-one relation. In those regions, the weight map reveals that both components contribute to the fit.

We select the two fits with the lowest $\Delta\chi^2$ values (because the fit should be symmetric to the one-to-one relation). The further analysis is complicated by the fact that PPXF outputs two results for each fit, one for each kinematic component, but the assignment of

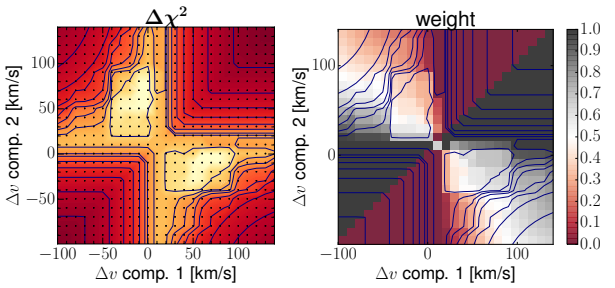

Figure 2.3: Left: $\Delta\chi^2$ as function of the input velocities for the two kinematic components. The contour lines are at $\Delta\chi^2 = 1, 4, 9$, after that the value doubles. The cross-like structure is the single-component solution. The best-fitting solutions are the bright areas with the lowest $\Delta\chi^2$ values. Right: weights for one kinematic component as function of the input velocities for the two kinematic components, with $\Delta\chi^2$ contours plotted. A true two-component solution is fitted in those regions where both components have a non zero-weight, i.e. brighter regions that are perpendicular to the one-to-one relation. The regions with the lowest $\Delta\chi^2$ fall on to those areas where both components contribute. The aforementioned single-component trails fall on regions where mostly one component contributes. For a better visualization these plots have a slightly higher sampling in velocity than our analysis, but this does not affect our results.

numerical component 1 and 2 is not related to the two physical components. This means for each fit we need to decide to which physical component (i.e. clockwise and counter clockwise rotating) the two numerical components belong.

We sort in such a way that the difference of the velocities of the two physical components $V_1 - V_2$ has the same sign as the major axis coordinate. After sorting velocity, velocity dispersion and weights, we adopt the mean of the two values from the two fits with the lowest $\Delta\chi^2$ as the final value.

In Fig. 2.4 we show the velocity fields. These plots show a clear separation of the two components and thus prove the existence of two counter-rotating populations. Component 1 rotates faster than component 2. Component 2 rotates in the same direction as the H I gas (van Woerden et al., 1993; Kamphuis et al., 2015). Here, the separation of the two components is purely based on a weighted superposition of the two kinematic templates. In Section 2.6.4, we determine the mass fractions of the two components based on our dynamical modelling.

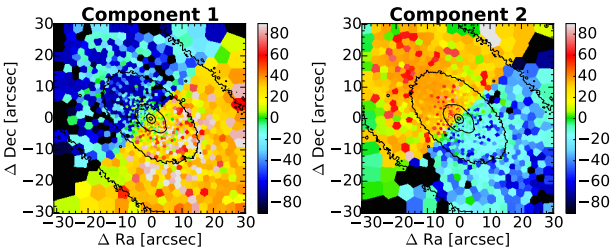

Figure 2.4: Left: velocity field of component 1 ($\mathrm{km\,s^{-1}}$). Right: velocity field of component 2 ($\mathrm{km\,s^{-1}}$). Black lines are the isophotes of the galaxy's integrated light.

2.4 Population fitting

We extract the stellar population from the MUSE data using PPXF to perform full-spectrum fitting and a regularization of the weights solution. To make use of the full wavelength range provided by the MUSE spectrograph (4750–9340 Å), we used the MIUSCAT (Vazdekis et al., 2012) population models. These models combine the observational stellar libraries MILES (Sánchez-Blázquez et al., 2006; Falcón-Barroso et al., 2011), Indo–US (Valdes et al., 2004) and CaT (Cenarro et al., 2001) to predict stellar populations over the wavelength range from 3465 to 9469 Å. MILES and CaT libraries are used in their respective wavelength ranges and Indo-U.S. in the gaps and at the blue and red extensions (Vazdekis et al., 2012).

We use stellar populations based on the Padova isochrones (Girardi et al., 2000) and use as a reference a Salpeter IMF. We restrict to the safe parameter range (Vazdekis et al., 2012) and obtain a set of population models covering the age range from 0.1 to 17.8 Gyr spaced into 46 logarithmically equidistant steps and six metallicites ([M/H] = −1.71, −1.31, −0.71, −0.4, 0.0, +0.22). All template spectra are scaled with one scalar to have a median value of 1. The same is done for the galaxy spectrum.

The whole MUSE wavelength range is used for the population fitting, no masking is applied. We simultaneously fit the stellar kinematics, population and the gas emission lines of Hα, Hβ, [O I] $\lambda\lambda$ 6300,6364, [O III] $\lambda\lambda$ 4959,5007, [N II] $\lambda\lambda$ 6548,6583, [S II] λ 6716 and [S II] λ 6731. The flux ratios of the doublets are fixed to 1/3 as predicted by atomic physics. All gas emission lines have a common kinematic (V and σ) solution, while the fluxes of the seven gas components (three doublets and four lines) are freely scaled.

We assume the errors on the spectrum to be constant with wavelength. We use the χ^2 per degree of freedom (χ^2/DOF) provided by the best fit to renormalize the error to give a $\chi^2/\mathrm{DOF} = 1$:

$$\varepsilon_{\mathrm{norm}} = \varepsilon \times \sqrt{\chi^2/\mathrm{DOF}}. \tag{2.1}$$

After the unregularized fit, we perform a regularized fit, with the PPXF regularization parameter 'REGUL = 100'.

Two examples of the regularized fit are shown in Figs. 2.5 and 2.6 for a central bin and one at a major axis radius of $r = 30.8$ arcsec, slightly more than one R_{e}. In the centre bin, two distinct populations emerge: an old, metal-poor one with $[M/H] < -1.0$ and a ~ 0.3 Gyr roughly solar metallicity ($[M/H] > -0.5$) one. In the outer bin, the separation is less prominent, even though there is an indication for a separation in metallicity.

For each Voronoi bin, the average age and metallicity are calculated as the weighted sums of the individual simple stellar population values

$$\log(\mathrm{Age}) = \frac{\sum_i w_i \log(\mathrm{Age}_i)}{\sum_i w_i} \tag{2.2}$$

$$[M/H] = \frac{\sum_i w_i [M/H]_i}{\sum_i w_i}. \tag{2.3}$$

The index i runs over the simple stellar populations and w_i is the weight PPXF assigned to the i-th population. Since MIUSCAT populations are normalized to an initial mass of $1\,\mathrm{M}_\odot$, these mean values are mass weighted. Mass-to-light ratios are computed from the MIUSCAT mass (Vazdekis et al., 2012) and photometry predictions (Ricciardelli et al., 2012) following equation 2 of Cappellari et al. (2013b)

$$(M_*/L)_{\mathrm{Salp}} = \frac{\sum_i w_i M_i}{\sum_i w_i L_i}. \tag{2.4}$$

Fig. 2.7 shows the mean age, metallicity and $(M_*/L)_{\mathrm{Salp}}$ maps of NGC 5102. The age map shows a young (~ 0.8 Gyr) population in the centre which is in line with the literature (e.g. Davidge, 2015). A relatively flat mean age of ~ 2 Gyr is observed in the outer parts, as reported by Davidge (2015) for the bulge of NGC 5102. There is a slight indication that the mean age decreases at the largest radii. The metallicity map reveals that the highest metallicity population is found in the centre while towards the outer parts the value drops from slightly below solar to $[M/H] = -0.5$. The high-metallicity population we see in the centre of NGC 5102 is in stark contrast to previous studies, since Davidge (2015) finds a metallicity of $Z = 0.004$ ($[M/H] \sim -0.7$) for the nucleus.

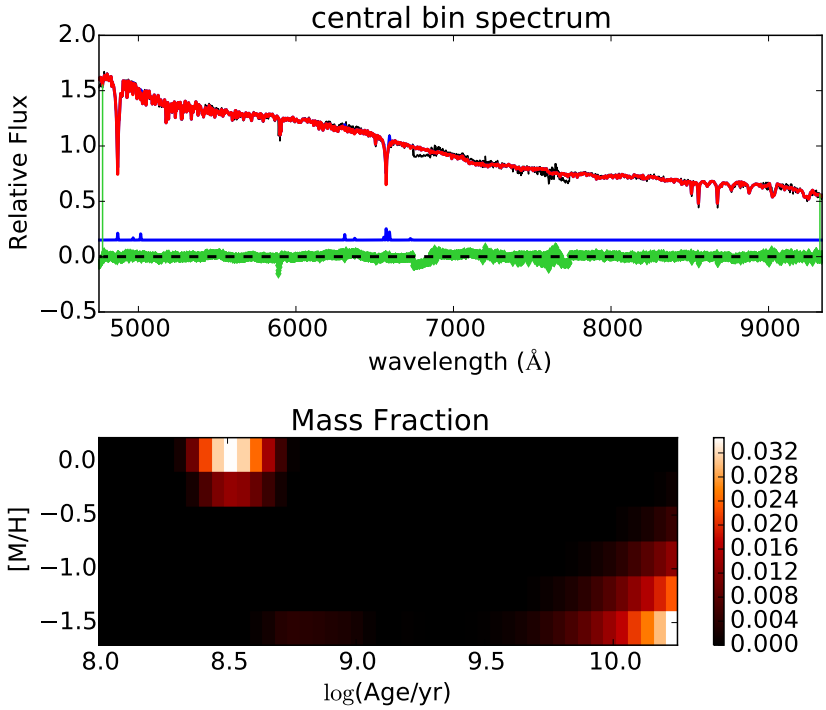

Figure 2.5: Top: the spectrum of a centre bin is shown in black. The red line shows the best regularized population fit to each spectrum. The blue line gives the best-fitting solution for the gas component. The green line shows the residuals (data − stellar model − gas model). Bottom: two-dimensional grid in age and metallicity spanning the parameter range of the stellar SSP models. The colour coding gives the weight each model contributes to the fit in the upper panel. This gives the distribution of stellar parameters.

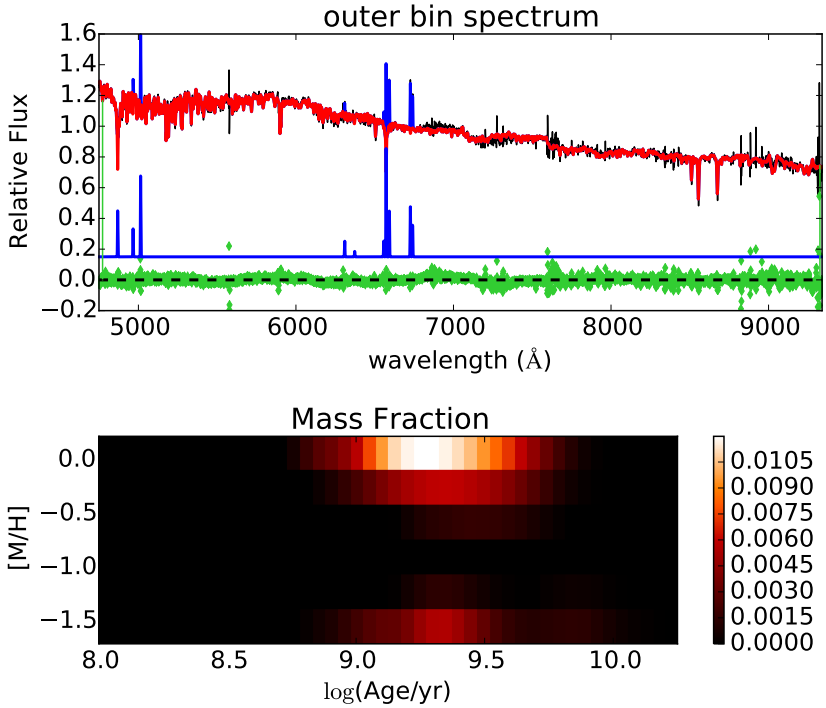

Figure 2.6: As Fig. 2.5, but for an outer Voronoi-bin at 30.8 arcsec from the centre.

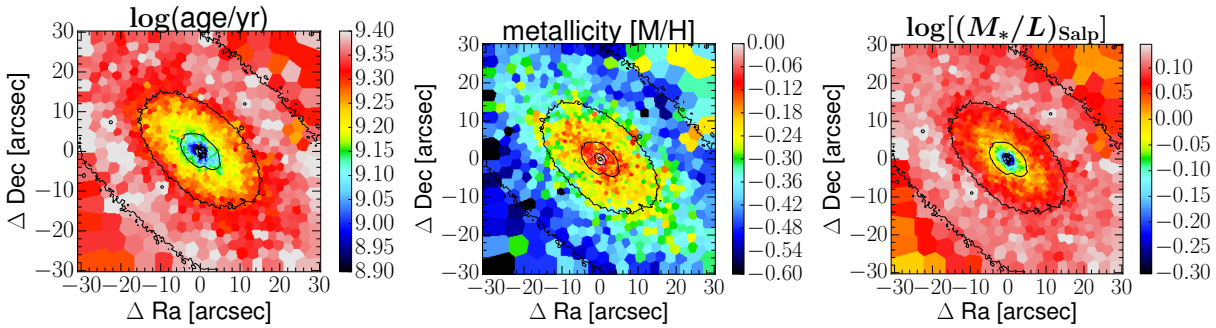

Figure 2.7: Left: regularized mass weighted log(Age) [log(yr)] field. Middle: regularized mass weighted metallicity $[M/H]$ field. Right: regularized $(M_*/L)_{\rm Salp}$ field. Black lines are the isophotes of the galaxy integrated light.

2.5 Photometry

There are two selection criteria for the photometric data for the dynamical models: to properly describe the distribution of the kinematic tracer the photometry has to be within the MUSE wavelength range and the photometric system needs to be well calibrated. In the *HST* archive, there are two image sets that fulfil these criteria, both are taken with the Wide Field and Planetary Camera 2 (WFPC2) in the $F569W$ and the $F547M$ filter. The $F569W$ data are preferred for two reasons: the photometry is deeper because of the larger bandwidth and the longer integration time and is a mosaic of two fields. The problem with this data set is that the galaxy centre is saturated. We therefore use the $F547M$ Planetary Camera (PC) image and add the $F569W$ at radii larger than 6 arcsec from the galaxy centre to avoid the saturated pixels.

When extracting the surface photometry of NGC 5102 on the $F547M$ wide field (WF) images, we discovered that the sky was over-subtracted by the standard pipeline. We determined the amount of over subtraction by requiring the profiles to be a power-law at large radii. For the PC image, the sky level is $-0.14\,\mathrm{counts\,s^{-1}}$ and the resulting surface photometry is shown in blue in Fig. 2.8. For the $F569W$ WF image, we found a sky level of $-0.01\,\mathrm{counts\,s^{-1}}$.

The WFPC 2 PC point spread function (PSF) is modelled using the dedicated software TINYTIM version 7.5 (Krist, 1993; Krist et al., 2011). The input spectrum is chosen to be a blackbody of 5700 K, because this approximates the NGC 5102 spectrum in the wavelength range of the $F547M$ filter. The resulting PSF-image is approximated by four two dimensional circular Gaussian functions using the Multi-Gaussian Expansion method (MGE; Emsellem et al., 1994; Cappellari, 2002).

For the dynamical models, we parametrize the

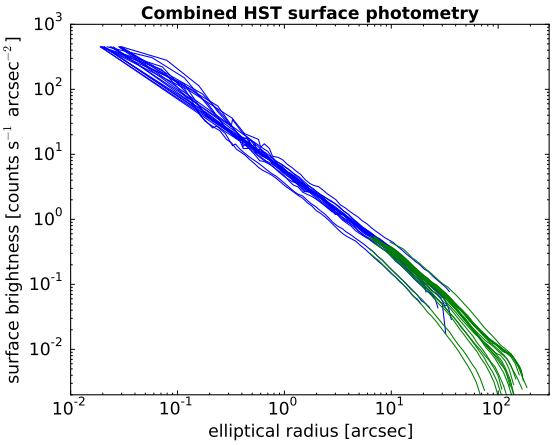

Figure 2.8: Photometry of two filters/instruments is shown: $F547M$ PC photometry in blue and $F569W$ WF in green. The different lines are the surface photometry from different sectors. The match of the photometry from the two filters/instruments shows that the scaling works.

galaxy surface brightness using the MGE. We use the FIND_GALAXY PYTHON routine[2] (Cappellari, 2002) to determine the galaxy centre and position angle. The surface photometry is measured in sectors equally sampled in eccentric anomaly (5°) and logarithmically sampled in radius, using the MGE_FIT_SECTORS[2] software of Cappellari (2002). The photometry of the four quadrants is averaged by the code. This allows for a simple combination of photometry from different images. To combine the different photometric data sets, we have to scale the $F569W$ photometry to match the $F547M$ calibration. This scaling takes the differences in pixels size, sensitivity and bandwidth of the filters into account. We found that the $F569W$ fluxes need to be multiplied by 0.13 to match the $F547M$ photometry. The resulting combined photo-

Table 2.2: MGE parametrization of NGC 5102 V-band stellar surface brightness.

log(surface density) [log($L_\odot$ pc^{-2})]	log(σ) [log($''$)]	q
6.932	−1.491	0.783
5.807	−1.096	0.900
5.133	−0.667	0.666
4.722	−0.278	0.636
4.164	+0.055	0.739
3.856	+0.380	0.609
3.415	+0.754	0.601
2.926	+0.958	0.663
2.587	+1.232	0.453
2.636	+1.413	0.473
2.145	+1.902	0.400

metry is shown in Fig. 2.8.

To correct the MGE model for PSF effects, we use the intensities and standard deviations of the MGE extraction of the PSF-image (for details see Cappellari, 2002). The regularized[3] MGE expansion along selected angular sections of the combined photometry is shown in Fig. 2.9 and the isophotes of the data and the model are compared in Fig. 2.10. Both plots show that the extraction did work very well, even out to the largest radii no problems are visible.

The output of the MGE (total counts, standard deviation and axial ratio for each Gaussian) is transformed into peak surface densities ($L_\odot$ pc^{-2}) using the *HST* photometric calibration of Dolphin (2009) for gain = 14. The $V - I = 0.93$ colour is computed from the $V = 11.18$ (mean value, Sandage & Visvanathan, 1978) and $I = 10.25$ (Doyle et al., 2005) magnitudes listed on NASA/IPAC Extragalactic Database (NED). The $F547M$ data were read out with gain = 15, which is accounted for by using the gain ratio term of Holtzman et al. (1995). We also correct for the galactic extinction towards NGC 5102 using $A_V = 0.151$, the value given by NED (Schlafly & Finkbeiner, 2011). For the transformation from surface brightness to surface density, the absolute V-band magnitude of the sun is needed and we use the value given by Blanton & Roweis (2007) $M_{\odot,V} = 4.78$.

The resulting MGE parametrization of NGC 5102 is given in Table 2.2. Following equation 11 of Cappellari et al. (2013a), we compute from the MGE a

[3] The regularization aims at finding the roundest solution that is in agreement with the errors on the photometry by first iteratively increasing the minimum boundary for the q value, to remove very flat components that are not justified by the data, and then lowering the upper bound on q to remove very round low surface brightness components that do not contribute to the χ^2 as in Scott et al. (2013).

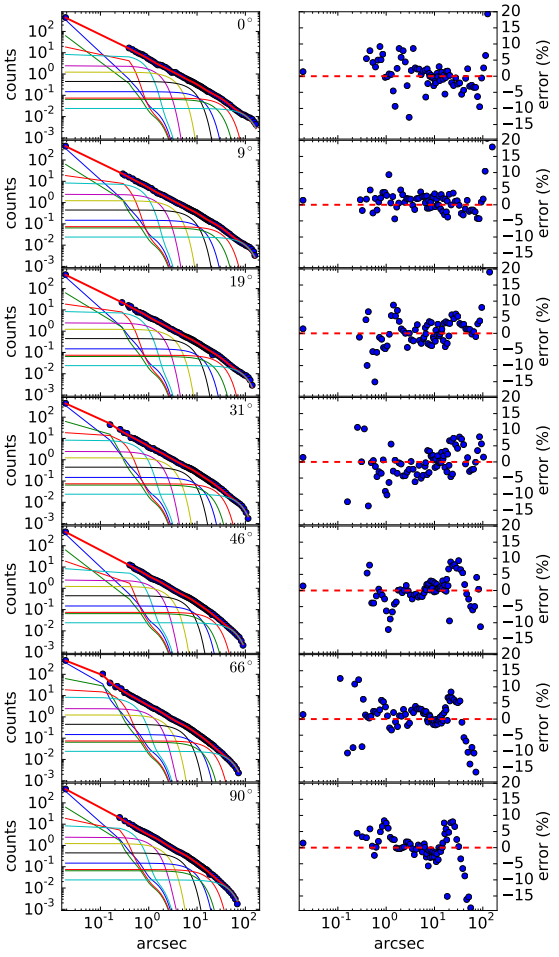

Figure 2.9: Right column: for a number of sectors the combined $F547M$ PC and $F569W$ WFPC2 photometry (blue points) and MGE model is shown. Left column: the residuals for the photometry are shown. There are no consistent structures in the residuals visible – indicating that the MGE model approximates the data well.

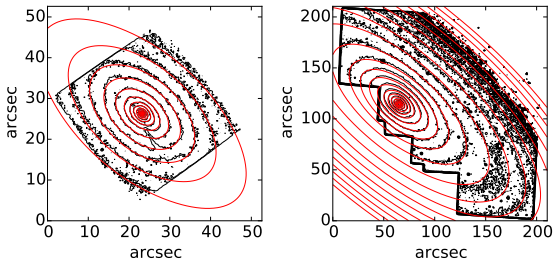

Figure 2.10: Isophotes from the data (black) and the MGE model (red) are shown. On the left-hand panel for the $F547M$ PC image and on the right-hand panel for the $F569W$ WFPC2 images.

total apparent V-band magnitude of $M_V = 9.74$ mag and a circularized effective radius of $R_e = 27.4$ arcsec. The RC3 value for the total apparent V-band magnitude is $M_V = 9.63$ mag.

The results from the population fitting showed that NGC 5102 has a prominent $(M_*/L)_{\rm Salp}$ trend in the sense that the light distribution is more strongly peaked than the mass distribution. To calculate a prediction of the *stellar mass* distribution, we multiply the observed surface brightness by $(M_*/L)_{\rm Salp}$. We use the $(M_*/L)_{\rm Salp}$ values displayed in Fig. 2.7 and compute the elliptical radius for each value according to

$$r_{\rm ell} = \sqrt{x^2 + y^2/\bar{q}^2}, \tag{2.5}$$

where the x-axis is aligned with the major axis and the coordinates are centred on the galaxy centre. $\bar{q}$ is the mean axial ratio from the MGE light extraction in Table 2.2. We fit these data with the following expression:

$$M_*/L(r_{\rm ell}) = (M_*/L)_0 + \Delta(M_*/L)\,[1 - \exp(-r_{\rm ell}/\tau)] \tag{2.6}$$

with three free, positive parameters: the difference in the mass-to-light ratio between the centre and the outer parts is $\Delta(M_*/L) = 0.825$, the mass-to-light ratio in the centre is $(M_*/L)_0 = 0.486$ and the scaling factor is $\tau = 6.758$. The best fit is shown in Fig. 2.11, underlining that this simple formula is actually a good approximation of the measured $(M_*/L)_{\rm Salp}$ values. The surface photometry obtained by SECTORS_PHOTOMETRY is sampled within a set of radial sectors. At any given $r_{\rm ell}$ (equation 2.5), we multiply the derived surface brightness by the $(M_*/L)_{\rm Salp}(r_{\rm ell})$ [equation 2.6] and fit a MGE model with the MGE_FIT_SECTORS procedure. In this way the MGE represents the stellar mass, rather than luminosity, assuming a Salpeter IMF. The MGE stellar mass parametrization of NGC 5102 is given in Table 2.3.

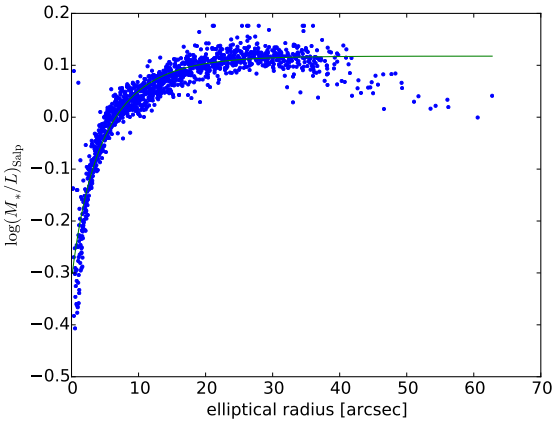

Figure 2.11: $(M_*/L)_{\rm Salp}$ from the regularized population fit (see Fig. 2.7) as function of the major axis radius. The best-fitting model to the data is shown in green.

Table 2.3: MGE parametrization of the NGC 5102 stellar mass surface density. The surface mass is computed by multiplying the photometry with the $(M_*/L)_{\rm Salp}$ parametrization, see equation (2.6).

log(surface density) [log($M_\odot$ pc^{-2})]	log(σ) [log($''$)]	q
6.659	−1.491	0.650
5.720	−1.138	0.650
4.941	−0.695	0.650
4.451	−0.280	0.650
3.869	+0.103	0.650
3.626	+0.387	0.601
3.317	+0.794	0.564
2.950	+0.985	0.627
2.631	+1.262	0.447
2.736	+1.414	0.472
2.263	+1.902	0.400

2.6 Jeans anisotropic modelling

We use the Jeans Anisotropic Modelling[2] (JAM; Cappellari, 2008) approach to compare our kinematic measurements with the predictions from modelling the mass distribution of the galaxy. This modelling approach allows the inclusion of the stellar mass inferred from the MGE, DM haloes and multiple kinematic components to constrain the potential of the galaxy. The JAM method makes some observationally motivated, but non-general assumptions on the dynamics of the models. This may in principle affect our conclusions on the total mass profile. However, the JAM approach was shown to be able to recover total mass profiles with high accuracy and negligible bias, both using realistic, high-resolution N-body simulations (Lablanche et al., 2012), cosmological hydrodynamical simulations (Li et al., 2016) and when compared to more general dynamical models (Cappellari et al., 2015). The mass profiles recovered by JAM at large radii in Cappellari et al. (2015) were also recently independently confirmed, with remarkable accuracy, using H I gas kinematics (Serra et al., 2016). All these tests motivate our use of JAM models in this paper.

2.6.1 Modelling approach

We use JAM models to predict the second velocity moment from the photometry and compare to the

$$V_{\rm rms} = \sqrt{V^2 + \sigma^2} \tag{2.7}$$

measured from the kinematics. The error on the observed $V_{\rm rms}$ is computed via error propagation as

$$\varepsilon_{V_{\rm rms}} = \frac{1}{V_{\rm rms}} \sqrt{(V\varepsilon_V)^2 + (\sigma\varepsilon_\sigma)^2}. \tag{2.8}$$

To prevent the model from being too strongly influenced by the high-S/N spaxels in the nucleus we do not use the true kinematics errors, instead we proceed as follows: the error on the velocity is initially assumed to be constant with $\varepsilon_V = 5\,{\rm km\,s^{-1}}$ and the error on the velocity dispersion to be a constant fraction $\varepsilon_\sigma = 0.05\sigma$. To ensure a proper normalization of the model uncertainties the errors are scaled after the best fit was obtained. We scale by a constant to have $\chi^2/{\rm DOF} = 1$ for the best-fitting model (model e, see below), following equation (2.1).

The large number of $V_{\rm rms}$ measurements from the MUSE data challenge the interpretation of the results: as van den Bosch & van de Ven (2009) note, in these cases the standard deviation of χ^2 itself becomes non-negligible. For this reason, we follow their approach and conservatively increase $\Delta\chi^2$ required to reach a given confidence level, taking the χ^2 uncertainty into account. We note that this approach is not statistically rigorous, but appears necessary to avoid unrealistically small errors in modelling fits with thousands of observables and gives sensible results. However, as our errors are based on Markov chain Monte Carlo (MCMC) [see below] rather than χ^2 contours, we need to scale the errors to reach the same effect as increasing the $\Delta\chi^2$ level. The standard deviation of χ^2 is $\sqrt{(2(N-M)}$ with N data points and M free parameters. To include this uncertainty in the MCMC sampling, the error needs to be increased in such a way that a 'miss fit' with a $\Delta\chi^2 = \sqrt{2N}$ with the original errors results in a fit with $\Delta\chi^2 = 1$ with the increased errors. Considering that multiplying all errors by ε, the χ^2 decreases by ε^2, a decrease of the χ^2 by $\sqrt{2N}$ is obtained by multiplying all errors by $(2N)^{1/4}$. This scaling is exactly equivalent to redefining the $\Delta\chi^2$ confidence level.

We use five different sets of models as follows.

(a) Self-consistent JAM model: we assume that the mass follows the light distribution, described by the MGE surface brightness extraction (see Table 2.2). This model has three free parameters that are fitted to match the observed $V_{\rm rms}$: the anisotropy parameter[4] $\beta_z = 1 - \sigma_z^2/\sigma_R^2$ and the inclination i which uniquely define the shape of the second velocity moment and the mass-to-light ratio $(M/L)_{\rm dyn}$, which is a linear scaling parameter used to match the JAM model to the measured $V_{\rm rms}$.

(b) Stars-only JAM model: in this model, we make an explicit distinction between (i) the distribution of the kinematic tracer population, which is parametrized using the MGE fitted to the stellar surface brightness in Table 2.2 (as in model a) and (ii) the stellar mass distribution, which is described using the MGE in Table 2.3, which accounts for the spatial variation in $(M_*/L)_{\rm Salp}$. This model is motivated by the observed strong $(M_*/L)_{\rm Salp}$ gradient, that makes the assumption of a constant (M_*/L) in model (a) quite inaccurate. Again this model has three free parameters: the anisotropy β_z and the inclination i that shape the second velocity moment and a global scaling factor $\alpha = (M/L)_{\rm dyn}/(M_*/L)_{\rm Salp}$, with $(M/L)_{\rm dyn}$ being the *total mass*-to-light ratio in the dynamical JAM model.

(c) JAM model with NFW DM halo: like in model (b), we distinguish (i) the distribution of the kinematic tracer population, which is parametrized using the MGE in Table 2.2 and (ii) the stellar mass distribution, which is described using the MGE in Table 2.3. However, we now also include the contribution of an NFW DM halo (Navarro et al., 1996). Assuming the DM halo is spherical, the double power-law NFW profile has two free parameters: the virial mass M_{200} and the concentration c_{200}. We use the virial mass–concentration M_{200}–c_{200} scaling relation of Klypin et al. (2011) derived from simulations to reduce the number of free parameters for the halo to one. The details of the scaling relation do not influence our results because the break radius of the halo lies at much larger radii than where we have our kinematics, and this implies that we would obtain essentially the same results if our halo was a single power-law. The JAM model with an NFW DM halo has then four free parameters: the anisotropy β_z, the inclination i, the IMF normalization $\alpha_* = (M_*/L)_{\rm dyn}/(M_*/L)_{\rm Salp}$ and the virial mass of the NFW halo M_{200}. Given that the stellar mass was computed from the spectral fits assuming a Salpeter IMF, any extra mass scaling can be interpreted as a difference in the IMF mass normalization.

(d) JAM model with generalized gNFW DM halo (e.g. Wyithe et al., 2001): the only difference between this model and model (c) is that we replace the NFW DM halo by a generalized NFW profile. Instead of forcing the inner slope of the halo to be -1, we introduce a free inner halo exponent γ, but force the

[4] In a cylindrical coordinate system with the cylinder axis aligned with the rotation axis of the galaxy, σ_z is the velocity dispersion parallel to the cylinder axis and σ_R is the velocity dispersion parallel to the radial axis.

outer slope to be -3. The matter density ρ is then described by

$$\rho(r) = \rho_s \left(\frac{r}{r_s}\right)^{\gamma} \left(\frac{1}{2} + \frac{1}{2}\frac{r}{r_s}\right)^{-\gamma-3} \tag{2.9}$$

where ρ_s is the normalization of the halo and r_s is the break radius. The break radius is outside the range covered by our kinematic data and should not affect the results at all. In line with Cappellari et al. (2013a), we choose a break radius of $r_s = 20\,\mathrm{kpc}$. This model has five free parameters: the anisotropy β_z, the inclination i, the inner halo slope γ, the DM fraction f_{DM} and the IMF normalization α_*.

(e) JAM model with a power-law *total* mass density: in this approach, we assume the stars (parametrized by the MGE in Table 2.2) are just a tracer population within a total mass distribution which we assume to be spherical and described by a power-law, within the region where we have kinematic information (and with a break at large radii). In particular, we do not make the standard assumption that the total mass is the sum of a luminous and dark component with specific parametrizations. In practice we describe the *total* mass density by equation (2.9). We are not aware of the use of this approach in stellar dynamical studies, but it was extensively used before in strong gravitational lensing studies of density profiles (e.g. Koopmans et al., 2009). The conceptual advantage of this approach is that it does not require any assumption regarding the *stellar mass* distribution, which can be quite uncertain due to the variations in M_*/L of the stellar population, including possible radial variations in the IMF. A motivation for its use comes from the finding that, even when the dark halo is allowed to be quite general, the *total* density profiles of ETGs are well approximated by a single power-law out to about 4 R_{e} (Cappellari et al., 2015). This model has four free parameters: the anisotropy β_z, the inclination i, the inner *total* mass density slope γ and the *total* mass density at 1 kpc $\rho(r = 1\,\mathrm{kpc})$. We choose $\rho(r = 1\,\mathrm{kpc})$ as free parameter to reduce the degeneracy between the halo normalization and the halo slope. Numerically it is straightforward to replace ρ_s in equation (2.9) with $\rho(r = 1\,\mathrm{kpc})$, while we keep $r_s = 20\,\mathrm{kpc}$.

In all models, the central region with a radius of $r = 2\,\mathrm{arcsec}$ is masked. In this region, a sharp σ peak is observed that influences the derived model parameters in a non-physical way. The necessary detailed modelling of the central black hole is beyond the scope of this paper. For all five models (a)–(e), the JAM model parameters are obtained using an MCMC sampling. The MCMC sampling is done using the Foreman-Mackey et al. (2013) EMCEE PYTHON code, an implementation of Goodman & Weare (2010) affine invariant MCMC ensemble sampler. There are basically two inputs to EMCEE: the prior function P(model) and the likelihood function P(data—model). We use an uninformative prior function, i.e. within the bounds the likelihood is 1, outside it is 0. Assuming Gaussian errors, the likelihood function is

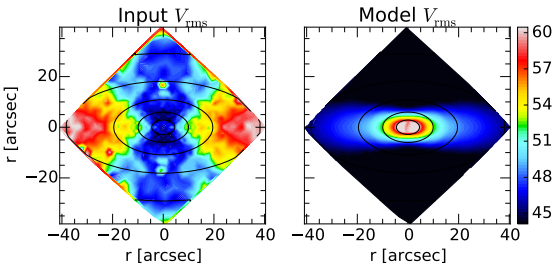

Figure 2.12: Self-consistent JAM model (a) second velocity moment (right-hand panel) is compared to the measured V_{rms} (left-hand panel). The model is completely unable to describe the observations. The values on the colour-bar are in $\mathrm{km\,s^{-1}}$.

$$P(\mathrm{data}|\mathrm{model}) \propto \exp\left(-\frac{\chi^2}{2}\right) \tag{2.10}$$

$$\chi^2 = \sum \left(\frac{V_{\mathrm{rms}} - \langle v_{\mathrm{los}}^2\rangle^{1/2}}{\varepsilon_{V_{\mathrm{rms}}}}\right)^2, \tag{2.11}$$

where $\langle v_{\mathrm{los}}^2\rangle$ is the second moment of the JAM model velocity distribution. The posterior distribution is then

$$P(\mathrm{model}|\mathrm{data}) \propto P(\mathrm{data}|\mathrm{model}) \times P(\mathrm{model}). \tag{2.12}$$

We use 100 walkers, each performing 500 steps to sample the posterior distribution.

2.6.2 JAM models of NGC 5102

The best-fitting self-consistent JAM model (a) is compared to the observed V_{rms} in Fig. 2.12, the median values of the posterior distribution are given in Table 2.4. It is obvious that the model does not at all represent the observed V_{rms}. This result is in contrast to the results obtained by Cappellari et al. (2013a) who apply the same approach to the 260 ATLAS^{3D} galaxies (see their fig. 1), where all galaxies with good kinematic data are well described by the self-consistent model. This qualitatively indicates that NGC 5102, unlike the ATLAS^{3D} ETGs, is dominated by DM. It also shows that the DM must be more shallow than the stars, since otherwise the self-consistent model would still be able to produce an acceptable fit. These qualitative results will be quantified in the following.

Table 2.4: JAM model parameters. The table gives the median values from the JAM model MCMC posterior distribution. The errors are the larger of the two intervals: 16th to 50th and 50th to 84th percentile.

Model	β_z	i	$\log(M/L)$	$\log(\alpha)^a$	γ	$f_{\rm DM}$	$\log(\rho(r=1\,{\rm kpc}))$	χ^2/DOF^b
	–	(°)	[$\log(M_\odot/L_\odot)$]	–	–	–	[$\log(M_\odot\,{\rm pc}^{-3})$]	–
bounds	[0.0, 0.5]	[70., 90.]	[−0.6, 0.3]	[−0.6, 0.3]	[−2.0, 0.0]	[0, 1]	[−4.0, 1.0]	
(a)	0.09 ± 0.04	87 ± 3	0.05 ± 0.01	–	–	–	–	14.84
(b)	0.08 ± 0.03	87 ± 3	–	0.14 ± 0.01	–	–	–	5.42
(c)	0.18 ± 0.04	86 ± 3	–	-0.05 ± 0.03	–	0.37 ± 0.04	–	1.13
(d)	0.22 ± 0.05	86 ± 4	–	-0.21 ± 0.21	-1.4 ± 0.3	0.58 ± 0.16	–	1.02
(e)	0.27 ± 0.04	86 ± 4	–	–	-1.75 ± 0.04	–	-0.75 ± 0.03	1.00

[a] For models (c) and (d) $\alpha_* = (M_*/L)_{\rm dyn}/(M_*/L)_{\rm Salp}$, with $(M_*/L)_{\rm dyn}$ ratio of dynamical *stellar* mass-to-light ratio. For model (b) $\alpha = (M/L)_{\rm dyn}/(M_*/L)_{\rm Salp}$ with $(M/L)_{\rm dyn}$ the *total* mass in the dynamical JAM model.

[b] The χ^2/DOF values stated here give χ^2/DOF = 1 for the best-fitting model (e). This means these χ^2/DOF values are *not* scaled to account for the effects of the standard deviation of the χ^2 itself (see Section 2.6.1).

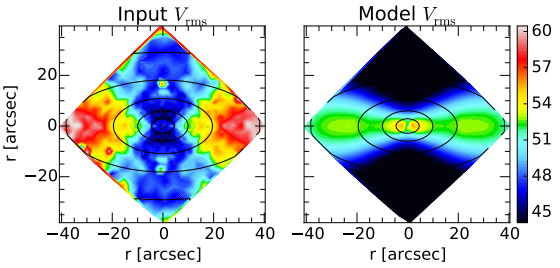

Figure 2.13: JAM model (b): the stars-only model second velocity moment (right-hand panel) is compared to the measured $V_{\rm rms}$ (left-hand panel). The fit is slightly better than in Fig. 2.12, but still the model is unable to describe the observations. The values on the colour-bar are in km s^{-1}.

The stars-only JAM model (b) shown in Fig. 2.13 differs noticeably from model (a) and represents a clear improvement but still at a poor overall level. Using the MGE *stellar mass* prediction instead of the simple mass-follows-light assumption moves the model into the right direction, but does not solve a more fundamental difference between data and model prediction. The median values of the posterior distribution are given in Table 2.4. Even though the χ^2/DOF of this model indicates a fair improvement over model (a), the quality of the JAM model is poor compared to the self-consistent models for the ATLAS$^{\rm 3D}$ galaxies (Cappellari et al., 2013a). It is obvious that the shallower mass profile used for this model can only reduce the DM needed to explain the kinematics of this galaxy, because the mass profile is shallower than the light profile and the DM halo has an even shallower slope than the mass profile.

Fitting model (c) with an NFW DM halo to the observed $V_{\rm rms}$ dramatically improves the quality of the JAM model. Fig. 2.14 compares the best-fitting JAM model with the NFW DM halo. Now the rise in velocity dispersion along the major axis and the flat $V_{\rm rms}$ along the minor axis are reproduced well by the model. The median model parameters from the posterior distribution are again summarized in Table 2.4. The mass $M(r)$ of an axisymmetric MGE enclosed within a sphere of radius r can be obtained as

$$M(r) = 4\pi \int_0^r r^2 \rho_{\rm tot}(r) {\rm d}r, \tag{2.13}$$

where the density $\rho_{\rm tot}(r)$ was given in footnote 11 of Cappellari et al. (2015). Using the same notation we obtain

$$M(r) = \sum_j M_j \left[{\rm erf}\,(h_j) - \frac{1}{e_j} \exp\left(-h_j^2 q_j^2\right) {\rm erf}\,(h_j e_j) \right] \tag{2.14}$$

with

$$e_j \equiv \sqrt{1 - q_j^2} \tag{2.15}$$

$$h_j \equiv \frac{r}{\sigma_j q_j \sqrt{2}}, \tag{2.16}$$

where the index j runs over the Gaussian components of the MGE model. Inside a sphere of radius $r = R_{\rm e}$, the DM fraction is $M_{\rm DM}(r)/M_{\rm tot}(r) = 0.37 \pm 0.04$.

For model (d), the posterior distribution from the MCMC sampling is shown in Fig. 2.15 and the median values are summarized in Table 2.4. This plot shows the expected degeneracy between the IMF normalization, the DM halo slope γ and the DM fraction. Due to the degeneracy, a range of parameter combinations gives nearly equally acceptable fits: from models with reasonable IMF normalizations to models that are mostly DM dominated [see also model e, as this is the limiting case of $\log(\alpha_*)$ going to −infinity and $f_{\rm DM}$ to 1]. A Salpeter IMF with an

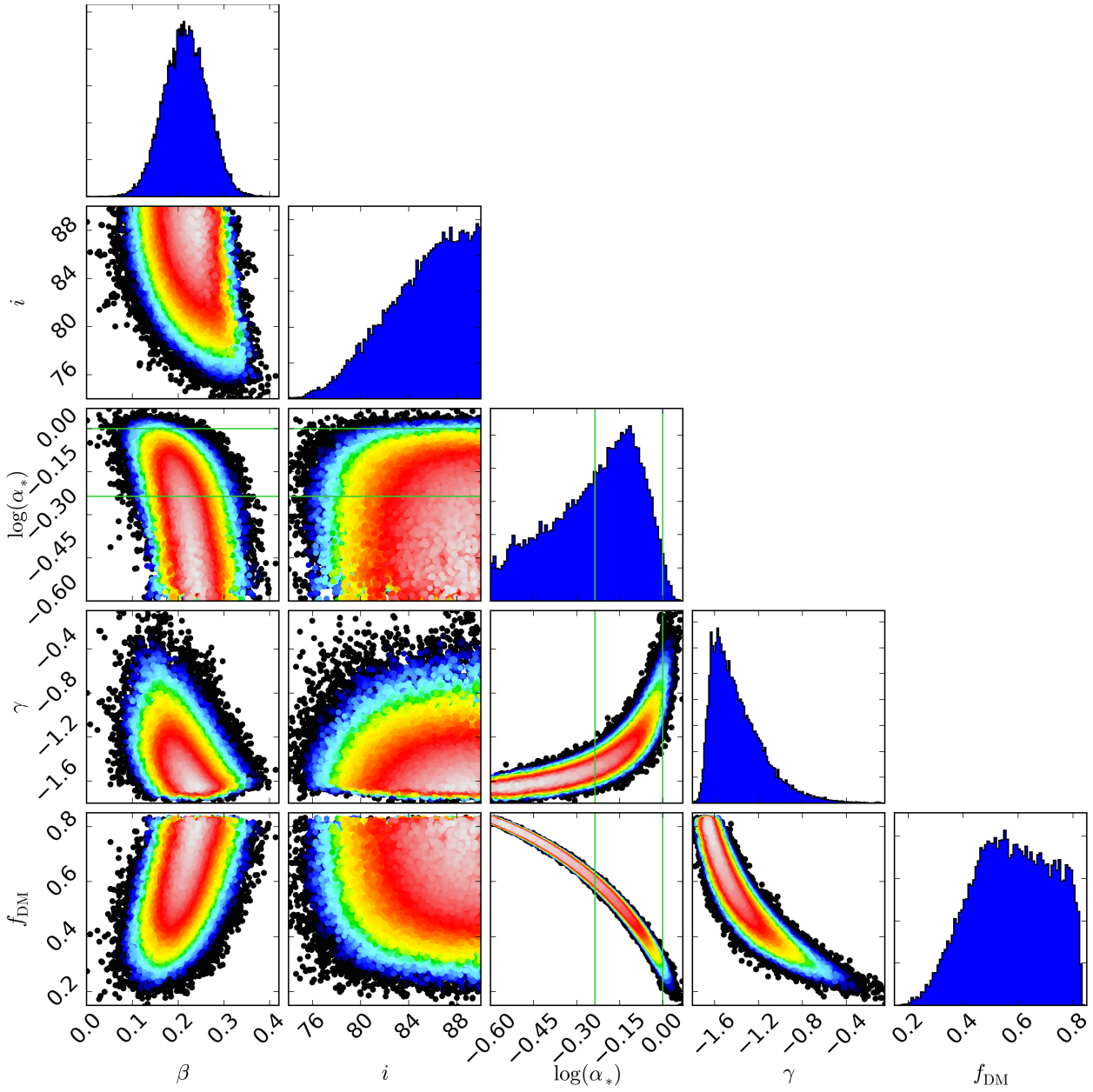

Figure 2.15: The posterior distribution of model (d) with an MGE mass model and a gNFW DM halo, i.e. a power-law halo with free inner slope and outer slope fixed to -3. The green lines correspond to a Salpeter IMF ($\log(\alpha_*) = 0$) and a Chabrier IMF ($\log(\alpha_*) = -0.236$). The colour coding gives the likelihood for the model parameters, with black points being disfavoured at 3σ or more. The sharp truncation of the DM fraction at $f_{\rm DM} \approx 0.83$ is caused by the lower boundary on the IMF normalization α_*, effectively introducing a lower limit for the stellar mass fraction.

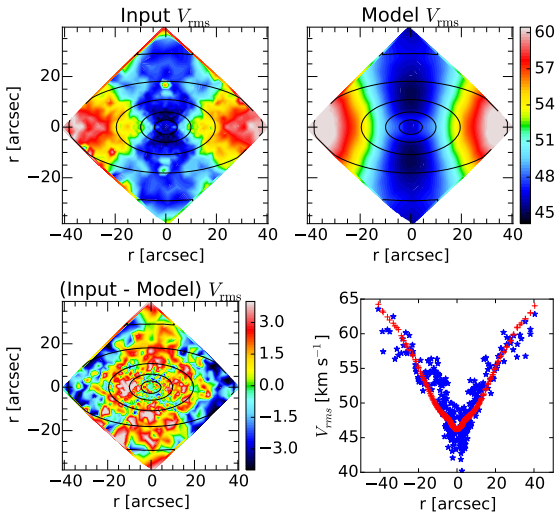

Figure 2.14: JAM model (c) [NFW halo and MGE stellar mass] second velocity moment. Top row: the symmetrized measured $V_{\rm rms}$ (left) is compared to the JAM model prediction (right). Bottom left: the plot shows the difference between measured and model $V_{\rm rms}$. Bottom right: a cut through the $V_{\rm rms}$ plane is shown, plotting all points with minor axis distances $-2.5 \leq r_{\rm min} \leq 2.5$. The blue stars are the measurements, the red crosses the JAM model. The values on the colour-bar are in km s^{-1}.

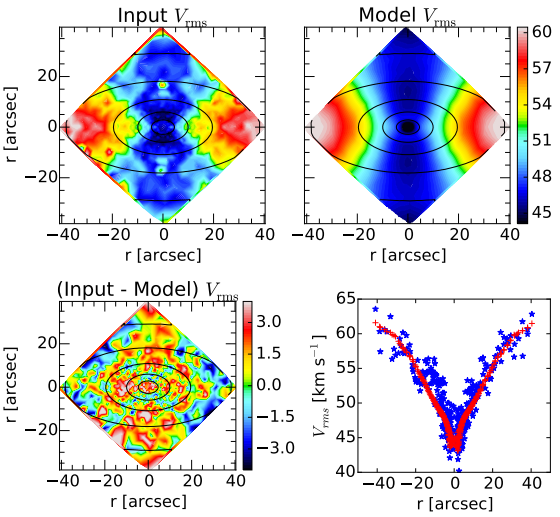

Figure 2.16: JAM model (e) [total mass is parametrized by a spherical power-law] second velocity moment. Top row: the symmetrized measured $V_{\rm rms}$ (left) is compared to the JAM model prediction (right). Bottom left: the plot shows the difference between measured and model $V_{\rm rms}$. Bottom right: a cut through the $V_{\rm rms}$ plane is shown, plotting all points with minor axis distances $-2.5 \leq r_{\rm min} \leq 2.5$. The blue stars are the measurements, the red crosses the JAM model. The values on the colour-bar are in km s^{-1}.

inner halo slope $\gamma = -1$ (i.e. model c) seems to be less likely. A model with a Chabrier IMF (i.e. a typical IMF for a low-mass galaxy) is in the range of high likelihood and requires a DM fraction of $f_{\rm DM} \approx 0.6$. In Fig. 2.15, we see a sharp truncation of the DM fraction at $f_{\rm DM} \approx 0.83$. We emphasize that this truncation is caused by our lower boundary on the IMF normalization α_*. The lower boundary on α_* is chosen at half the mass of a Chabrier IMF.

In model (e), we assume that the *total* matter distribution can be described by a power-law. Fig. 2.16 shows that this model actually gives the best description of the observed $V_{\rm rms}$, even though the improvement over the NFW model (c) is minor (see Table 2.4). This underlines that the simple assumption of a power-law matter distribution with spherical symmetry describes the observed $V_{\rm rms}$ well. The slope for the *total* mass density is a very robust result, in contrast to the slope of the dark halo that is degenerate with the IMF normalization. The slope $\gamma = -1.75 \pm 0.04$ we find for NGC 5102 is shallower than the slope of an isothermal halo ($\gamma_{\rm iso} = -2$). Cappellari et al. (2015) measure an average slope of $\langle\gamma\rangle = -2.19 \pm 0.03$ for the 14 fast-rotating galaxies out to large radii of $4R_{\rm e}$. The authors do not find a strong dependence of the slope on the radius and report a marginally smaller slope when limiting the radial range to $r \leq R_{\rm e}$. The smaller slope we find for the low-mass galaxy NGC 5102 agrees with the decreasing *total* mass slope reported by Cappellari (2016): fig. 22(c) shows a trend as a function of σ (dashed lines, with values given in fig. 20). The lowest σ in ATLAS$^{\rm 3D}$ is ~ 50 km/s, which is comparable to $\sigma_{\rm e} = 48$ of this galaxy. At that σ level the slope in ATLAS$^{\rm 3D}$ is ~ -1.9, so this galaxy would be almost consistent with that.

2.6.3 Decomposing the power-law profile

The advantage of model (e) is that it allows us to measure the *total* density profile, which is an important observable in itself, without the need to make *any* assumption about the DM contribution and its parametrization. This is the same situation as in studies of the circular velocity curves of ETGs with gas discs (e.g. Weijmans et al., 2008). However, once the total density or rotation curve has been obtained, in both cases extra assumptions are required to make inferences about the luminous and DM.

When measuring DM via this two-step process

(modelling of the total mass followed by mass decomposition), one should expect results that are generally similar to what one can obtain via the standard route of assuming a dark halo parametrization during the JAM fitting itself. However, the details of the two approaches are sufficiently different that this allow one to test for the robustness of the halo results.

The stellar mass density profile is computed from the axisymmetric MGE using Note 11 in Cappellari et al. (2015). The NFW density is computed following the approach detailed in model (c) in Section 2.6.1 and the power-law density is derived from the analytic expression in equation (2.9). This fitting has two free parameters: the logarithm of the IMF normalization $\log(\alpha_*)$ to scale the stellar mass density profile and the logarithm of the virial mass $\log(M_{200})$ of the NFW halo. For each individual fit, we assume constant relative errors on the total density, with arbitrary normalization. We emphasizes that we are using the NFW parametrization for the DM halo. From the results of the JAM models, one might prefer to use the gNFW parametrization, but that would not work: in the inner part (where we can constrain the model with our kinematic data), the gNFW is simply a power-law with free slope and normalization. Because we parametrized our *total* mass density with a power-law, this could be reproduced by the gNFW, without the need for any luminous matter – a result clearly in contrast to our observations.

We fit all realizations from the MCMC posterior distribution of the JAM model (e) to obtain a distribution in the two free parameters $\log(\alpha_*)$ and $\log M_{200}$. Fig. 2.17 shows 100 randomly chosen fits from the posterior distribution. The distribution of the parameters is shown in Fig. 2.18. From this posterior distribution we obtain $\log(\alpha_*) = 0.015 \pm 0.026$ and $\log(M_{200}) = 12.4 \pm 0.3$, which means the power-law decomposition prefers a slightly higher stellar mass then the JAM model (c) [Table 2.4] and accordingly a slightly lower DM mass. From the decomposition of the power-law model, we measure a DM fraction of $f_{\rm DM} = 0.30 \pm 0.04$, compared to $f_{\rm DM} = 0.37 \pm 0.04$ for model (c). Given the differences in the two methods to infer the DM fraction (JAM modelling and the power-law decomposition), the two values are in a good agreement and more important they give a sense for the systematic uncertainties that are difficult to estimate otherwise.

The colour coding in Fig. 2.18 gives the likelihood for the models with black points being disfavoured at 3σ or more. The fact that the coloured area has a different shape than the complete posterior sample indicates that not all power-law realizations can be described by the stellar mass distribution and an NFW DM halo. On the other hand, the best-fitting stellar plus NFW dark halo model seems to be poorly described by a power-law. This nicely emphasizes the systematic differences between the models.

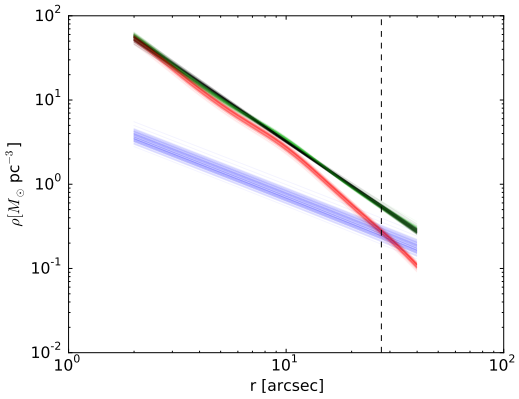

Figure 2.17: The solid black lines are 100 randomly selected power-law models from the posterior distribution of the JAM model (e). These are fitted with a combination of stellar mass density (red) and NFW DM halo (blue). The green line is the sum of luminous and dark component. We fit the power-law models in the range $2\,\mathrm{arcsec} \leq r \leq 40\,\mathrm{arcsec}$, where the lower limit is identical to the central masking radius used for the JAM modelling and the outer limit is the largest radius sampled by our kinematic data. The vertical (black, dashed) line marks $1R_\mathrm{e}$.

2.6.4 Mass decomposition of counter-rotating discs

To study the mass distribution, we only need the $V_{\rm rms}$. In this way, we can ignore how the stellar kinematics separates into ordered and random motions, and we do not need to make any assumptions about the tangential anisotropy. However, in order to study the mean velocity we need to make a choice for the tangential anisotropy.

In the JAM approach, the tangential anisotropy can be specified in two ways: (i) either by giving the σ_ϕ/σ_R ratio (equation 34 of Cappellari, 2008) or (ii) by quantifying the ratio κ between mean rotation of the model and a model with an oblate velocity ellipsoid (equation 35 of Cappellari, 2008).

The anisotropy of a JAM model can be different for each individual Gaussian of the MGE and this allows one to construct models with a nearly arbitrary mean rotation field, by assigning different tangential anisotropies. Here, we allow for κ to be different and in particular to have different signs for different Gaussians in order to model the counter-rotating discs in this galaxy.

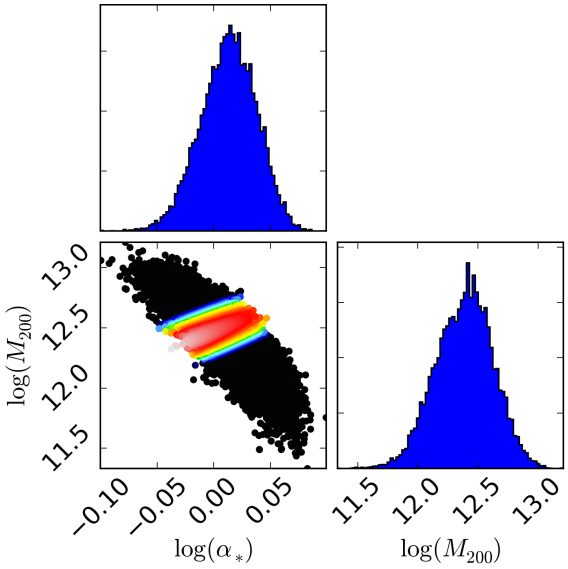

Figure 2.18: Corner plot showing the posterior distribution of M_{200} and IMF normalization α_* values as obtained by decomposing the JAM power-law model (e) into stellar and DM. The colour coding gives the likelihood for the model parameters, with black points being disfavoured at 3σ or more.

Similar examples of JAM models of a set of six fast-rotator ETGs with counter-rotating discs from the ATLAS^{3D} survey are presented in fig. 12 of Cappellari (2016).

We use the JAM model (c) [with MGE stellar mass model and NFW DM halo] to recover the velocity and dispersion of this model. We use a PYTHON implementation of the MP-FIT program (Markwardt, 2009) to fit the κ value of each Gaussian component, by minimizing the squared residuals between the observed and modelled velocity and dispersion fields simultaneously. This fit has 11 free parameters (i.e. the κ value of each of the 11 Gaussian components from the photometry given in Table 2.2). The resulting velocity and dispersion map are compared to the observed ones in Fig. 2.19.

The most prominent disagreement between data and model dispersion is the too steep rise of the model along the major axis. This is the same disagreement one can see in the $V_{\rm rms}$ in Fig. 2.14 and is caused by too much matter in the outer parts of the galaxy and indicative for a too shallow DM halo as illustrated by the fact that model (d) prefers a steeper halo slope than NFW.

The decomposition of the JAM $V_{\rm rms}$ in ordered and random motion can be used, with some assumptions, to estimate the mass fraction the two counter-rotating discs contribute to the total stellar mass. We start by writing the fitted κ_i value of the i-th Gaussian component as a linear combination of the intrinsic κ values of the two components:

$$\kappa_i = \kappa_i^{(1)} w_i^{(1)} + \kappa_i^{(2)} w_i^{(2)} \tag{2.17}$$

$$1 = w_i^{(1)} + w_i^{(2)} \tag{2.18}$$

To obtain a mass estimate from these two equations, we need to know the intrinsic κ values of the two discs. Since it is impossible to derive these from the data, we assume that the two counter-rotating discs have perfect oblate velocity ellipsoids, i.e. their intrinsic κ-values are $\kappa_i^{(1)} = 1$ and $\kappa_i^{(2)} = -1$. This assumption is motivated by the finding that fast-rotator ETGs as a class satisfy this assumption with high accuracy Cappellari (see fig. 11 of 2016). We then solve for the weights of each Gaussian component:

$$w_i^{(1)} = \frac{\kappa_i + 1}{2} \tag{2.19}$$

$$w_i^{(2)} = 1 - w_i^{(1)}. \tag{2.20}$$

The masses of the two components are the weighted sums of the total mass M_i of the Gaussians

$$M^{(1)} = \sum_i w_i^{(1)} M_i \tag{2.21}$$

$$M^{(2)} = \sum_i w_i^{(2)} M_i \tag{2.22}$$

We find a mass fraction of 40% for component 1 and 60% for component 2. These fractions refer to the total mass enclosed in our MGE mass model (Table 2.3) and are quite uncertain. The indication is that the two counter-rotating discs have roughly equal masses within the range of our photometry. This nearly equal contribution for the two discs is similar to what was found for the S0 galaxy NGC 4550, which has qualitatively similar kinematics and was also modelled in detail (Cappellari et al., 2007).

2.7 Discussion

2.7.1 Counter-rotating populations

We reliably showed that the 2σ appearance of NGC 5102 is due to two counter-rotating discs by disentangling their contribution to the LOSVD. We found that component 2 is more concentrated and rotates slower than component 1, but the resolution of the MUSE data is too low to reliably measure the rotation velocity. The H I gas has a regular rotation pattern with a flat outer rotation velocity of roughly 95 km s^{-1} (van Woerden et al., 1993; Kamphuis et al., 2015). The rotation axis of the gas is essentially

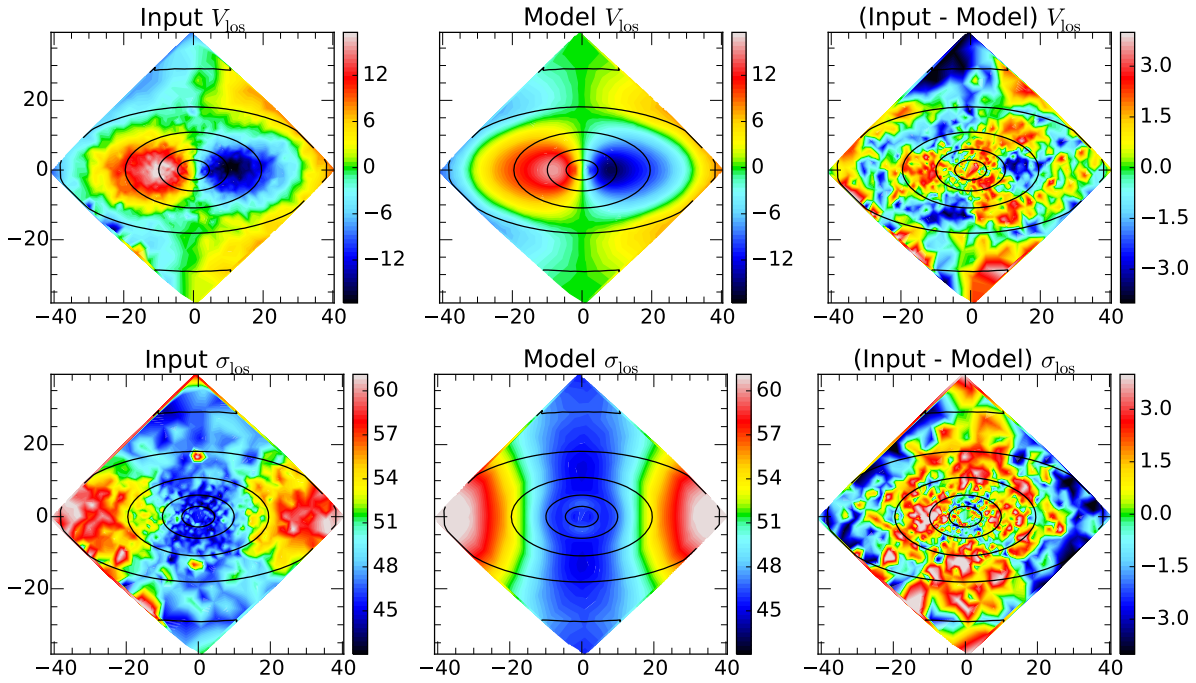

Figure 2.19: The best-fitting JAM model (c) $V_{\rm rms}$ prediction is decomposed in ordered (V) and random (σ) motion. Top panel: The measured V (left-hand panel, symmetrized version of Fig. 2.2) is compared to the predicted velocity field (middle panel). The right-hand panel shows the residuals. Bottom panel: the measured σ (left-hand-panel, symmetrized version of Fig. 2.2) is compared to the predicted dispersion field (middle) and the residuals are shown in the right-hand panel. The values on the colour-bar are in $\mathrm{km\,s^{-1}}$.

aligned with the rotation axis of the stars and the sense of rotation is identical to the more concentrated component 2.

It is very tempting to describe the formation of NGC 5102 by the following scenario: the less concentrated disc (component 1) was in place early on, when a cloud of H I gas with opposite momentum was swallowed by NGC 5102. Form this counter-rotating gas then the counter-rotating stellar disc was formed. This interpretation would need an investigation of the stellar population of the two counter-rotating discs, which is not possible with the spectral resolution of the MUSE spectra.

2.7.2 Population

The population fits show a strong gradient in age and metallicity, exhibiting in the centre a mass weighted mean age below 8×10^8 yr. The age gradient flattens at a mass weighted mean age of roughly 2.5×10^9 yr. The metallicity gradient we find is in contrast to previous studies, as e.g. Davidge (2015) based on index measurements finds no metallicity gradient.

Our age values are in broad agreement with the ages of 1 and 2 Gyr which Davidge (2015) finds for the nuclear and the bulge spectra by fitting SSP models with fixed metallicity of $Z = 0.004$ ($[\mathrm{Fe/H}] \approx -0.7$). In light of the strong metallicity gradient, we find the assumption of a constant metallicity questionable, but Davidge (2015) already notes that solar metallicity models would result in 0.3 dex younger ages.

Kraft et al. (2005) find a dominant old (3 Gyr) super-solar ($Z = 1.5$) population and a less prominent young (0.3 Gyr) metal-poor ($Z = 0.2$) population in the centre. Neither our work nor the one by Davidge (2015) can confirm a dominant metal-rich 3 Gyr population. There are several reasons for the mismatch: Kraft et al. (2005) use archival spectra from four different sources, which they stick together. This might introduce unknown systematic uncertainties in general and especially for NGC 5102: all spectra need to be exposed at exactly the same position, otherwise the strong population gradient makes the concatenated spectrum meaningless. There is not much experience in the literature with fitting spectra from the UV to the NIR, complicating the comparison of our results with the fit of Kraft et al. (2005) to the extended wavelength range from 2000 to 9800 Å.

The strong population gradients we observe might be influenced by the presence of the two kinematic components. To investigate this, a decomposition of the populations of the two counter-rotating discs

would be necessary. This decomposition works if the two components are well separated in their kinematics or have quite different populations. Such a decomposition is beyond the scope of this paper, but based on the spatial extent of the age and metallicity gradients we do see some indication that the two kinematic components have different stellar populations. In that case the more concentrated component 2 would have a young and metal-rich population, while the more extended component 1 would be older and metal-poor. Validating this indication would give interesting insights into the evolution of NGC 5102 and might also explain the strong $(M_*/L)_{\rm Salp}$ gradient.

2.7.3 JAM modelling

The strong disagreement of the self-consistent JAM models (a) (mass follows light) and (b) (stars only) with the data shows that this low-mass galaxy has a different DM content from most of the higher mass ATLAS^{3D} ETGs. The JAM models make strong assumptions about the galaxy that might not be fulfilled for real galaxies, especially that the velocity ellipsoid is aligned with cylinder coordinates. The fact that there is a large number of observed fast-rotating galaxies that can be approximated quite well, within $1R_{\rm e}$, using the self-consistent JAM models (e.g. Cappellari et al., 2013a) and further supported from the analysis of simulated galaxies (Lablanche et al., 2012; Li et al., 2016) makes it unlikely that anisotropy is driving the observed differences, and rather indicates a difference in the DM content.

Including an NFW DM halo into the JAM models brings the model and the data into good agreement. The DM fraction of 0.37 ± 0.04 we find is relatively high, as shown by the comparison with the DM fractions from Cappellari et al. (2013b) in Fig. 2.20. The model with an NFW DM halo requires a relatively heavy IMF, an unexpected result for this relatively low-mass galaxy. The more general model with a power-law DM halo with a free inner slope explains this result: the halo slope and the IMF normalization are degenerate and anti-correlated. These models favour a more Chabrier/Kroupa like IMF and a steeper than NFW dark halo slope, resulting in a larger DM fraction inside $1Re$. This matches with the results of Tortora et al. (2016) obtained on a sample of 39 Virgo cluster dwarf ETGs: DM fraction and IMF-normalization correction are anti-correlated and dwarf early-types have on average slightly more massive IMFs than Chabrier. This means that the DM fraction in Fig. 2.20 represents a lower limit to the DM fraction inside a sphere of $1R_{\rm e}$ in NGC 5102. A light IMF would be more consistent with the expectations from the IMF–σ relation, as indicated either by similar JAM models (Cappellari et al., 2012, 2013b; Posacki et al., 2015), or by stellar population models (Conroy & van Dokkum, 2012; Spiniello et al., 2012; Ferreras et al., 2013). However, the present results do not allow us to constrain the IMF normalization with significant accuracy.

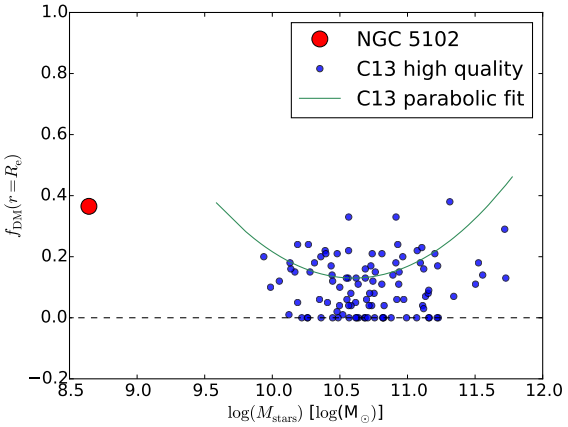

Figure 2.20: Comparison of the DM fraction inside a sphere of radius $r = R_{\rm e}$, assuming the halo has an NFW profile. The NGC 5102 value is from this paper (JAM model c), the blue circles (sub sample with high-quality kinematic data) are from Cappellari et al. (2013a, mass) and Cappellari et al. (2013b, DM fractions). The parabola $f_{\rm DM} = 0.13 + 0.24(\log M_{\rm stars} - 10.6)^2$ is the fit by Cappellari et al. (2013a) to the sample with NFW haloes, that have masses determined via M_{200}–$M_{\rm stars}$ scaling relations from simulations.

Previous literature values for the inclination of NGC 5102 are all based on axial ratios and make an assumption on the intrinsic flattening of the galaxy: 64.°4 (Davidge, 2008, intrinsic flattening unknown), 66° (Beaulieu et al., 2010, $q_{\rm intr} = 0.2$) and $70 \pm 6°$ (Kamphuis et al., 2015, $q_{\rm intr} = 0.2$ and adding a 3° offset). Assuming a flat disc, we compute a minimum inclination of 66.°3 from the flattest MGE ($q = 0.4$) in Tables 2.2 and 2.3. Our $q = 0.4$ is in good agreement with the value of $q = 0.38 \pm 0.03$ we obtain from the HyperLeda logr25 $= 0.42 \pm 0.04$ (Makarov et al., 2014). Even though the flattening of the outermost Gaussian in itself is not very robust, the comparison with the other sources shows that it is reasonable. The problem with inclinations estimated via axial ratios is the assumption of the intrinsic flattening that cannot be validated. Weijmans et al. (2014) determine that the mean *intrinsic* flattening of the ATLAS^{3D} fast-rotator galaxies is $q_{\rm intr} = 0.25$. Under this assumption and taking the HyperLeda ob-

served axial ratio the minimum inclination becomes 73°. This is even more important for dwarf galaxies that tend to be rounder. Sánchez-Janssen et al. (2016) determine the mean intrinsic axial ratio of Virgo dwarf galaxies to be $q_{\rm intr} = 0.57$ – even rounder than the observed one of NGC 5102. In summary, if the intrinsic axial ratio of NGC 5102 is intermediate between the ATLAS^{3D} and the Virgo dwarf galaxy value, it might well be that we see NGC 5102 edge-on. However, our constraints are not very tight and any inclination between 75° and 90° would be consistent with the data at 3σ confidence.

2.8 Summary

We analyse the kinematics and stellar population of the nearby low-mass S0 galaxy NGC 5102 with MUSE spectra. The data cover the central part of the galaxy, out to $1R_{\rm e}$ along the major axis. We fit Gaussian (two moment) and Gauss–Hermite (four moment) LOSVDs to two different wavelength regions (the overlap between MUSE and the MILES library and the Ca II triplet). For the first time we reveal that NGC 5102 is a 2σ galaxy, showing the typical two dispersion peaks along the major axis and at the same position a reversal of the sense of rotation. The results obtained in the two different wavelength regions agree within the expected uncertainties. The four moment extraction finds larger rotational velocity amplitudes, a sign for two counter-rotating discs in this galaxy.

We disentangle the rotation of the two counter-rotating discs by fitting the MUSE spectra with two independent Gaussian LOSVDs. The most likely explanation for the evolution of the two counter-rotating discs is that the more extended disc (component 1) was in place when gas with opposite momentum was swallowed by NGC 5102. The counter-rotating gas has been detected by van Woerden et al. (1993) and most likely created the counter-rotating disc. Unfortunately the resolution of the MUSE spectra is too low to fit individual populations for the two counter-rotating discs, as this would help in further constraining the evolution of this galaxy.

We fit the stellar population of NGC 5102. This fitting exhibits strong gradients in the mean stellar age, metallicity and the stellar mass-to-light ratio. The unusual blue bulge of NGC 5102 has been known since the early 1970s and was attributed to a young nuclear cluster. To our knowledge, a strong metallicity gradient has not been discussed in the literature yet. The extent of the young metal-rich population does not spatially coincide with the kinematic signature of the counter-rotating disc.

We modelled the dynamics of NGC 5102 using the JAM method. The JAM models using the simple mass-follows-light assumption, as well as the stars-only model, are not able to reproduce the observed stellar kinematics.

Including DM in the JAM models immediately solves the difficulties in reproducing the observed kinematics. The model with an NFW dark halo requires a DM fraction of 0.37 ± 0.04 inside a sphere of a radius of one $R_{\rm e}$ and a heavy IMF. Our model with a general NFW dark halo (i.e. a power-law halo with a free inner slope) shows that the DM fraction is degenerate with the IMF normalization. Nevertheless these models prefer a light weight IMF, steeper than an NFW dark halo slope and accordingly a higher DM fraction. Therefore, the indication is that the model with an NFW halo (and a relatively heavy IMF) is a lower limit to the DM fraction.

A more robust result than the dark halo slope is the slope of the *total* mass density. We model the mass density as a power-law and find excellent agreement with the data for a slope of -1.75 ± 0.04. This slope is shallower than the slope of an isothermal halo (-2) and also shallower than the slope Cappellari et al. (2015) report for higher mass fast-rotating galaxies. This agrees qualitatively with the finding of Cappellari (2016) that the halo slope decreases with decreasing stellar mass.

Acknowledgements

This work is based on observations collected at the European Organisation for Astronomical Research in the Southern Hemisphere under ESO programme 60.A-9308(A) and also based on observations made with the NASA/ESA *Hubble Space Telescope*, and obtained from the Hubble Legacy Archive, which is a collaboration between the Space Telescope Science Institute (STScI/NASA), the Space Telescope European Coordinating Facility (ST-ECF/ESA) and the Canadian Astronomy Data Centre (CADC/NRC/CSA). This research has made use of the NASA/IPAC Extragalactic Database (NED) which is operated by the Jet Propulsion Laboratory, California Institute of Technology, under contract with the National Aeronautics and Space Administration. We acknowledge the usage of the HyperLeda data base (http://leda.univ-lyon1.fr). We thank the anonymous referee for helpful comments. MM is grateful for financial support from the Leibniz Graduate School for Quantitative Spectroscopy in Astrophysics, a joint project of the Leibniz Institute for Astrophysics Potsdam (AIP) and the Institute of Physics and Astronomy of the University of Potsdam

(UP). MC acknowledges support from a Royal Society University Research Fellowship. CJW acknowledges support through the Marie Curie Career Integration Grant 303912.

Bibliography

Bacon R., et al., 2010, in Society of Photo-Optical Instrumentation Engineers (SPIE) Conference Series. p. 773508, doi:10.1117/12.856027
Beaulieu S. F., Freeman K. C., Hidalgo S. L., Norman C. A., Quinn P. J., 2010, AJ, 139, 984
Beifiori A., Maraston C., Thomas D., Johansson J., 2011, A&A, 531, A109
Bell E. F., de Jong R. S., 2001, ApJ, 550, 212
Bendo G. J., Joseph R. D., 2004, AJ, 127, 3338
Blanton M. R., Roweis S., 2007, AJ, 133, 734
Cappellari M., 2002, MNRAS, 333, 400
Cappellari M., 2008, MNRAS, 390, 71
Cappellari M., 2016, ARA&A, 54, 597
Cappellari M., Copin Y., 2003, MNRAS, 342, 345
Cappellari M., Emsellem E., 2004, PASP, 116, 138
Cappellari M., et al., 2007, MNRAS, 379, 418
Cappellari M., et al., 2011, MNRAS, 413, 813
Cappellari M., et al., 2012, Nature, 484, 485
Cappellari M., et al., 2013a, MNRAS, 432, 1709
Cappellari M., et al., 2013b, MNRAS, 432, 1862
Cappellari M., et al., 2015, ApJ, 804, L21
Cenarro A. J., Cardiel N., Gorgas J., Peletier R. F., Vazdekis A., Prada F., 2001, MNRAS, 326, 959
Coccato L., Morelli L., Corsini E. M., Buson L., Pizzella A., Vergani D., Bertola F., 2011, MNRAS, 412, L113
Conroy C., van Dokkum P. G., 2012, ApJ, 760, 71
Davidge T. J., 2008, AJ, 135, 1636
Davidge T. J., 2010, AJ, 139, 680
Davidge T. J., 2015, ApJ, 799, 97
Deharveng J.-M., Jedrzejewski R., Crane P., Disney M. J., Rocca-Volmerange B., 1997, A&A, 326, 528
Dolphin A. E., 2009, PASP, 121, 655
Doyle M. T., et al., 2005, MNRAS, 361, 34
Eggen O. J., 1971, QJRAS, 12, 305
Emsellem E., Monnet G., Bacon R., 1994, A&A, 285
Falcón-Barroso J., Sánchez-Blázquez P., Vazdekis A., Ricciardelli E., Cardiel N., Cenarro A. J., Gorgas J., Peletier R. F., 2011, A&A, 532, A95
Ferreras I., La Barbera F., de la Rosa I. G., Vazdekis A., de Carvalho R. R., Falcón-Barroso J., Ricciardelli E., 2013, MNRAS, 429, L15
Foreman-Mackey D., Hogg D. W., Lang D., Goodman J., 2013, PASP, 125, 306
Foster C., Arnold J. A., Forbes D. A., Pastorello N., Romanowsky A. J., Spitler L. R., Strader J., Brodie J. P., 2013, MNRAS, 435, 3587
Gallagher J. S., Faber S. M., Balick B., 1975, ApJ, 202, 7
Girardi L., Bressan A., Bertelli G., Chiosi C., 2000, A&AS, 141, 371
Goodman J., Weare J., 2010, Comm. App. Math and Comp. Sci., 5, 65
Holtzman J. A., Burrows C. J., Casertano S., Hester J. J., Trauger J. T., Watson A. M., Worthey G., 1995, PASP, 107, 1065
Johnston E. J., Merrifield M. R., Aragón-Salamanca A., Cappellari M., 2013, MNRAS, 428, 1296
Kamphuis P., Józsa G. I. G., Oh S.-. H., Spekkens K., Urbancic N., Serra P., Koribalski B. S., Dettmar R.-J., 2015, MNRAS, 452, 3139
Karachentsev I. D., et al., 2002, A&A, 385, 21
Karachentsev I. D., et al., 2007, AJ, 133, 504
Klypin A. A., Trujillo-Gomez S., Primack J., 2011, ApJ, 740, 102
Koopmans L. V. E., et al., 2009, ApJ, 703, L51
Kraft R. P., Nolan L. A., Ponman T. J., Jones C., Raychaudhury S., 2005, ApJ, 625, 785
Krajnović D., Cappellari M., de Zeeuw P. T., Copin Y., 2006, MNRAS, 366, 787
Krajnović D., et al., 2011, MNRAS, 414, 2923
Krist J., 1993, in Hanisch R. J., Brissenden R. J. V., Barnes J., eds, Astronomical Society of the Pacific Conference Series Vol. 52, Astronomical Data Analysis Software and Systems II. p. 536
Krist J. E., Hook R. N., Stoehr F., 2011, in Society of Photo-Optical Instrumentation Engineers (SPIE) Conference Series. p. 81270J, doi:10.1117/12.892762
Lablanche P.-Y., et al., 2012, MNRAS, 424, 1495
Li H., Li R., Mao S., Xu D., Long R. J., Emsellem E., 2016, MNRAS, 455, 3680
Makarov D., Prugniel P., Terekhova N., Courtois H., Vauglin I., 2014, A&A, 570, A13
Markwardt C. B., 2009, in Bohlender D. A., Durand D., Dowler P., eds, Astronomical Society of the Pacific Conference Series Vol. 411, Astronomical Data Analysis Software and Systems XVIII. p. 251 (arXiv:0902.2850)
McMillan R., Ciardullo R., Jacoby G. H., 1994, AJ, 108, 1610
Navarro J. F., Frenk C. S., White S. D. M., 1996, ApJ, 462, 563
Posacki S., Cappellari M., Treu T., Pellegrini S., Ciotti L., 2015, MNRAS, 446, 493
Pritchet C., 1979, ApJ, 231, 354
Ricciardelli E., Vazdekis A., Cenarro A. J., Falcón-Barroso J., 2012, MNRAS, 424, 172
Rix H.-W., Franx M., Fisher D., Illingworth G., 1992, ApJ, 400, L5
Rubin V. C., Graham J. A., Kenney J. D. P., 1992, ApJ, 394, L9

Sánchez-Blázquez P., et al., 2006, MNRAS, 371, 703
Sánchez-Janssen R., et al., 2016, ApJ, 820, 69
Sandage A., Visvanathan N., 1978, ApJ, 223, 707
Schlafly E. F., Finkbeiner D. P., 2011, ApJ, 737, 103
Scott N., et al., 2013, MNRAS, 432, 1894
Serra P., Oosterloo T., Cappellari M., den Heijer M., Józsa G. I. G., 2016, MNRAS, 460, 1382
Spiniello C., Trager S. C., Koopmans L. V. E., Chen Y. P., 2012, ApJ, 753, L32
Tonry J. L., Dressler A., Blakeslee J. P., Ajhar E. A., Fletcher A. B., Luppino G. A., Metzger M. R., Moore C. B., 2001, ApJ, 546, 681
Tortora C., La Barbera F., Napolitano N. R., 2016, MNRAS, 455, 308
Tully R. B., Libeskind N. I., Karachentsev I. D., Karachentseva V. E., Rizzi L., Shaya E. J., 2015, ApJ, 802, L25
Valdes F., Gupta R., Rose J. A., Singh H. P., Bell D. J., 2004, ApJS, 152, 251
Vazdekis A., Ricciardelli E., Cenarro A. J., Rivero-González J. G., Díaz-García L. A., Falcón-Barroso J., 2012, MNRAS, 424, 157
Weijmans A.-M., Krajnović D., van de Ven G., Oosterloo T. A., Morganti R., de Zeeuw P. T., 2008, MNRAS, 383, 1343
Weijmans A.-M., et al., 2014, MNRAS, 444, 3340
Weilbacher P. M., Streicher O., Urrutia T., Jarno A., Pécontal-Rousset A., Bacon R., Böhm P., 2012, in Society of Photo-Optical Instrumentation Engineers (SPIE) Conference Series. p. 84510B, doi:10.1117/12.925114
Wyithe J. S. B., Turner E. L., Spergel D. N., 2001, ApJ, 555, 504
van Woerden H., van Driel W., Braun R., Rots A. H., 1993, A&A, 269, 15
van den Bergh S., 1976, AJ, 81, 795
van den Bosch R. C. E., van de Ven G., 2009, MNRAS, 398, 1117

3 Surface brightness fluctuations

Surface Brightness Fluctuation (SBF) measure the pixel-to-pixel brightness variations in CCD images of galaxies. This method has been first described almost 30 years ago to measure extragalactic distances. In this chapter I give a detailed introduction to the SBF method. In observed images a number of different processes can add and remove fluctuations. Examples are the smoothing effect of the point-spread-function or the fluctuations that are caused by read-noise. I pay special attention to the approach that is used to disentangle these different contributions to the SBF and measure the pure stellar fluctuations. For this thesis the effect of the stellar population on the fluctuations is the most important aspect. I discuss the literature on that topic and motivate that SBF spectra greatly enhance the power of the SBF method for stellar population studies, especially to investigate the bright evolved stars.

3.1 Introduction

In images of an unresolved stellar population fluctuations in the brightness of neighbouring resolution elements are inevitable. Scheuer (1957) used this fact on single dish radio data to probe a population of faint, unresolved radio stars. In optical astronomy SBF were first described by Tonry & Schneider (1988) and employed to measure extragalactic distances. SBF are very sensitive to bright stars and are therefore sensitive to the stellar population. SBF have been used especially to investigate the short-lived but bright thermally pulsating Asymptotic Giant Branch (TP-AGB) evolutionary phase .

The main aim in this thesis is to further develop the optical SBF technique. So far this technique has been applied only to images. By using a number of images of the same object but in different bands, one can infer some basic information about the stellar population, like correlations in the colour SBF magnitude diagrams or radial gradients in the SBF magnitudes. This work is the first that applies the SBF method to the data of an integral field spectrograph. The data product of the used MUSE spectrograph are 3D data cubes, that provide 2D spatially resolved and spectral information. We can think of such a data cube as providing $\sim$ 3600 pseudo-images with a band width of 1.25 Å. By applying the SBF technique to every of the 3600 pseudo-images an SBF spectrum is obtained.

I start this chapter with a detailed description of the SBF method in Section 3.2. I use a simplified example to get an intuitive understanding of SBF and explain the mathematical tools needed to analyse actual observational data. I give a short summary of the methods to make SBFs a standard candle for distance measurements in Section 3.3. In Section 3.4 I describe the path that lead us to investigate SBF spectra. This includes a discussion of the influence the stellar population has on the SBFs and different approaches to enhance the SBF for investigating stellar populations.

3.2 Surface brightness fluctuations

In this section I introduce the SBF definition in Section 3.2.1 and use a simplified model to give an intuitive understanding of SBFs and how these are used to measure distances in Section 3.2.2. I go on by adding complications to the simple model and explain step by step their influence on the derivation of SBFs in Section 3.2.3 and summarise a few of the alternative

approaches to measure SBF that are discussed in the literature in Section 3.2.4. I close the section with a short summary on deriving measurement uncertainties in Section 3.2.5.

3.2.1 Definition of SBFs

Charge-Coupled Device (CCD) images of galaxies always show brightness fluctuations around an idealised smooth surface brightness profile. Tonry & Schneider (1988) explain that there are at least two reasons for these deviations: measurement noise and variations in the number of stars per pixel. The number of stars that fall on to one CCD pixel is a random number drawn from a Poisson-Statistic, with the expectation value given by the idealised smooth surface brightness profile. These variations are an intrinsic property of the galaxy (or more generally of any extended astronomical object) and should be considered as signal, not as noise. To quantify them Tonry & Schneider (1988) define a 'mean, luminosity-weighted luminosity of the stellar population' (their equation 9):

$$\bar{L} = \frac{\sum_i n_i L_i^2}{\langle L \rangle} \tag{3.1}$$

$$\langle L \rangle = \sum_i n_i L_i. \tag{3.2}$$

The index i runs over the different types of stars. The denominator in equation 3.1 is the mean luminosity of the population. The numerator $\sum_i n_i L_i^2$ is the variance of a normal distributed quantity. For sufficiently large numbers the Poisson distribution is approximated by the normal distribution. This means that equation 3.1 is the ratio of the variance and the mean – two quantities that can be measured from CCD images of galaxies.

Buzzoni (1989) develops a similar formalism to investigate the effects of a finite and discrete sampling on stellar population analysis, especially in low-mass systems like Globular Clusters (GCs). Buzzoni (1993) emphasizes the close relation between the Tonry & Schneider (1988) and the Buzzoni (1989) approach.

3.2.2 Distance dependence of SBFs

The SBF method has been invented to measure extragalactic distances. The reason why the brightness variations in CCD observations of galaxies are related to the distance can be easily understood. There are two approaches to this, the first one is the mathematical way, by simplifying the definition of SBF in equation 3.1. In the second approach I use the point of view of an observer that has a CCD observation of a galaxy.

In both approaches it is assumed that the stellar population is made of just one type of stars, meaning that $L_i \equiv L$. Inserting that into equation 3.1 we see that

$$\frac{\sum_i n_i L_i^2}{\sum_i n_i L_i} = \frac{L^2}{L} = L. \tag{3.3}$$

This shows that SBF measure the luminosity of a single star. It is important to notice that SBF have units of a luminosity.

To provide a feeling for the SBF Tonry & Schneider (1988) describe an idealised situation where a galaxy is assumed to be made of only one type of star with apparent luminosity l and a spatially constant stellar density. In a slightly modified version I will repeat their explanation here. The most important difference is that their example is based on number counts – but in unresolved populations the brightness of CCD pixels is measured. Therefore my simple model deals with luminosities instead of numbers. I assume an idealised 'observational' situation, where neither noise nor other disturbing sources nor smearing by a point spread function (PSF) is impacting the image.

Even though luminosities are observed SBFs are based on fluctuations in the number of stars per CCD pixel. The distribution of stars in such a setting is described by Poisson statistics. The most important fact that I recall about Poisson distributed quantities is that the variance is equal to the mean value:

$$\mathrm{Var}(N) = \mathrm{E}(N). \tag{3.4}$$

Poisson-statistics apply to numbers but in astronomy luminosities are observed. Assuming that all stars have the same apparent luminosity l one can relate the mean and variance in the surface brightness μ of the CCD image to the number of stars and their luminosity:

$$\mathrm{E}(\mu) = \mathrm{E}(lN) = l\mathrm{E}(N) \tag{3.5}$$

$$\begin{aligned}\mathrm{Var}(\mu) &= \mathrm{Var}(lN) = l^2\mathrm{Var}(N) \\ &= l^2\mathrm{E}(N).\end{aligned} \tag{3.6}$$

Both the mean and the variance can be measured from the data and the ratio of these two quantities is

$$\frac{\mathrm{Var}(\mu)}{\mathrm{E}(\mu)} = \frac{l^2\mathrm{E}(N)}{l\mathrm{E}(N)} = l \tag{3.7}$$

the apparent luminosity of a single star. This is an important finding, because I have made no assumptions about the actual stellar density or the luminosity of the star. This means that just from the CCD image one would be unable to say how many stars contribute to a pixel. It is the statistical approach of

the SBFs that can recover the apparent luminosity of a single star.

Since the apparent luminosity of a single star depends on the distance d and the intrinsic luminosity L

$$l = \frac{L}{4\pi d^2}, \tag{3.8}$$

it is possible to determine the distance once the intrinsic luminosity L of the star is known. This means if the galaxy is made of standard candles, the distance can be derived.

3.2.3 Measuring SBFs from CCD images

In this section I will step by step remove the simplifications I made about the galaxy in the previous section and explain how the analysis has to be modified in order to be able to recover the intrinsic fluctuations.

PSF convolution One of the assumptions was that the galaxy image is not smeared with a PSF. The PSF leads to a smoothing of the image and therefore removes some of the variance – while the mean value is unchanged. Therefore the effect of the PSF on SBF measurements needs to be corrected. In mathematical words the effect of the PSF-smoothing is a convolution of the galaxy image f with the PSF-function $f_{\rm psf}$

$$f_{\rm obs} = f * f_{\rm psf}. \tag{3.9}$$

The convolution theorem states that the convolution in the spatial domain becomes a multiplication in the Fourier (wave-number) domain. The SBF are measured from the power spectrum (the reason for that is explained below), the squared absolute value of the Fourier-transform. Then the convolution theorem reads

$$\begin{aligned} |\mathcal{F}(f_{\rm obs})|^2 &= |\mathcal{F}(f * f_{\rm psf})|^2 = |\mathcal{F}(f) \cdot \mathcal{F}(f_{\rm psf})|^2 \\ &= \underbrace{|\mathcal{F}(f)|^2}_{=\text{const}} \cdot |\mathcal{F}(f_{\rm psf})|^2. \end{aligned} \tag{3.10}$$

It turns out that $|\mathcal{F}(f)|^2$ actually measures the SBFs, if the image has been prepared in the right way (see next paragraph for the details). This means that in the Fourier domain the SBFs can be measured by just scaling the PSF power spectrum to the power spectrum of the observed image.

SBFs in Fourier domain A typical (e.g. Tonry & Schneider, 1988) preparation of SBF images is to compute a smooth mean of the surface brightness distribution (x_i, i indexing the CCD pixels), subtract that mean $\bar{x}$ and divide the residual by the square root of the subtracted smooth mean. The SBFs of such an image can be derived by just computing the sum of the squared pixel values of the renormalised image x'_i

$$\begin{aligned} \sum_i^N (x'_i)^2 &= \sum_i^N \left(\frac{x_i - \bar{x}}{\sqrt{\bar{x}}} \right)^2 \\ &= \frac{\mathrm{Var}(X)}{\mathrm{Mean}(X)}. \end{aligned} \tag{3.11}$$

This can be linked to the Fourier domain by using Parseval's theorem

$$\sum_i^N |x'_i|^2 = \frac{1}{N} \sum_j^N |\widetilde{x'_j}|^2 \tag{3.12}$$

where $\widetilde{x'}$ denotes the Fourier transform of x'. This relation shows that the mean of the power spectrum measures the SBFs of the original image. This explains why the SBFs can be obtained from the power spectrum.

Noise There is another effect of the PSF: In any observation the intrinsic SBF fluctuations are contaminated with noise fluctuations (photon shot noise, read noise, etc). These noise fluctuations are *not* convolved with the PSF. The observation should therefore be written as $f_{\rm obs} = f * f_{\rm psf} + n$. In the Fourier domain this reads

$$|\mathcal{F}(f_{\rm obs})|^2 = |\mathcal{F}(f)|^2 \cdot |\mathcal{F}(f_{\rm psf})|^2 + \underbrace{|\mathcal{F}(n)|^2}_{=\text{const}}. \tag{3.13}$$

This means while the SBF signal is multiplied with the PSF power spectrum, the measurement noise has a flat (i.e. white) power spectrum that is additive. This makes it easy to disentangle SBF and noise fluctuations in the Fourier domain. Changing the notation slightly I arrive at the fitting function that Tonry & Schneider (1988) used to measure the first SBFs:

$$P(k) = P_0 \cdot P_{\rm psf}(k) + P_1. \tag{3.14}$$

$P(k)$ is the full 2D power spectrum (Tonry & Schneider, 1988, still used the azimuthally averaged power spectrum, however, that is an unnecessary simplification). The scaling constants are: P_0 the SBFs and P_1 the noise level.

Surface brightness profile So far I have assumed that the surface brightness profile is flat, i.e. that the mean stellar density is constant. The solution for

real galaxies is to compute a smooth mean surface brightness and subtract this. Usually the residual image still has some large-scale variation that need to be corrected for (Tonry & Schneider, 1988). This is done by smoothing the image on a scale of approximately 10 times the PSF-Full Width at Half Maximum (FWHM) and subtracting the smoothed image (Tonry & Schneider, 1988).

I showed above that the standard deviation of the fluctuation is proportional to the square root of the mean value (Poisson statistics). This scaling has to be taken into account, but there are at least two different approaches in the literature: some authors (e.g. Tonry & Schneider, 1988; Pahre & Mould, 1994; Pahre et al., 1999; Dunn & Jerjen, 2006) divide the residual image by the square root of the mean surface brightness, others (e.g. Tonry et al., 1990; Jensen et al., 1998; Mei et al., 2005a) include the scaling of the fluctuations with the square root of the mean surface brightness in the expectation power spectrum (see next section for details). Both approaches give similar results, because they are equivalent. This can be shown by using Parseval's theorem (Sodemann & Thomsen, 1995).

Masking residuals In all SBF measurements there are some parts of the image that are dominated by defects and need to be masked. These defects may be foreground stars, GCs, background galaxies, residual cosmic rays, CCD defects, etc. The masking has an influence on the power spectrum, because it changes the window function. Therefore equation 3.14 has to be modified to include the effect of masking:

$$P(k) = P_0 \cdot E(k) + P_1. \tag{3.15}$$

Now the SBFs are scaled with the expectation power spectrum $E(k)$. This power spectrum is the convolution of the PSF power spectrum with the window function power spectrum. The window function is either just the mask (if the residual image has been divided by the square root of the surface brightness profile) or the product of the mask and the surface brightness profile. The derivation of the expectation power spectrum is mathematically not rigorous, but Jensen et al. (1998) justify the approach by noting: 'In computing $E(k)$ in this way, we are effectively multiplying the data by the mask prior to convolution with the PSF. The effect of this approximation on the expectation power spectrum is minimal, and $E(k)$ is very nearly the power spectrum of the PSF alone.'

Different stars The last point that has to be touched here is the restriction to only one type of stars. Equation 3.1 already shows how different types of stars can be used to compute the SBFs. In Tonry & Schneider (1988) the authors lapidary say this is valid in the limit of many stars, i.e. when Gaussian statistics apply. This is however, a very important remark and missing out this statement led to some confusion in the literature (see Raimondo et al., 2005, for a clarification).

The point is the following: in equations 3.4 to 3.6 I showed how the variance and the mean value of the luminosity are computed for a single type of stars in Poisson statistics. In equation 3.1 different populations are considered by just adding up the variances and mean values of identical stellar types. This is only valid for normal distributions and generally not for Poisson distributed quantities. This means that already in the definition of the SBF it is assumed that the Poisson distribution has converged to Gaussian. Raimondo et al. (2005) show that the assumption of Gaussian statistics is valid if 500 independent samples (roughly speaking pixels, the PSF effect has been neglected) with a stellar mass of $5 \cdot 10^3\,\mathrm{M}_\odot$ are used. Even if the mass in every pixel is an order of magnitude lower, about 2000 pixels are sufficient to fulfil the assumption of Gaussian statistics.

3.2.4 Variations to the standard SBF extraction technique

A different approach to measure SBFs is presented in Lorenz et al. (1993). The difference of this approach to the classical (Tonry & Schneider, 1988; Tonry et al., 1990) method is that the model of the light distribution is constructed via smoothing with an adaptive filter. This filter smoothes the image, without broadening sharp features (GCs or the galaxy centre Lorenz et al., 1993). Because the filter preserves the sharp features, no masking has to be applied.

Sodemann & Thomsen (1995) use a special low-pass iterative filtering technique to determine the SBF flux. This technique uses not only the mean of the data power spectrum, but also its variance. Instead of using a measured PSF-power spectrum Sodemann & Thomsen (1995) parametrize the power spectrum with an analytical function.

Yet another approach is presented in Neilsen et al. (1997). These authors compute the smooth image of the galaxy using a low-pass Fourier filter. For this they use a Butterworth filter. The filtered image is transformed back to real domain and is basically a smooth version of the galaxy with all small scale variations removed. This low-pass image is subtracted from the original image and the residual image is divided by the square root of the low-pass image. The mask is constructed by rejecting all points in the re-

maining image that deviate too much from zero to be SBF fluctuations.

Mei et al. (2005a) investigate the impact that resampling the image has on the derivation of SBFs. Resampling is an issue for the SBF technique, because it correlates the noise of adjacent pixels. Usually the data of imaging instruments do not need to be resampled during the data reduction. For the ACS Virgo cluster Survey (Côté et al., 2004) resampling is however, needed because of the significant geometrical distortion of the camera, leading to significant differences in the sky coverage of different pixels. Mei et al. (2005a) investigates different sampling kernels and their impact on SBFs, concluding that only a Lancsoz kernel allows unbiased SBF measurements.

The measurement in semi-resolved populations uses a different approach and also involves a different modelling. I discuss this in Section 3.4.2.

3.2.5 Estimating errors

The error on the SBF can be estimated from the two fitting constants P_0 and P_1. In the simplest form (e.g. Pahre et al., 1999) the signal-to-noise ratio (SNR) can be estimated by

$$\mathrm{SNR} = \frac{P_0}{P_1}. \tag{3.16}$$

Here I assume that P_0 is the SBF-flux. Being a bit more general one would have to say that P_0 is the PSF-convolved part of the fluctuations, meaning that it also includes the fluctuations contributed by unmasked point-sources (i.e. those point-sources that are too faint to be detected). At least the contribution of faint unmasked GCs to the SBF signal can be estimated from the globular-cluster luminosity function (e.g. Tonry & Schneider, 1988). See for example equation 4 in Jensen et al. (2001) for a SNR estimate considering other noise contributions.

3.3 SBF standard candles

There are basically two ways to calibrate SBFs for distance measurements. The first one is to tie the SBF distance scale to an existing distance scale and use the SBFs as secondary distance estimator, the second one relies on theoretical calibrations from stellar population modelling and makes SBFs a primary distance indicator.

3.3.1 Empirical calibration

Most of the SBF measurements that seek to measure distances use empirical zero-point calibrations, as the stellar population model uncertainties are too large for precise distances measurements. In the following I give a few examples of SBF zero-point calibrations, without aiming for completeness. In Tonry et al. (1989) the distances are obtained by fixing the distance of M32, one of the observed galaxies. Distances to the other objects are then given in multiples of the M32 distance. In a followup study Tonry et al. (1990) use the same zero point for an enlarged sample of galaxies.

In the I band SBF-survey (Tonry et al., 1997, 2001) the absolute fluctuation magnitude is shown to be a universal linear function of (V-I) colour. The zero point is obtained from Cepheid distances, comparisons with other distance estimators [planetary nebula luminosity function, Supernova (SN) Ia, SN II, Tully & Fisher (1977) relation, and $D_n - \sigma$ relation (Dressler et al., 1987)] show that the zero-point is universal.

Ajhar et al. (1997) tied the *Hubble Space Telescope* (*HST*) $F814W$ zero-point calibration to the I band SBF-survey calibration of Tonry et al. (1997).

3.3.2 Theoretical calibration

Theoretical SBFs are based on stellar population synthesis calculations. Any of these calibrations can be used to derive the absolute SBF-magnitude – colour relation. The reader is referred to Section 3.4.1 for a more detailed description of the stellar population models.

Tonry et al. (1990) present the first theoretical calibration of the SBF method. The main aim of this work was to calibrate SBFs as a function of galaxy colour for distance measurements. However, the empirical data of Tonry (1991) show that the slope of this first theoretical SBF-magnitude – colour relation has the wrong sign.

Another example of the use of SBF models to derive distances is Buzzoni (1993), computing SBF models based on the fuel consumption theorem stellar population synthesis code of Buzzoni (1989). The derived distances for the Virgo cluster and the Leo, Fornax and Eridanus groups are in good agreement with the results of Tonry (1991). More recently Cantiello et al. (2003) claimed to obtain reliable distance from theoretical SBF models.

In practice the theoretical models have never been popular to derive distances. The reason is that already small uncertainties in the stellar population models result in distance uncertainties that are larger than those that can be obtained via empirical calibrations (see previous section). However, in order to diagnose the stellar population properties, the models are essential and that is the heritage where they

have been used mostly.

The combination of theoretical and empirical SBF has worked out the stellar population influence on the SBF magnitudes. This influence has always been suspected and has played an important role in the empirical calibrations. However, usually the population effects can be calibrated out by the galaxy colour.

3.4 SBF as stellar population probes

From the definition of SBF in equation 3.1 it is obvious that SBF are sensitive to the most luminous stars in a stellar population. In intermediate-to-old stellar populations the optical and infrared SBF are therefore dominated by RGB and AGB stars (Liu et al., 2000). Therefore SBF have been suggested to be a good observational probe of evolved stars, especially TP-AGB stars. This short evolutionary phase is inherently difficult to model, but very important for the interpretation of the infrared light of stellar populations, especially at higher redshift (Maraston, 2005). I start with summarising the stellar population models that predict SBF magnitudes in Section 3.4.1. I continue with a discussion on the sampling effects and SBF magnitudes is Section 3.4.2. In Section 3.4.3 I summarise the most important observational results on the population effects and motivate why SBF spectra can improve the impact of SBF on the investigation of stellar populations. The last Section 3.4.4 introduces methods that use the diagnostic power of the SBF method for investigating stellar populations.

3.4.1 SBF models

One of the early models predicting SBF magnitudes was presented by Worthey (1993) and Worthey (1994). He already mentions that SBFs are relatively insensitive to changes in the Initial Mass Function (IMF), because only giant stars are probed. he theoretically confirms that SBFs can be calibrated against colour as has been done empirically. The competing model based on the fuel consumption theorem has been calculated by Buzzoni (1989, 1993).

It took more than half a decade before the next generation of models were presented (Liu et al., 2000, 2002; Blakeslee et al., 2001; Cantiello et al., 2003; Marín-Franch & Aparicio, 2006). These models are all motivated by the development in the stellar evolution calculations. But still these models mostly aim at older ($t \geq 3\,\mathrm{Gyr}$) stellar populations, typically found in early type galaxies. Since it is very complicated to constrain models with the observed SBFs of galaxies most authors compare their models also to GC data. Pioneering work on the modelling of SBFs from young populations is done in the work by González et al. (2004); González-Lópezlira et al. (2005) and Raimondo et al. (2005). An increasing attention has been paid to include the effect of the TP-AGB stars on SBF magnitudes (Cantiello et al., 2003; Raimondo et al., 2005; Raimondo, 2009; Lee et al., 2010; González-Lópezlira et al., 2010).

3.4.2 Sensitivity of SBF on sampling of the mass function

The brightness fluctuations that SBF measure are caused by the sampling of the stellar population in every pixel. In the classical approach it is assumed that the Poisson-Statistic can be approximated by a normal distribution, i.e. that the number of stars is large. Especially in semi-resolved studies that is not always true and needs to be taken into account.

The sampling influence has been discussed by many authors (e.g. Raimondo et al., 2005; Marín-Franch & Aparicio, 2006; Beerman et al., 2012). A very important contribution to this discussion is the rigorous differentiation between two different SBF approaches that have been used in the literature by Raimondo et al. (2005). The two different techniques are the original SBF of unresolved stellar populations (Tonry & Schneider, 1988; Tonry et al., 2001; Mei et al., 2005b; Blakeslee et al., 2009) and the slightly different approach used to diagnose semi-resolved stellar populations (Tonry & Schneider, 1988; González et al., 2004). In the later approach the numerator in equation 3.1 is obtained by summing the light of the bright resolved stars, while the denominator is obtained from the integrated light. Raimondo et al. (2005) shows that the two approaches need to be modelled in a different way, a fact that previously had been neglected. The two methods agree only in the limit when the Poisson-statistics approach Gaussian statistics, i.e. for large numbers of stars (that would be more than $2.5 \cdot 10^5\,M_\odot$). For lower mass stellar systems theoretical predictions have to use the right definitions in order to predict useful values.

3.4.3 Empirical evidence for population effects on SBFs

The fact that the stellar population has an influence on the SBF magnitudes has been always suspected. Here I summarise the most important findings.

Tonry et al. (1990) use SBF-colour – SBF-colour and SBF-colour – Mg_2 index diagrams to find that galaxies have complicated stellar populations. Tonry (1991) shows that the $\bar{m}_I$ SBF magnitude correlates

with colour, for galaxies in Eridanus, Virgo and Fornax. These galaxy colour – SBF-magnitude relations have become one of the important relations. Especially in the infrared, early models have suggested that the slope of the relation might change the sign (Worthey, 1993, 1994). Later observations unambiguously showed that the slope but not the sign changes with wavelength (Jensen et al., 1998; Liu et al., 2002; Jensen et al., 2003).

NGC 205 is the first galaxy where radial SBF variations have been detected that are well correlated with the known $(V-I)$ colour gradient (Tonry, 1991). Radial gradients in the SBF-magnitude have been observed in many other objects (Sodemann & Thomsen, 1995, 1996). Radial gradients in SBF $\bar{B}-\bar{V}$ colour have been found by Sodemann & Thomsen (1996) in M32.

Investigating 19 galactic GCs Ajhar & Tonry (1994) find that the fluctuation colour is a metallicity indicator becoming redder with increasing metallicity.

All these results have their own importance, however, non of these makes explicit use of the diagnostic power of SBF. To my knowledge the first study that uses SBF to diagnose TP-AGB evolution is Cantiello et al. (2003), finding that SBF magnitudes are sensitive to mass loss during the Asymptotic Giant Branch (AGB) phase and can be used to constrain that parameter. In a following study Raimondo et al. (2005) remarks that SBF magnitudes are especially sensitive to mass-loss in populations younger than 1 Gyr. The reason for the sensitivity of SBF on TP-AGB evolution is that changing the mass-loss rate affects the life-time and thus the total number of TP-AGB stars in a population (Raimondo, 2009). However, González-Lópezlira et al. (2010) does not find such effects in her models. The authors state that a number of effects act together to make mass loss rates degenerate in unresolved populations. An increase in the TP-AGB mass loss rate increases the intrinsic luminosity, but at the same time the life-time is shorter. An increase in the mass loss rate also leads to a higher obscuration of the star (González-Lópezlira et al., 2010). Correspondingly González-Lópezlira et al. (2010) find the strongest differences between models with and without circum-stellar dust.

This example illustrates three issues that are important for the discussion of SBF:

- The TP-AGB phase is difficult to model and there exist major uncertainties in the models. Marigo (2015) identifies three main problems in TP-AGB modelling: '1) the modelling of the TP-AGB phase is crutial for the derivation of basic galaxy properties (e.g. mass and age) up to high redshift [...]; 2) current TP-AGB calibrations based on Magellanic Cloud clusters turn out not to work properly for other external galaxies, yielding a likely TP-AGB overestimation; 3)the significance of TP-AGB contributon in galaxies, and hence their derived properties, are strongly debated, with conflicting claims in favour of either a *heavy* or *light* TP-AGB' (Marigo, 2015).

- The sensitivity of SBF to luminous stars makes these observations ideal to test TP-AGB evolution. I refer to this as the diagnostic power of SBF.

- Photometric observations (colours and SBF magnitudes) are not ideal to probe stellar evolution models. Comparisons between different theoretical predictions show that models often populate similar regions in the colour – SBF-magnitude diagrams but do still differ considerably (Liu et al., 2002; Marín-Franch & Aparicio, 2006; Lee et al., 2010; Jensen et al., 2015). This means that the fact that the models populate the same region as the data in a diagnostic diagram is necessary but not sufficient for a model to be realistic. There are two main obstacles: (i) The models predict the evolution of simple stellar populations but galaxies have complex star formation histories and multiple stellar populations. (ii) Constraining age, metallicity, distance and stellar evolution models is nearly impossible with just a few photometric data points. So either additional information is needed or these values can be constrained only for samples of similar galaxies. One complication for population studies using SBF is that these are most diagnostic in the colour – SBF-magnitude diagrams. But the SBF-magnitudes are distance dependent and thus complicate the interpretation (Cantiello et al., 2003).

A major step forward on the observational side would be to have spectral information on the SBF. The reason is that spectra are distance independent and provide much more detailed physical information than photometry. In essence SBF spectra combine the diagnostic power of the SBF method with the physical information content of spectra.

Observations of unresolved, complex stellar populations are not ideal for calibrating stellar evolution models. The reason is that the light of stars from many evolutionary phases is mixed and the stars in one evolutionary phase are very heterogenous, i.e. have different metallicities and masses. However, the SBF spectrum provides a consistency check, interme-

diate between the resolved stellar population studies and the unresolved ones. This method provides the unique chance to test Single-burst Stellar Population (SSP) models on integrated stellar populations and to compare the same models to the SBF spectra where the evolved stars are enhanced. These tests can help to validate the models for the use in situations where only integrated spectra are available.

3.4.4 Methods that use the diagnostic power of SBF

In recent years the SBF-method has been modified and developed to strengthen the usability for population investigations. In a theoretical investigation Mould (2012) shows that age and metallicity can be better constrained from giant-free spectra of unresolved simple stellar populations. Observationally the faintest pixels of the unresolved population are probably the closest realisation of a giant-free population.

A similar idea is presented in Beerman et al. (2012). They consider semi-resolved stellar populations and the uncertainties introduced by a stochastic sampling of the giant branch. They conclude that removing the bright resolved stars can limit the uncertainties. Beerman et al. (2012) show that the cut-off magnitude should be slightly brighter than the main-sequence turn-off. Both fainter and brighter cut-off magnitudes increase the uncertainties.

Another concept is the so called 'fluctuation spectroscopy' introduced in van Dokkum & Conroy (2014). In principle the fluctuation spectroscopy compares the difference spectrum of individual spatial pixels for a given total flux difference, i.e. how does the spectrum of a faint spatial pixel compare to the mean spectrum of the galaxy. In practice van Dokkum & Conroy (2014) use only 6 narrow band filters calibrated to measure the index strength of three spectral features.

A technique that aims at gaining information about long-period variable stars (mostly post-AGB stars) is the 'pixel-shimmer' method of Conroy et al. (2015). Here the authors obtain pixel light curves of unresolved populations. A fraction of the pixels actually does show temporal brightness variations that are caused by the long period variable stars. This method is challenging, because long time monitoring combined with high spatial resolution and precise spatial positioning are needed. On the other hand the models can reveal the age of the population and the long-period variable star fraction.

Another approach to investigate semi-resolved stellar populations are the pixel colour – magnitude diagrams presented by Conroy & van Dokkum (2016). In contrast to plotting individual stellar colours and magnitudes the colours and magnitudes of CCD pixels, containing 1 to 10^4 stars on average are plotted. The authors show that with this approach they are able to recover the star formation history of mock observations.

3.5 Summary

In this chapter I motivate the development of spectroscopic SBF. For this motivation I start with the very basics, introducing the classical SBF method, as used to measure distances. I explain in detail the procedures that are used to disentangle the SBF from measurement noise and the PSF smoothing.

For distance measurements the population effects are calibrated via SBF-magnitude colour relations, however, in the mean time the SBF method has developed into a stellar population probe. Especially the sensitivity to the luminous stars has been suggested to be helpful to constrain TP-AGB models.

The limiting factor in these investigations is the information content of a few magnitudes and SBF-magnitudes. This is the reason for developing the method of spectroscopic SBFs, that combine the diagnostic power of the SBF method with the physical information content of spectra.

Bibliography

Ajhar E. A., Tonry J. L., 1994, ApJ, 429, 557
Ajhar E. A., Lauer T. R., Tonry J. L., Blakeslee J. P., Dressler A., Holtzman J. A., Postman M., 1997, AJ, 114, 626
Beerman L. C., et al., 2012, ApJ, 760, 104
Blakeslee J. P., Vazdekis A., Ajhar E. A., 2001, MNRAS, 320, 193
Blakeslee J. P., et al., 2009, ApJ, 694, 556
Buzzoni A., 1989, ApJS, 71, 817
Buzzoni A., 1993, A&A, 275, 433
Cantiello M., Raimondo G., Brocato E., Capaccioli M., 2003, AJ, 125, 2783
Conroy C., van Dokkum P. G., 2016, ApJ, 827, 9
Conroy C., van Dokkum P. G., Choi J., 2015, Nature, 527, 488
Côté P., et al., 2004, ApJS, 153, 223
Dressler A., Lynden-Bell D., Burstein D., Davies R. L., Faber S. M., Terlevich R., Wegner G., 1987, ApJ, 313, 42
Dunn L. P., Jerjen H., 2006, AJ, 132, 1384
González-López lira R. A., Albarrán M. Y., Mouhcine M., Liu M. C., Bruzual-A. G., de Batz B., 2005, MNRAS, 363, 1279

González-Lópezlira R. A., Bruzual-A. G., Charlot S., Ballesteros-Paredes J., Loinard L., 2010, MNRAS, 403, 1213
González R. A., Liu M. C., Bruzual A. G., 2004, ApJ, 611, 270
Jensen J. B., Tonry J. L., Luppino G. A., 1998, ApJ, 505, 111
Jensen J. B., Tonry J. L., Thompson R. I., Ajhar E. A., Lauer T. R., Rieke M. J., Postman M., Liu M. C., 2001, ApJ, 550, 503
Jensen J. B., Tonry J. L., Barris B. J., Thompson R. I., Liu M. C., Rieke M. J., Ajhar E. A., Blakeslee J. P., 2003, ApJ, 583, 712
Jensen J. B., Blakeslee J. P., Gibson Z., Lee H.-c., Cantiello M., Raimondo G., Boyer N., Cho H., 2015, ApJ, 808, 91
Lee H.-c., Worthey G., Blakeslee J. P., 2010, ApJ, 710, 421
Liu M. C., Charlot S., Graham J. R., 2000, ApJ, 543, 644
Liu M. C., Graham J. R., Charlot S., 2002, ApJ, 564, 216
Lorenz H., Bohm P., Capaccioli M., Richter G. M., Longo G., 1993, A&A, 277, L15
Maraston C., 2005, MNRAS, 362, 799
Marigo P., 2015, in Kerschbaum F., Wing R. F., Hron J., eds, Astronomical Society of the Pacific Conference Series Vol. 497, Why Galaxies Care about AGB Stars III: A Closer Look in Space and Time. p. 229 (arXiv:1411.3126)
Marín-Franch A., Aparicio A., 2006, A&A, 450, 979
Mei S., et al., 2005a, ApJS, 156, 113
Mei S., et al., 2005b, ApJ, 625, 121
Mould J., 2012, ApJ, 755, L14
Neilsen Jr. E. H., Tsvetanov Z. I., Ford H. C., 1997, ApJ, 483, 745
Pahre M. A., Mould J. R., 1994, ApJ, 433, 567
Pahre M. A., et al., 1999, ApJ, 515, 79
Raimondo G., 2009, ApJ, 700, 1247
Raimondo G., Brocato E., Cantiello M., Capaccioli M., 2005, AJ, 130, 2625
Scheuer P. A. G., 1957, Proceedings of the Cambridge Philosophical Society, 53, 764
Sodemann M., Thomsen B., 1995, AJ, 110, 179
Sodemann M., Thomsen B., 1996, AJ, 111, 208
Tonry J. L., 1991, ApJ, 373, L1
Tonry J., Schneider D. P., 1988, AJ, 96, 807
Tonry J. L., Ajhar E. A., Luppino G. A., 1989, ApJ, 346, L57
Tonry J. L., Ajhar E. A., Luppino G. A., 1990, AJ, 100, 1416
Tonry J. L., Blakeslee J. P., Ajhar E. A., Dressler A., 1997, ApJ, 475, 399
Tonry J. L., Dressler A., Blakeslee J. P., Ajhar E. A., Fletcher A. B., Luppino G. A., Metzger M. R., Moore C. B., 2001, ApJ, 546, 681
Tully R. B., Fisher J. R., 1977, A&A, 54, 661
Worthey G., 1993, ApJ, 409, 530
Worthey G., 1994, ApJS, 95, 107
van Dokkum P. G., Conroy C., 2014, ApJ, 797, 56

Stellar population synthesis with SPAA 4

In this chapter the stellar population synthesis code SPAA is introduced. The unique feature of SPAA is the computation of theoretical Surface Brightness Fluctuation (SBF) spectra, that are needed for comparison with the observed SBF spectrum. Apart from that SPAA is implemented in a way that enables flexible change of input data, like the isochrone tables or stellar spectral libraries. Currently I use PARSEC isochrones and three different stellar libraries: the theoretical PHOENX 2013 and the Coelho 2014 libraries, and the observational MILES library. I test a linear interpolation routine that is much faster than other interpolation algorithms.

4.1 Introduction

Our understanding of galaxies and other unresolved stellar populations is strongly influenced by our ability to interpret the light of these systems. In galaxies the stars and the nebular gas emission are contributing the light, if galaxies with an active nucleus are omitted. Circumstellar and interstellar dust absorb light and re-emit the light in the infrared. This process, known also as reddening, reshapes the spectral energy distribution of galaxies. Here the discussion is restricted to the stellar part of the light.

The first steps in understanding the light of galaxies have been done in the sixties of the last century. In order to reproduce the observed galaxy magnitudes and colours linear combinations of stellar magnitudes were computed (Wood, 1966; McClure & van den Bergh, 1968; Spinrad & Taylor, 1971). This is in principle an easy task, but actually there are a number of constraints that need to be taken into account: the weights need to be non-negative and the Herzsprung–Russel diagram needs to have a reasonable shape. Therefore this was mostly a trial-and-error method, based on the experience and skills of the person and not mathematically rigorous. Faber (1972) introduced a fitting code that implemented both: a classical minimization under given constrains. This approach had the potential to make the stellar combination reproducible.

In the same year Tinsley (1972) introduced evolutionary population synthesis. In this approach the author describes the evolution of a galaxy in a closed box: stars form from collapsing gas clouds and return metal enriched material to the interstellar medium during their lifetime. The initial mass distribution of stars and the star formation history are parametrized with analytical functions. This is a major step forward, because it starts describing the physical processes that drive the galactic evolution and hence these models might be tested against the observations. The major problems in the seventies were the limited (i.e. very sparse mass sampling) and inhomogeneous stellar tracks (i.e. collected from many different sources). Since the evolution of the bright, evolved stars is fast, a sparse sampling in mass leads to unphysical jumps in magnitudes and colours.

These difficulties with describing the fast giant evolution were the reason for inventing the fuel consumption theorem. The fuel consumption theorem states that the bolometric luminosity of any post main-sequence phase is directly proportional to the fuel burned during this stage (Renzini, 1981). So in practice the fuel consumption theorem just changes the integrating variable from the mass to the fuel for the post main-sequence stars. This approach has some advantages over the evolutionary population synthesis, as it can provide the luminosity contribution of any post main sequence phase. The main disadvantage is that it predicts bolometric luminosity

that is not observable.

The next major step that advanced the evolutionary population synthesis is the invention of isochrone synthesis by Charlot & Bruzual (1991). Isochrones had been used to interpret photometric observations before Charlot & Bruzual (1991) used this concept to obtain a finer mass sampling and hence reduce the unphysical fluctuations in population models.

Not only the modelling approach changed over time, also the data and analysis strategies have changed. In the beginning the broad-band colours of galaxies have been used to investigate the stellar populations. Later the invention of the Lick/IDS index system (Burstein et al., 1984; Worthey et al., 1994) made this analysis very popular. With the increasing amount of medium and even high-resolution spectra the technique of full-spectrum fitting became the most prominent and widely used method to analyse the light of galaxies (e.g. Cappellari & Emsellem, 2004; Cid Fernandes et al., 2005; Ocvirk et al., 2006; Koleva et al., 2009).

This chapter is structured as follows: In Section 4.2 I motivate the development of a new stellar population synthesis code. In Section 4.3 the input data are described. This is the Initial Mass Function (IMF), the isochrone tables and the stellar spectral library. Section 4.4 describes the SPAA code. The use of the Hess–diagram in the synthesis is described. The linear interpolation routine that was implemented is tested and the synthesis of SBF spectra is discussed.

4.2 Motivation for computing a new stellar population library

In the literature many stellar population libraries are described (e.g. Leitherer et al., 1999; Bruzual & Charlot, 2003; Le Borgne et al., 2004; Maraston, 2005; Coelho et al., 2007; Conroy et al., 2009; Mollá et al., 2009; Vazdekis et al., 2010, 2012). So the question is why is another library needed? There are two reasons for us to add another stellar population library. The immediate objective for this project is that I need SBF model spectra and – since this is a new analysis technique – no such models are available in the literature.

On the longer run this new project aims at replacing the isochrones in the stellar population synthesis by directly deriving the Hess–diagram from the stellar evolutionary tracks. Isochrones are produced by interpolating stellar evolutionary tracks, meaning these are secondary products themselves. Often the isochrones need to be interpolated, because their metallicities or ages do not fit the needs for the population synthesis. By directly computing the Hess–diagram from the evolutionary tracks at least one interpolation would be omitted.

For the current project I still use isochrones to populate the Hess diagram, but implement the synthesis via a Hess–diagram. So the current code is effectively an isochrone synthesis code, but offers the possibility to easily exchange the module that computes the Hess–diagram in the future. This new code is called Stellar Populations for All Applications (SPAA).

4.3 Input data

Two types of input data are needed: a set of isochrones and a stellar population library. I made an effort to write the code in such a way that the input data can be changed easily and the user is not bound to a specific choice. Additionally a prescription for the IMF is needed. In the following I will describe which data and parametrizations are used.

4.3.1 Initial mass function parametrizations

SPAA currently implements two IMF functions: a Chabrier like, with the normalisation given in table 1 of Chabrier (2003):

$$\xi(\log m) = \begin{cases} 0.158 \cdot \exp\left[-\frac{(\log m - \log 0.079)^2}{2 \cdot 0.69^2}\right] & \text{if } \log m \leq 0 \\ 0.0443 \cdot m^{-1.3} & \text{else.} \end{cases} \tag{4.1}$$

Here m is the mass of the star in units of solar masses. The second IMF form is given in eq. 18 of Chabrier (2003):

$$\xi(\log\, m) = 0.086 \exp\left[-\frac{(\log\, m - \log\, 0.22)^2}{2 \cdot 0.57^2}\right]. \tag{4.2}$$

Only the former one is useful for spectral synthesis purposes, the later one includes the effects of blends due to unresolved binary stars. This form is useful for resolved stellar population studies, where star counts matter.

4.3.2 Stellar isochrones

Currently I am using the most recent PARSEC isochrones (Bressan et al., 2012), because of their special emphasis on thermally pulsating Asymptotic Giant Branch (TP-AGB) evolution (Marigo et al., 2013). The details of the isochrones are described in Section 5.5.1.

4.3.3 Stellar spectral libraries

An important ingredient in stellar population synthesis are stellar spectral libraries. Two different types of libraries are widely used: empirical libraries (observed stellar spectra, e.g. Gorgas et al., 1993; Worthey et al., 1994; Cenarro et al., 2001; Prugniel & Soubiran, 2001; Le Borgne et al., 2003; Valdes et al., 2004; Sánchez-Blázquez et al., 2006; Chen et al., 2014) and theoretical libraries (e.g. Husser et al., 2013; Coelho, 2014). Both types come with advantages and disadvantages.

The main advantage of theoretical libraries is that the input parameters, like effective temperature ($T_{\rm eff}$), surface gravity and chemical composition are controlled. This enables the computation of large homogeneously sampled libraries. This is especially important to compute the models of rare giant stars or stars with chemical compositions that are different from the pattern observed in the solar neighbourhood (i.e. solar scaled). Theoretical spectra are computed at very high resolutions and are broadened according to the science requirements. The spectra can be computed for large continuous wavelength ranges and are noise free.

The disadvantages of theoretical spectra are that their accuracy depends on our knowledge of the physical processes at work and the precision and completeness of input data. One of the longstanding problems with theoretical models of stellar atmospheres is that there are high-resolution models that are good for comparison with observed spectra but not good in predicting photometric properties (Coelho, 2014). This is caused by the atomic transition tables used as input. These are split into lists with observed lines (i.e. the atomic levels have been measured in laboratories) and predicted lines (i.e. the energy levels are only predicted by quantum mechanics). Due to the inaccuracies in the predicted line tables these are missing in high-resolution spectra calculations. But these weak absorption lines do add some important line blanketing to the spectra that becomes noticeable when computing broad-band magnitudes. For the computation of photometric properties a second low-resolution spectrum, the Spectral Energy Distribution (SED), is computed that uses less accurate but more complete line lists including predicted lines.

The main advantage of empirical libraries is that these are based on observed spectra of stars. Therefore any further analysis based on such a library is independent from our knowledge of stellar atmospheres.

The main disadvantage of empirical libraries is that they mostly sample stars in the solar vicinity and therefore are biased towards solar scaled abundances. It is also difficult to sufficiently sample all regions of the Hertzsprung–Russel diagram, especially the regions where stars are evolving fast (high mass stars or the TP-AGB phase of intermediate to low mass stars). This is problematic when stellar population spectra are computed from these libraries, because then spectra need to be interpolated over sparsely populated areas or even worse need to be extrapolated. The last point to be mentioned is that empirical libraries are always noisy and have a finite resolution that is given by the instrumental line spread function of the spectrograph used for the observations.

Theoretical stellar spectral libraries in SPAA

Coelho 2014 The theoretical stellar library by Coelho (2014) has been computed with the specific aim to be used for stellar population synthesis models. The library consists of opacity distribution functions, model atmospheres, statistical samples of surface fluxes (SED models) and high-resolution spectra (Coelho, 2014). As discussed in the previous section SED-models are computed using both the observed line transitions and the less certain predicted ones. This is essential to compute broad-band magnitudes from the theoretical models. High-resolution spectra (i.e. those models used for comparison with observed spectra) include only the observed line list. The pseudo-continuum of the high-resolution spectra is corrected for the effects of line blanketing from predicted lines. This is done by computing differential correction functions between the high-resolution and the SED model (for details see Coelho, 2014). Therefore the Coelho (2014) high-resolution models can be used to compute accurate broad-band fluxes.

The other focus of this library is to investigate the effect of α-element abundances. The library provides spectra with four different solar scaled compositions: $[\mathrm{Fe/H}] = (-1.0, -0.5, 0.0, +0.2)$. For every composition two α-enhanced mixtures are computed: one at fixed total metallicity and one at fixed iron abundance.

The spectra are computed for values in the range $3000 \leq T_{\rm eff} \leq 25\,000\,\mathrm{K}$ and $-0.5 \leq \log g \leq 5.5$. The coverage of the $T_{\rm eff}$ – $\log g$ plane is however, not complete as it follows the locus of stellar isochrones. The spectra cover the wavelength range from 2500 to 9000 Å at a Gaussian Full Width at Half Maximum (FWHM) resolution of $R = 20\,000$.

PHOENIX 2013 The PHOENIX 2013 library (Husser et al., 2013) is a new extensive grid of stellar spectra and model atmospheres computed with the PHOENIX code version 16 (Hauschildt & Baron, 1999). This version implements up-to-date equation of states and atomic and molecular line lists

with the benefit of predicting especially cool stars much better than other libraries (Husser et al., 2013). The PHOENIX models are computed in spherical geometry and assume local thermodynamic equilibrium. The current library covers $2300 \leq T_{\rm eff} \leq 12\,000\,{\rm K}$, $0.0 \leq \log g \leq 6.0$, $-4.0 \leq [{\rm Fe/H}] \leq +1.0$. The library also provides α-element enhanced and depleted spectra for a (increasing) subset of spectra, with values in the range $-0.2 \leq [\alpha/{\rm Fe}] \leq 1.2$. In the PHOENIX library α-element changes are computed at fixed iron abundance, meaning that the total metallicity changes when α-elements are changed.

The covered wavelength range is $500 \leq \lambda \leq 55\,000$ Å. For the current work I use a version of the library that covers only the wavelength range from $3000 \leq \lambda \leq 10\,000$ Å with a FWHM resolution of 1 Å sampled with 0.1 Å.

Empirical stellar spectral library in SPAA

MILES I decided to use the observational library MILES (Sánchez-Blázquez et al., 2006). The basic properties of the library will be described in Section 5.5.2

In addition to the discussion in that section I add here the calibration of the spectra. The fluxes of the observed stars do depend not only on the emitted flux but also on the distance. I found that the stars in the MILES library are not corrected for this effect. I decided to follow the flux calibration Prugniel & Soubiran (2001) use for the ELODIE library: they scale the flux of the stars to 1 at 5500 Å. I do the same for all MILES stars. Then I multiply with the flux of a theoretical PHOENIX spectrum of similar surface gravity, effective temperature and chemical composition at the same wavelength. In this way both theoretical and observational spectra have the same flux units and can be treated in the same way by SPAA. The resulting spectra for stars with various temperatures at fixed metallicity and surface gravity is shown in Fig. 4.1.

4.4 The SPAA code

SPAA is currently a set of functions or modules that can handle different parts of the stellar population synthesis. The main aim is to provide a flexible code that can handle different tasks. One of these standard tasks is to compute libraries of Single-burst Stellar Population (SSP)-model spectra. For this special task I have written a wrapper that handles this. This code will be explained in the following.

4.4.1 The parameter file

The SPAA code is controlled with a parameter file, where all of the inputs and outputs are specified, as well as many internal parameter are set. This is very important for a program that aims to be flexible with many input data. The parameter file is structured in lines, with every line providing one parameter. Comment lines start with the number-sign (#). Every line is structured into four parts, separated by white spaces:

1. parameter name: this is a string of any length
2. parameter value(s): the value of a parameter may be a string or a number or an array. array elements must be separated by a comma (,), no white spaces!
3. identifier: the identifier is used in the code to format the parameter in the right shape, it should give the type of the parameter (i=integer, f=float, ia=integer array, fa=float array, b=boolean s=string). Any parameter with an identifier that is not implemented ends up to be a string. So not implemented identifiers will not crash the code while reading the parameter file.
4. comments: the last part starts with an exclamation mark (!). Every thing that follows is treated as a single string (including white spaces) and is thought as an explanation of the parameter.

The parameter file is read into a dictionary that is (almost) identical to the parameter dictionary class used in PYPARADISE (for a description of this full spectrum fitting code see Section 5.6.1). Therefore any new keyword can be invented and written to the parameter file without disturbing the code.

4.4.2 Reading the isochrone

Isochrones are one of the important input data for stellar population synthesis models. However, there is no general format in which isochrones are distributed. The naming scheme of isochrone files and also the information provided in the table itself is very diverse. This means that for any new isochrone to be used with SPAA, the naming scheme has to be implemented – or the file-names have to follow the naming scheme of an implemented isochrone. Currently the isochrone names are generated from three parameters: metallicity, α-enrichment and age.

The isochrone is stored in a dictionary, because isochrone tables provide usually very different information and there is no standardised format. Storing the

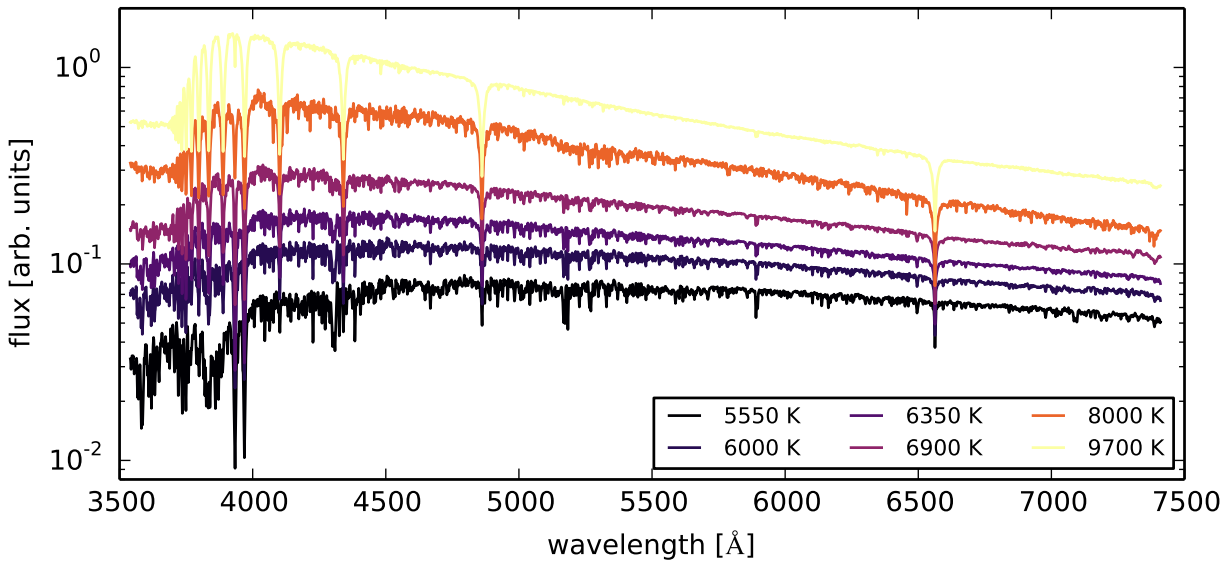

Figure 4.1: Miles spectra after normalising the fluxes with the PHOENIX library (see text), for a range of effective temperatures and around log $g = 4.0$ for stars with roughly solar abundance.

input in a dictionary structure enables to read all information from the isochrone-file – without needing a code already expecting exactly that information. This makes it easy to switch to different isochrones. To read an isochrone table a description file is needed that connects the keyword that is used in the code with the column where the corresponding information is found in the isochrone table. This would be for example

```
1 InitMass
3 logL
4 logTeff
```

if the initial mass values are written in the second (counting starts with 0!), logarithmic luminosities in the fourth and logarithmic temperatures in the fifth column. The reading routine will use only those columns that are written in the description file.

There are a few values that are required to run the code, these are: `InitMass, logTeff, logg` and `logL`. The last one could be made optional, when the stellar radius would be computed via equation 4.8 instead of equation 4.7. If the parameter key word `cut_evol_phases` is set 'True', i.e. some specified evolutionary phases should be removed from the isochrone, then the code also expects the isochrone to have the evolutionary phase identifier `evolStage`. There are also a number of optional isochrone information that are used, if provided: `ActMass, Uband, Bband, Vband, Rband, Iband, Jband, Hband, Kband, Mbol`.

After reading the isochrone all stellar models with mass outside the mass range specified in the parameter file are removed from the isochrone.

SPAA offers the possibility to remove specified stellar phases. This feature might be useful to explore the effects of different evolutionary phases on SSP spectra. It can be used if the evolutionary phase is tagged in the isochrone table and the `cut_evol_phases` keyword is true. Then the evolutionary phases specified under the `cut_evol_phases_id` keyword are removed.

4.4.3 Generate the Hess–diagram

The Hess–diagram is a two dimensional grid in the $T_{\rm eff}$ – log g space. The extension and the sampling of the grid are set in the parameter file. While the lower limits of the Hess-grid are taken from the parameter file, the upper cut-off might be slightly changed (always to larger values) to make the grid range an integer multiplicative of the sampling size.

If the isochrone points do extend outside of the specified grid a warning is printed, but these points will not be considered in the further computations. All other isochrone points are rounded to the next Hess-grid centre value in effective temperature and surface gravity.

The next step is to compute the IMF-weights. I therefore define the boundaries of initial mass inter-

vals

$$m_i^{\rm low} = \frac{m_{i-1}+m_i}{2} \text{ for } 1 < i \leq N \tag{4.3}$$

$$m_i^{\rm up} = \frac{m_i+m_{i+1}}{2} \text{ for } 0 < i \leq N-1 \tag{4.4}$$

$$m_N^{\rm up} = m_N + \frac{m_N - m_{N-1}}{2}. \tag{4.5}$$

The lower mass boundary $m_0^{\rm low}$ is always fixed to the mass interval given in the parameter file. This is important to ensure a meaningful IMF normalisation. The IMF weights $\rho(m_i)$ for every stellar model are obtained by integrating the IMF between the lower and upper bounds.

$$\rho(m_i) = \int_{m_i^{\rm low}}^{m_i^{\rm up}} \xi(\log m)\, {\rm d}\log m. \tag{4.6}$$

IMF weights should be (by definition) positive. If for some reason negative IMF values occur, a warning is printed.

The Hess–diagram is the IMF weight as function of $T_{\rm eff}$ and $\log g$ and thus it is a number-density diagram. For the stellar synthesis a modified version of this diagram is needed: The reason is that theoretical libraries provide the stellar fluxes in units of flux per unit area of stellar surface. This means a diagram is needed that also gives the product of stellar surface and IMF weights as function of $T_{\rm eff}$ and $\log g$ – I call this a flux density diagram.

For the flux density diagram the stellar radius R_* is computed following

$$R_* = R_\odot \sqrt{\frac{L_*}{L_\odot}\left(\frac{T_\odot}{T_{\rm eff}}\right)^4} \tag{4.7}$$

with L_* being the stellar luminosity. Alternatively the following formula has been used and shown to give similar results

$$R_* = \frac{GM_*}{g_*} \tag{4.8}$$

with G the constant of gravity, the stellar mass M_* and the stellar surface gravity g_*. Now the luminosity density diagram is

$$\rho_L(m_i) = 4\pi R_i^2 \rho(m_i). \tag{4.9}$$

For the computation of SBF spectra a third Hess-like density diagram is needed. The reason is that in the numerator of the SBFs (see equation 3.1) the squared fluxes are summed. I therefore define the fluctuation density as

$$\rho_f(m_i) = \left(4\pi R_i^2\right)^2 \rho(m_i). \tag{4.10}$$

The three density diagrams (i.e. number, luminosity and fluctuation) are compared in Fig. 4.2. This comparison shows nicely that the stellar mass is dominated by low-mass main-sequence stars. Many evolutionary phases contribute to the integrated light (I emphasize that the effect of surface temperature is not included in the flux density, meaning that hotter stars will effectively contribute more). The variance spectrum is dominated by the most evolved stars.

I also compute the initial mass of the population by integrating the IMF from 0.1 to 100 $M_\odot$.

In case the isochrone provides magnitudes $\mathbf{m}_x$ (with x being U, B, V, R, I, J, H, K, bol) also the luminosity in different filters is computed via

$$\mathbf{m}_x = -2.5 \log \left[\sum_i \rho(m_i) \cdot 10^{\mathbf{m}_{i,x}/2.5} \right]. \tag{4.11}$$

4.4.4 Spectrum interpolation

For the population synthesis a spectrum at every grid-point of the Hess–diagram (or at least at every grid-point with non-zero IMF-weight) is needed. Since no spectral library is sampled that dense I need to interpolate the existing spectra at the grid points.

I decided to interpolate only in the two-dimensional plane of $T_{\rm eff}$ and $\log g$. The interpolation starts with reading the positions of the stellar spectra in the library at a given metallicity and computing the convex hull surrounding these points. The next step is to setup the Hess-grid, i.e. the grid for the interpolated library. From this grid I remove all points that fall outside the convex hull. The remaining points are those where the spectra are interpolated. However, I limit the maximum separation between input spectra to $\Delta T_{\rm eff} \leq 1000\,{\rm K}$ and $\Delta \log g \leq 0.5$.

I use two interpolation methods: a fast but non-standard interpolation scheme that is a local linear interpolation and a standard piecewise cubic interpolation.

Cubic interpolation

I use the SCIPY.INTERPOLATE.GRIDDATA routine for the cubic interpolation. The 2D interpolation algorithm I use determines a 'piecewise cubic, continuously differentiable (C1), and approximately curvature-minimizing polynomial surface'[1]. This interpolation interpolates in the 3D space of (f_λ, $T_{\rm eff}$ and $\log g$). Therefore the interpolation has to loop

[1] see the SCIPY.INTERPOLATE.GRIDDATA documentation at http://docs.scipy.org/doc/scipy-0.14.0/reference/generated/scipy.interpolate.griddata.html

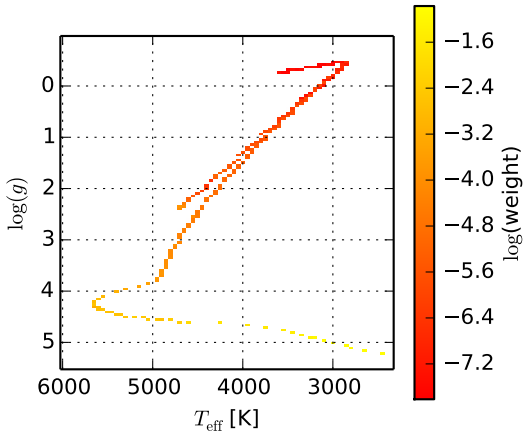

(a) Number density

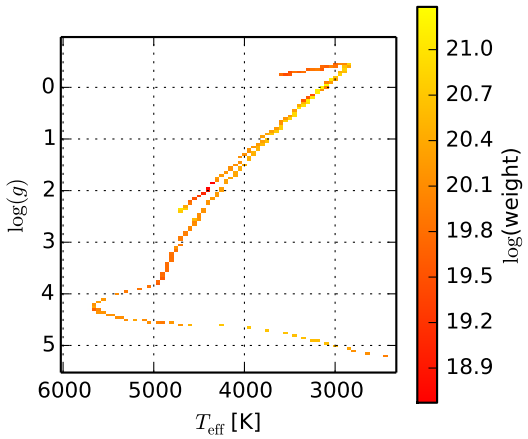

(b) Luminosity density

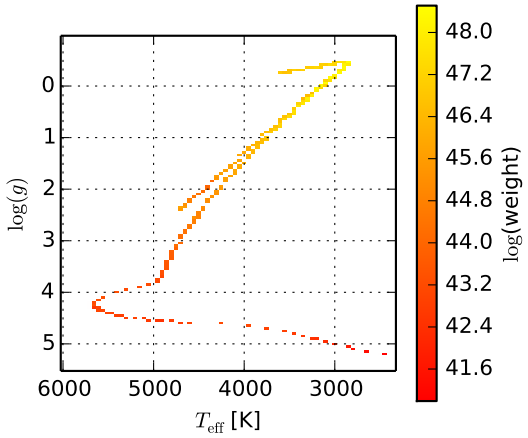

(c) Fluctuation density

Figure 4.2: The plot shoes the three types of Hess–diagrams computed by SPAA for a 13 Gyr old solar metallicity population. The original Hess–diagram is the number density plot, the flux density is the product of IMF weight and stellar surface and the fluctuation density is the product of IMF weight and squared stellar surface.

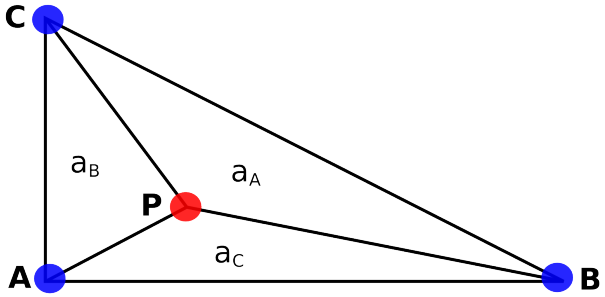

Figure 4.3: This sketch explains our linear interpolation scheme in equation 4.12. The areas a_A, a_B and a_C are used to weight the spectra at positions A, B and C to interpolate the spectrum at position P.

over every spectral point and that makes this approach rather slow, especially with high resolution theoretical libraries.

Linear interpolation

The linear interpolation that I use was developed to provide a fast interpolator[2]. For any given point P in the $T_{\rm eff}$ and log g plane this method searches for the three nearest neighbours in the input library grid that form a triangle. The positions of these three points are named A, B and C, see Fig. 4.3 for a sketch of the situation. The spectrum at point P is interpolated as a weighted linear combination of the spectra at the points A, B, C. The weight for point A is the fraction the small triangle P, B, C contributes to the area of the triangle A, B, C (see Fig. 4.3).

$$F_P = a_A F_A + a_B F_B + a_C F_C \tag{4.12}$$

$$1 = a_A + a_B + a_C \tag{4.13}$$

The advantage of this method is that it is fast, because the weights are *not* wavelength dependent.

Testing the linear interpolation

Since the linear interpolation method is not standard I tested the performance of this method. The best test would be to remove one spectrum from the input library and interpolate that spectrum. Unfortunately on rectangular grids this forces this linear interpolation method to fall back into a 1D interpolation along either the $T_{\rm eff}$ or the log g axis. I therefore compare the results obtained with the cubic GRIDDATA interpolation routine and the linear interpolation. In Fig. 4.4 I plot the standard deviation of the difference (in percent) between the cubic and linear

[2] I acknowledge Oliver Rieger for implementing the linear interpolation method that is used in SPAA.

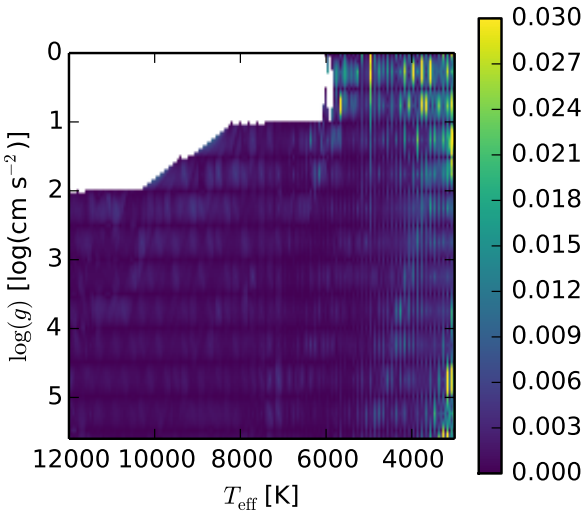

Figure 4.4: The plot shows the standard deviation between PHOENIX spectra interpolated with a standard piece-wise cubic spline interpolation and our custom made linear interpolation. The maximum RMS is of the order of 3%, for most spectra it is well below the 1% level. The cut-off pattern in the upper left corner is caused by enforcing limits on the maximum separation of input spectra, see text for details.

interpolated PHOENIX spectra. This plot shows that the maximum Root Mean Square (RMS) is of the order of 3%, while for most spectra the RMS is well below 1%. From this excise I conclude that the linear interpolation scheme is well suited for interpolating the spectra.

4.4.5 Spectral synthesis

Synthesising SSP spectra can be expressed as an integral over the stellar mass:

$$S(\lambda,t,Z)=\int_{m_l}^{m_u} f(\lambda,m,t,Z)\xi(m)\mathrm{d}m. \tag{4.14}$$

Where $\xi(m)$ is the IMF and $f(\lambda,m,t,Z)$ is the spectrum of a star with initial mass m, at an age t and with a heavy element fraction of Z. Usually an isochrone is used to translate the initial mass and the age to the atmospheric parameters effective temperature and surface gravity that describe a stellar spectrum.

In SPAA the basic property of any population is the Hess–diagram and therefore the spectral synthesis is a summation of the Hess–diagram

$$S(\lambda,t,Z)=\sum_{T_{\rm eff},\log\ g} f(\lambda,T_{\rm eff},\log\ g,Z)\rho_L(T_{\rm eff},\log\ g,t,Z). \tag{4.15}$$

If the stellar library provides spectra that give the total irradiated power per unit wavelength, one has to replace ρ_L by ρ_m.

For the synthesis of SBF spectra I compute the variance spectrum

$$S_{\rm var}(\lambda,t,Z)= \sum_{T_{\rm eff},\log\ g} f^2(\lambda,T_{\rm eff},\log\ g,Z)\rho_f(T_{\rm eff},\log\ g,t,Z). \tag{4.16}$$

The SBF spectrum can then be computed as the ratio of the variance and the integrated spectrum

$$S_{\rm SBF}=\frac{S_{\rm var}}{S}. \tag{4.17}$$

The advantage of this approach is that complex stellar populations can be easily computed via

$$S_{\rm SBF}=\frac{\sum_i w_i S_{\rm var}}{\sum_i w_i S}, \tag{4.18}$$

where i indicates the SSP and w_i is the weight of the ith population. In this way I preserve the strength that any 'complex' stellar population can be composed as a linear combination of the SSP templates also for the SBF spectra of 'complex' populations.

4.4.6 Connection between model and data SBF spectra

The computation of the model SBF spectra in the above paragraphs follows the definition of the SBF in equation 3.1. I have split the summation in the numerator and the denominator in two separate sums: first the summation over all stars of a simple stellar population and a second sum over all populations.

In the observations I basically measure the ratio of variance and mean value from the power spectrum (see equations 3.11 and 3.12). The connection between the measurement and the definition of the SBF in equation 3.1 is explained in section 3.2.3 in the paragraph on different stars.

The important assumption in equations 4.16 and 4.18 is that Gaussian statistics apply, because I sum the variances and mean values of different populations and stellar types. Therefore these models are only valid if also for the observed stellar population Gaussian statistics are a valid description. Raimondo et al. (2005) show that this means that the stellar mass has to be larger than $2.5\cdot10^5\,\mathrm{M}_\odot$.

4.5 Summary

For this thesis SBF model spectra are essential for the interpretation of the observational data. Because

none of the existing stellar population synthesis models predicts these spectra I present in this section the new stellar population synthesis code SPAA that computes for the first time SBF model spectra.

Currently SPAA implements the widely used isochrone synthesis approach to compute integrated and SBF spectra for SSP populations. Due to their detailed TP-AGB prescription I decided to use PARSEC isochrones. Three different stellar spectral libraries are currently used: the theoretical libraries PHOENIX and the one by Coelho (2014) and the observed MILES spectral library.

For the interpolation of the spectra a new non-standard, but fast linear interpolation routine is used. I validate this new interpolation routine by demonstrating that the interpolated spectra are very similar to the results of more standard cubic spline interpolation routines.

In this section I provide many technical details on the SPAA code and especially the wrapper that is used to compute SSP spectra. One point to be emphasized is that in future versions of SPAA the Hess-diagram will be directly computed from the stellar evolutionary tracks, istead of using the isochrone tables.

Bibliography

Bressan A., Marigo P., Girardi L., Salasnich B., Dal Cero C., Rubele S., Nanni A., 2012, MNRAS, 427, 127

Bruzual G., Charlot S., 2003, MNRAS, 344, 1000

Burstein D., Faber S. M., Gaskell C. M., Krumm N., 1984, ApJ, 287, 586

Cappellari M., Emsellem E., 2004, PASP, 116, 138

Cenarro A. J., Cardiel N., Gorgas J., Peletier R. F., Vazdekis A., Prada F., 2001, MNRAS, 326, 959

Chabrier G., 2003, PASP, 115, 763

Charlot S., Bruzual A. G., 1991, ApJ, 367, 126

Chen Y.-P., Trager S. C., Peletier R. F., Lançon A., Vazdekis A., Prugniel P., Silva D. R., Gonneau A., 2014, A&A, 565, A117

Cid Fernandes R., Mateus A., Sodré L., Stasińska G., Gomes J. M., 2005, MNRAS, 358, 363

Coelho P. R. T., 2014, MNRAS, 440, 1027

Coelho P., Bruzual G., Charlot S., Weiss A., Barbuy B., Ferguson J. W., 2007, MNRAS, 382, 498

Conroy C., Gunn J. E., White M., 2009, ApJ, 699, 486

Faber S. M., 1972, A&A, 20, 361

Gorgas J., Faber S. M., Burstein D., Gonzalez J. J., Courteau S., Prosser C., 1993, ApJS, 86, 153

Hauschildt P. H., Baron E., 1999, Journal of Computational and Applied Mathematics, 109, 41

Husser T.-O., Wende-von Berg S., Dreizler S., Homeier D., Reiners A., Barman T., Hauschildt P. H., 2013, A&A, 553, A6

Koleva M., Prugniel P., Bouchard A., Wu Y., 2009, A&A, 501, 1269

Le Borgne J.-F., et al., 2003, A&A, 402, 433

Le Borgne D., Rocca-Volmerange B., Prugniel P., Lançon A., Fioc M., Soubiran C., 2004, A&A, 425, 881

Leitherer C., et al., 1999, ApJS, 123, 3

Maraston C., 2005, MNRAS, 362, 799

Marigo P., Bressan A., Nanni A., Girardi L., Pumo M. L., 2013, MNRAS, 434, 488

McClure R. D., van den Bergh S., 1968, AJ, 73, 313

Mollá M., García-Vargas M. L., Bressan A., 2009, MNRAS, 398, 451

Ocvirk P., Pichon C., Lançon A., Thiébaut E., 2006, MNRAS, 365, 74

Prugniel P., Soubiran C., 2001, A&A, 369, 1048

Raimondo G., Brocato E., Cantiello M., Capaccioli M., 2005, AJ, 130, 2625

Renzini A., 1981, Annales de Physique, 6, 87

Sánchez-Blázquez P., et al., 2006, MNRAS, 371, 703

Spinrad H., Taylor B. J., 1971, ApJS, 22, 445

Tinsley B. M., 1972, A&A, 20, 383

Valdes F., Gupta R., Rose J. A., Singh H. P., Bell D. J., 2004, ApJS, 152, 251

Vazdekis A., Sánchez-Blázquez P., Falcón-Barroso J., Cenarro A. J., Beasley M. A., Cardiel N., Gorgas J., Peletier R. F., 2010, MNRAS, 404, 1639

Vazdekis A., Ricciardelli E., Cenarro A. J., Rivero-González J. G., Díaz-García L. A., Falcón-Barroso J., 2012, MNRAS, 424, 157

Wood D. B., 1966, ApJ, 145, 36

Worthey G., Faber S. M., Gonzalez J. J., Burstein D., 1994, ApJS, 94, 687

Surface brightness fluctuation spectrum: a new probe of evolved stars in unresolved stellar populations*

5

The Surface Brightness Fluctuation (SBF) method is by definition sensitive to the most luminous stars in a stellar population and provides therefore the diagnostic power to investigate the evolved luminous AGB stars in unresolved stellar populations. We apply the SBF technique to integral field spectroscopy data from the MUSE instrument and obtain the first SBF spectrum of a galaxy. SBF spectra combine the sensitivity of the SBF method to the luminous stars with the physical information content of spectra and thus reveal the full potential for stellar population studies. We show that the SBF spectrum of the S0 galaxy NGC 5102 is dominated by giant stars of spectral type M (RGB and AGB stars), carbon stars contribute at a much weaker level. We build the first stellar population synthesis tool that predicts SBF spectra. This isochrone integration code uses two different stellar spectral libraries as input: the observed MILES stars and the fully theoretical spectra by Coelho. The integrated spectra from the two libraries agree reasonably. The SBF spectrum models reveal that the models based on observed spectra predict weaker molecular features that are in better agreement with the NGC 5102 SBF spectrum. We use the integrated spectrum to derive the star formation history of NGC 5102. The additional constraints obtained by forcing the models to recover also the SBF spectrum do not further tighten the constraints on the derived star formation history. This result is confirmed by modelling mock spectra with different star formation histories.

5.1 Introduction

Surface Brightness Fluctuations (SBF) measure the spatial brightness variations in an image of a stellar population that are introduced by the random sampling of the stellar population in every resolution element (pixel). This technique had been used for some time in radio astronomy (Scheuer, 1957), before almost 30 years ago Tonry & Schneider (1988) introduced SBFs in optical astronomy as a technique to measure (extragalactic) distances. SBFs have become one of the common tools to measure extragalactic distances.

By definition SBFs are sensitive to the most luminous stars in a stellar population. In turn this means that SBFs depend on the stellar population properties. Some of the early findings are that SBF magnitudes correlate with colour (e.g. Tonry, 1991; Sodemann & Thomsen, 1996) and that SBF magnitudes and colours are metallicity depended (Ajhar & Tonry, 1994). The theoretical models indicate that SBFs are sensitive to the giant branch temperature, but are not good in differentiating age and metallicity effects (Worthey, 1993). SBFs amplify the signal of the most luminous stars in a stellar population. Which evolutionary phase this is depends on the photometric band and the age of the population (Liu et al., 2000; Cantiello et al., 2003). In intermediate-to-old stellar populations the SBF signal in the optical and especially in the infrared is contributed by red giant branch (RGB) and asymptotic giant branch (AGB) stars. Because SBFs enhance the signal from these evolved stars, this method is especially beneficial for the study of RGB and AGB stars in unresolved stellar populations.

The AGB evolution is among the least well understood evolutionary phases (for a review see Herwig, 2005). This evolutionary phase is short, but complex.

* A version of this chapter will be submitted to *Monthly Notices of the Royal Astronomical Society*. The preliminary list of co-authors includes Paula R. T. Coelho, Gabriella Raimondo, Martin M. Roth and C. Jakob Walcher

The AGB stars have two burning shells, encounter a number of He-flashes (called thermal pulses) and subsequent deepening of the convective zone, so called third dredge-ups. These dredge-ups bring nuclear processed material to the surface and change the chemical abundance of the atmosphere.

Even though TP-AGB stars are short-lived, they are extremely luminous and therefore are important for the interpretation of the light of unresolved stellar populations (Maraston, 2005; Conroy et al., 2009). The uncertainties in the TP-AGB models lead stellar population to work better in the optical than in the infrared wavelength range or vice versa (Eminian et al., 2008; Zibetti et al., 2009; Taylor et al., 2011).

It is the combination of the sensitivity of SBFs to the AGB stars and the uncertainty in the models that lead Cantiello et al. (2003) to use SBFs to constrain AGB mass loss. Raimondo et al. (2005) and Raimondo (2009) confirm that SBF magnitudes are sensitive to the AGB mass loss rates. In contrast to these findings González-Lópezlira et al. (2010) find only a week or absent dependency of SBF magnitudes on the AGB mass loss.

Constraining the different models with SBF magnitudes is difficult because these are distance dependent, and as discussed also depend on age and metallicity. So these many different effects are at least partly degenerate and complicate a firm conclusion. Especially when the models are compared to galaxy data, we are also faced with the problem that models assume SSPs, while galaxies certainly have composite stellar populations. The fact that the models and data cover the same space in a diagnostic diagram (i.e. colour vs SBF-magnitude or colour vs SBF colour) is the minimum requirement the models have to fulfil. Liu et al. (2002) show partly contradicting models that still span the range of observed galaxy properties. The model uncertainties in the TP-AGB modelling of infrared SBFs are highlighted in Jensen et al. (2015). Even though the differences between models are sometimes drastic, it is hard to say which model performs better on the basis of just a few SBF magnitudes and colours.

In this paper we will introduce SBF spectra, i.e. spectrally resolve the SBFs. By applying the SBF technique to several thousand pseudo-images of integral field spectrograph data we obtain SBFs with a spectral sampling of 1.25 Å. The only instrument that is currently providing integral field spectroscopy (IFS) over a sufficiently large field of view, with a sufficient spatial sampling, and a full octave in the spectral domain is the new second generation instrument MUSE (Bacon et al., 2010) mounted at ESOs Very Large Telescope.

The SBF spectra combine the sensitivity to the evolved RGB and AGB stars with the physical information content of spectra. So we expect that only SBF *spectra* can reveal the full power of SBFs for population studies and will be much better suited to constrain models than photometry.

Our approach of resolving the SBFs spectrally should not be confused with the 'fluctuation spectroscopy' of van Dokkum & Conroy (2014). Firstly because these authors use only six narrow-band images centred on selected spectral features, whereas we have access to the full spectral range from ~ 4800 to about ~ 9300 Å at a resolving power of 1770 to 3500. Secondly, 'fluctuation spectroscopy' is methodically different from our approach: SBFs are referred to by the authors as the relative brightness of a pixel to a smooth light-profile, whereas our SBF is based on the original Tonry & Schneider (1988) definition. Furthermore, they use their narrow-band images to create index images and compare the variation of the index value as function of the pixel brightness relative to a smooth mean value.

In Section 5.2 we describe the target selection and summarise the properties of NGC 5102. We briefly summarise the observation and data reduction. We explain why the radial velocity needs to be corrected and how we did that. The extraction of the SBF spectrum from the IFS datacube is detailed in Section 5.3. A comparison of the SBF spectrum to stellar spectra of spectral types M and C is presented in Section 5.4. In order to compare the SBF spectrum to stellar population models, we setup a population synthesis model that predicts SBF spectra (Section 5.5) and use these models in Section 5.6 to fit the star formation history and compare with the SBF spectrum.

5.2 Data

5.2.1 Observations and data reduction

For this pilot study on the feasibility of measuring SBF from MUSE data we selected the galaxy that is best suited for SBF measurements. We therefore selected the galaxy with the brightest apparent SBF magnitude from the SBF I-band survey (Tonry et al., 1997, 2001) that is visible from Paranal Observatory in June ($200° \leq \mathrm{RA} \leq 340°$ and $\mathrm{Dec} \leq -10°$).

NGC 5102 was observed during the MUSE science verification run [programme 60.A-9308(A), PI: Mitzkus] in the night from 2014 June 23 to 24. MUSE is a panoramic integral field spectrograph, with a 60×60 arcsec field of view and 0.2 arcsec spatial sampling (Bacon et al., 2010). The wavelength cov-

erage is nominally from 4800 to 9300 Å. We obtained four object exposures of 960 s each, rotated by 90° to distribute the residuals of the image slicer system homogeneously over the field of view. The data reduction was carried out with the dedicated MUSE data reduction software (Weilbacher et al., 2012) version 1.0.1, following the standard procedure. The final product is a cube with mean SNR per volume-pixel of 4.5. The data-set and the reduction have been described in detail in Mitzkus et al. (2017).

5.2.2 Correcting the radial velocity shifts

With the SBFs we measure the intrinsic brightness differences to the mean values of CCD pixels that are caused by the spatial distribution of stars. So far the SBF method has been applied only to imaging data, sometimes in multiple bands. However, the spectral resolution of a MUSE observation is orders of magnitudes better than for imaging data. This in turn has implications for the data reduction and the SBF analysis. To measure a meaningful SBF spectrum it is required that one wavelength slice of the data-cube represents one rest-frame wavelength. A spatially varying redshift (as is typically caused by the rotation of a galaxy) will smear out one rest-frame wavelength, i.e. one spectral feature like an absorption line, over several wavelength layers of the data-cube. Therefore we have to correct the spectra for the line-of-sight velocity v.

The velocity field of NGC 5102 has been measured from the same data-set in Mitzkus et al. (2017, see fig. 2) and is used here to shift all spectra to the same rest-frame velocity. The line-of-sight velocity has been measured on spatially binned spectra using the Voronoi tessellation algorithm of Cappellari & Copin (2003) to ensure a sufficient SNR for an unbiased measurement of the kinematics.

The fact that SBF measure the intrinsic brightness differences between neighbouring pixels means for the data reduction that interpolations should be kept at the absolute necessary minimum (Mei et al., 2005). Any interpolation will correlate the noise of neighbouring pixels and impact the SBF measurement. Fortunately the MUSE data reduction software interpolates the data only once, i.e. in the final step where the data cube is produced. All previous data reduction steps are applied to the data in a pix-table format, where for every CCD-pixel the flux, CCD position, wavelength and spatial position are stored.

Correcting the radial velocity shifts in the final data-cube would result in a second interpolation. In order to avoid this second interpolation we correct the radial velocities in the pixtables, after combining the fully reduced individual exposures, but before producing the final data cube. For every CCD pixel we compute the corrected wavelength from the velocity of the spatially nearest Voronoi bin (in RA and Dec of the centre position of the Voronoi bin). The final data cube is computed from this radial velocity corrected pixtable using the standard MUSE data reduction tool.

5.2.3 NGC 5102

The Centaurus group galaxy NGC 5102 is a low luminosity S0 galaxy (Karachentsev et al., 2002). The surface brightness fluctuation distance to NGC 5102 was measured to 4.0 ± 0.2 Mpc by Tonry et al. (2001). Other distance estimators find slightly smaller distances: The Planetary Nebula Luminosity Function distance was measured as 3.1 Mpc (McMillan et al., 1994), the tip of the red-giant branch measurements scatter between 3.2 Mpc (Davidge, 2008) and 3.74 Mpc (Tully et al., 2015). The stellar mass of NGC 5102 has been estimated to be $(5.6 \pm 0.8) \times 10^9\,\mathrm{M}_\odot$ (Beaulieu et al., 2010), broadly consistent with the estimate of Davidge (2015).

While the photometric appearance of NGC 5102 is typical for S0 galaxies (Pritchet, 1979; Davidge, 2015), this galaxy has a number of peculiarities. Freeman was the first one to notice the unusually blue colour of the nucleus (Eggen, 1971) that later was attributed to the presence of a star cluster with an age of $\sim 10^8$ yr (e.g. Gallagher et al., 1975; van den Bergh, 1976; Pritchet, 1979). Also the $3.3 \times 10^8\,\mathrm{M}_\odot$ H I reservoir (Gallagher et al., 1975) is relatively large for S0 galaxies. The H I is distributed in a ring like structure with a radius of 2.2 kpc and a prominent central depression (van Woerden et al., 1993). van den Bergh (1976) detected an Hα emission structure that was later also seen in [O III] (McMillan et al., 1994). The ring-like structure and the fact that the emission line ratios indicate shock ionization leads to the conclusion that this is a supershell (McMillan et al., 1994). Based on the velocity of the gas and the size these authors estimate an age of about 10^7 years for the supershell.

The stellar population in NGC 5102 has been investigated in many ways. In the centre Beaulieu et al. (2010) find a constant star formation rate over the last 0.2 Gyr and a burst about 20 Myr ago, in agreement with Deharveng et al. (1997). This burst is in remarkable agreement with the estimated age of the supershell. Davidge (2015) derives a luminosity weighted SSP age for the nucleus of $1^{+0.2}_{-0.1}$ Gyr and for the bulge of $2^{+0.5}_{-0.2}$ Gyr. The first IFU based, i.e. spatially resolved full spectrum fitting investigation of the stellar population confirmed the age and re-

vealed a metallicity gradient, with an about 0.8 Gyr old solar metallicity population in the centre and an about 2 Gyr old stellar population in the outer parts with sub-solar metallicity of $[M/H] \sim -0.5$ (Mitzkus et al., 2017).

5.3 Extracting the SBF spectrum

In this section we first describe the standard SBF method that is used for analysing imaging data. We then describe the modifications that are necessary to apply the method to IFU data.

5.3.1 Measuring SBF from images

The standard approach of measuring SBFs from images (Tonry & Schneider, 1988) starts with constructing a spatial mask of all extended and point sources and bad pixels. It is assumed that the sky flux has been accurately subtracted from the image during the data reduction. A smooth surface brightness model m is constructed. By subtracting the model from the data the brightness fluctuations become visible, but are still proportional to the square root of the surface brightness model. We call this the preliminary residual image

$$r' = d - m. \tag{5.1}$$

The spatial mask is complemented by masking all disturbing objects that show up on the preliminary residual image. To remove remaining large scale structures the preliminary residual is smoothed on a scale of ~ 10 times the PSF FWHM, providing the r'_{smooth} image that preserves only the large scale structure. We also renormalise the image to bring the fluctuations to a common level (e.g. Tonry & Schneider, 1988; Pahre & Mould, 1994; Pahre et al., 1999; Dunn & Jerjen, 2006)

$$r = \frac{r' - r'_{\mathrm{smooth}}}{\sqrt{m}}. \tag{5.2}$$

The masked residual image is then Fourier-transformed and the power-spectrum $P(k)$ is computed. The smoothing impacts the power spectrum at the lowest wave-numbers (Tonry & Schneider, 1988), therefore these need to be masked in the later analysis.

The data power spectrum is fitted with

$$P(k) = P_0 \cdot E(k) + P_1. \tag{5.3}$$

Where P_0 is the SBF flux and P_1 measures the photon shot noise. $E(k)$ is the expectation power-spectrum. The expectation power-spectrum is obtained by convolving the mask power-spectrum with the PSF power-spectrum (this is mathematically not rigorous but a very practical approximation, see remark by Jensen et al., 1998).

5.3.2 Adapting the procedure to measure the SBF spectrum from MUSE data

To extract the SBF spectrum from a MUSE data-cube requires some adjustments of the traditional approach presented in the previous section. This starts with creating a white light image from the data cube. In principle one could just collapse the data-cube along the dispersion dimension to create the white light image, but this would neglect the influence of nebular and sky emission lines. Since NGC 5102 has some prominent nebular emission lines that might disturb a fit of the stellar surface brightness we mask (in the spectral dimension) those lines. Conservatively we also mask the brightest 100 sky lines, because at these wavelength the residuals of the image slicer system are most prominent. The white light image is obtained by averaging all unmasked wavelength layers of the data-cube and shown in Fig. 5.1(a).

We also cut the data-cube in all three dimensions (lower and upper wavelength cut and at all four edges in the spatial plane) to remove incompletely covered regions.

We compute the smooth surface brightness profile from the white light image with the ELLIPSE task in the STSDAS IRAF package. ELLIPSE fits a number of elliptical isophotes to the input image, without further parametrizing the global shape of the surface brightness. We use the BMODEL task to create the surface brightness model (SB model) from the set of ellipses fitted with ELLIPSE. The SB model is shown in Fig. 5.1(b).

We derive the spatial mask by subtracting the SB model from the white light image, as shown in Fig. 5.1(c). In this image there are a number of point-like objects that need to be masked. More importantly in the centre of the galaxy there are strong residuals. This is probably due to dust absorption that also ruined the SB fit in the centre. We mask those regions completely and are left with the pure fluctuation image shown in Fig. 5.1(d).

The next step is the renormalisation of every monochromatic layer of the data-cube (see equations 5.1 and 5.2). For this we scale the SB model to the monochromatic layer under consideration. The scaling constant is the ratio of the mean object flux and

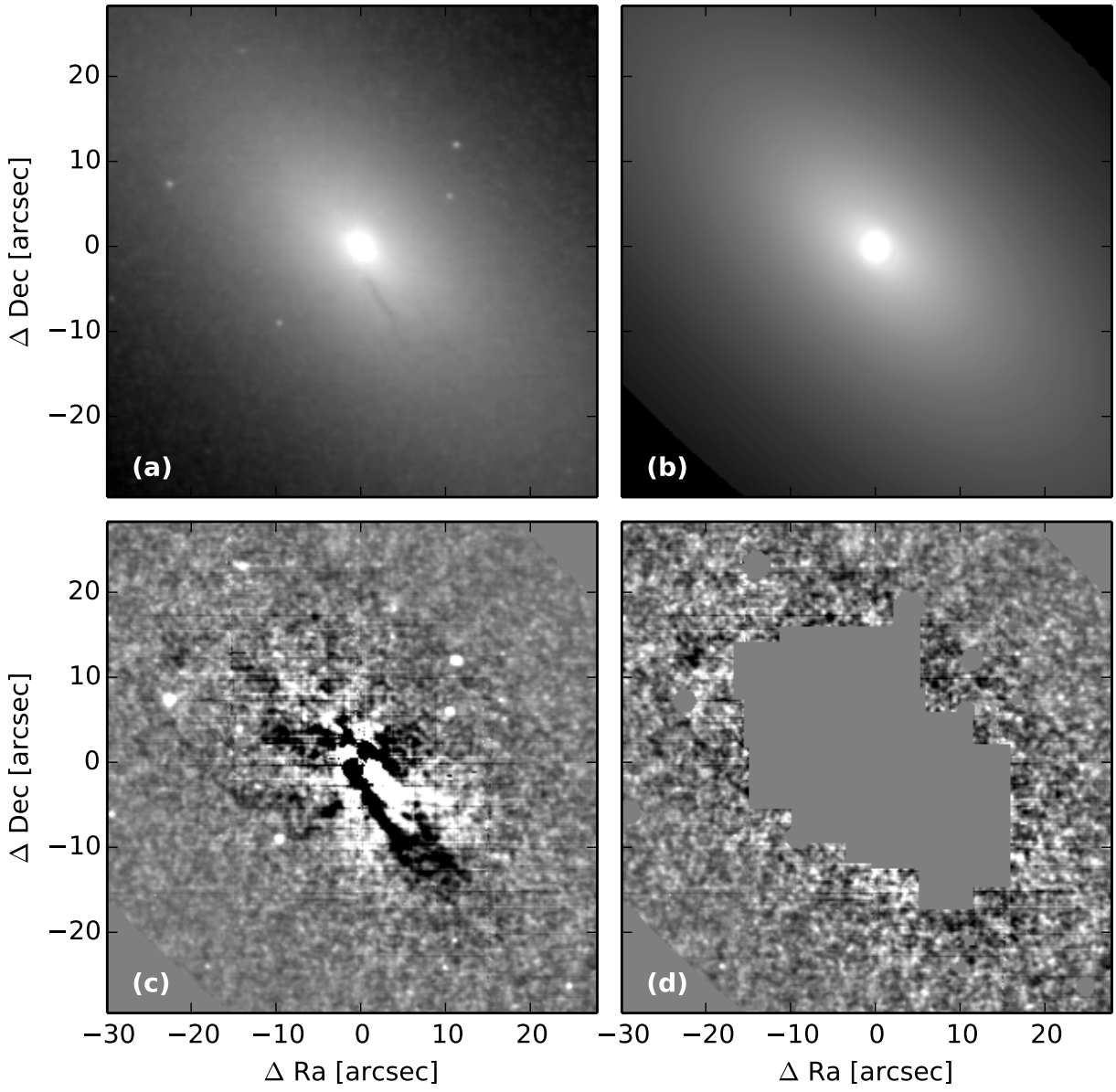

Figure 5.1: (a) The white light image of NGC 5102, obtained by collapsing the MUSE data cube along the spectral dimension. Spectral layers that are affected by nebular or sky emission have been masked out. (b) The surface brightness model of NGC 5102. (c) Residuals after subtracting the SB model. (d) The residuals have been masked with the spatial mask.

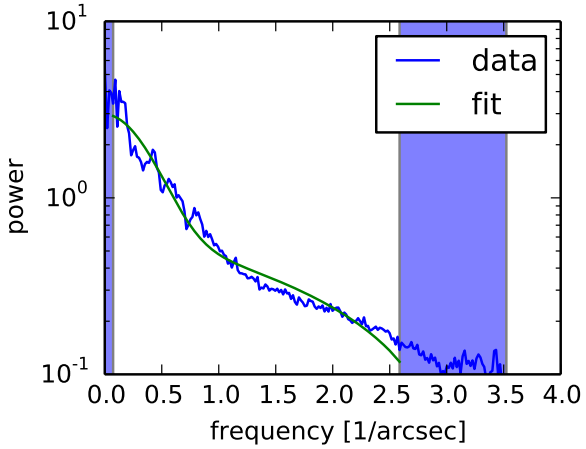

Figure 5.2: The data power spectrum at 6500 Å (blue) with the corresponding fit (green). Shaded regions have been masked for the fitting.

the mean SB model flux. We subtract the scaled SB model from the data to obtain the preliminary residual image (equation 5.1). This image is smoothed with a 2D gaussian with a full width at half maximum (FWHM) of 40 pixels. We remove remaining large scale galaxy features by subtracting the smoothed version from the preliminary residual image. Finally, we divide by the square root of the scaled SB model to obtain the residual image (equation 5.2).

The data power spectrum is computed from the residual image by multiplying this image with a window-function and Fourier-transforming the product. The window-function we use is the product of the spatial mask and a Hanning-function. The 1D Hanning-function is defined as

$$H(n) = 0.5 - 0.5\cos(\frac{2\pi n}{M-1}) \qquad 0 \leq n \leq M-1 \tag{5.4}$$

and the 2D version is obtained via the outer product of two Hanning-functions. The power spectrum is the square of the absolute value of the Fourier-transform.

Since the resampling of the MUSE data introduces non-negligible correlations of the white noise we have to modify equation 5.3 to fit the data power spectrum. We find that

$$P(k) = P_0 \cdot E(k) + P_1 + P_2 \cdot k \tag{5.5}$$

reproduces the observed power spectrum well[1]. The correlated noise term in the equation affects also the absolute value of the measured SBF (Mei et al., 2005). Since the properties of the resampling kernel are wavelength independent, the bias in the SBF spectrum is just a global offset, that does not affect our conclusions. Before fitting the power spectrum we apply a frequency mask: we cut the smallest frequencies $f < 0.07\,\mathrm{arcsec}^{-1}$, because these are affected by the smoothing of the residuals and the highest wave numbers $f > 2.6\,\mathrm{arcsec}^{-1}$, because those contain only information about the noise properties and would bias the fit in an unwanted way. We show an example fit of the power spectrum in Fig. 5.2.

In order to compute the expectation power spectrum we first compute the PSF and window-function power spectra. The PSF power spectrum is computed by multiplying the PSF image with the Hanning-function prior to the Fourier-transformation. The window function power spectrum is obtained by Fourier-transforming the product of the spatial mask and the Hanning-function. The expectation power spectrum $E(k)$ is the convolution of the PSF and the window function power spectrum.

As mentioned at the beginning of the section we apply the described steps to every monochromatic layer of a MUSE data cube. This gives about 3600 SBF values at different wavelengths - an SBF spectrum.

We estimate the SNR of the SBF spectrum at each spectral pixel from the ratio (Pahre et al., 1999; Jensen et al., 2001)

$$\mathrm{SNR}(\lambda) = \frac{P_0(\lambda)}{P_1(\lambda)}. \tag{5.6}$$

The integrated and the SBF spectrum of NGC 5102 are shown in Fig. 5.3. The integrated spectrum is the sum of all spectra at unmasked positions in Fig. 5.1(d). We had to mask a number of wavelength in the SBF spectrum for two reasons: The gas emission in the galaxy dominates over the stellar surface brightness fluctuations. The second major contamination are skylines. At the positions of sky lines the residual data-cube is dominated by the pattern of the image-slicer system MUSE is using. The overall shape of the SBF spectrum is very different from the integrated: while the integrated spectrum decreases with increasing wavelength, the SBF spectrum increases with increasing wavelength. The blue part of the SBF spectrum is flat and given the large noise featureless. The strongest features that we see are molecular bands in the wavelength region between 7000 and 8000 Å.

[1] In order to test the resampling influence on the noise properties we filled a pixtable with white noise and used the MUSE data reduction software to compute the final data cube. From these tests we see that the originally white noise (with a constant power spectrum) becomes a power spectrum that linearly decreases with the wavenumber k.

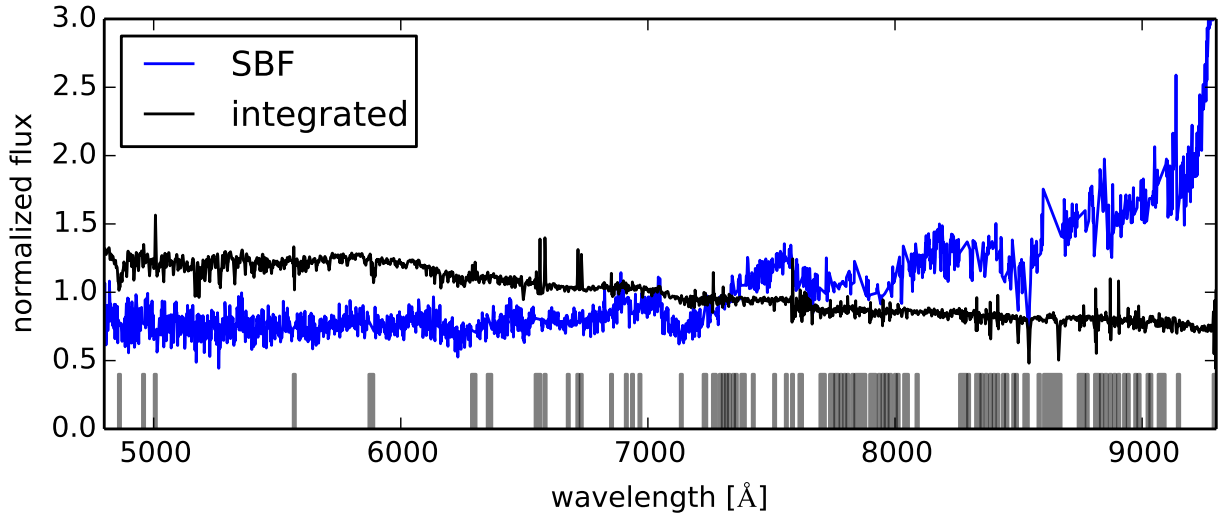

Figure 5.3: The integrated (black) and the SBF spectrum (blue) of NGC 5102 obtained from the MUSE observations. The grey marked regions have been masked in the SBF spectrum, as these wavelength are contaminated by either gas emission in NGC 5102 or by atmospheric emission lines. No masking has been applied to the integrated spectrum.

5.4 Comparison of the SBF spectrum with stellar spectra

SBF are dominated by the most luminous stars in a population. In intermediate-to-old stellar populations these are RGB and (TP-) AGB stars. To a first degree approximation TP-AGB spectra come in two flavours: stars with oxygen rich (spectral type M) and stars with carbon rich atmospheres (spectral type C). Main-sequence stars have mostly oxygen rich atmospheres with C/O < 1.0, however, also carbon rich dwarfs are found and their frequency in the solar neighbourhood is under discussion (e.g. Fortney, 2012). During the third dredge-up C/O increases, transforming initial M type stars into C-type stars. The change from an oxygen to a carbon rich atmosphere is not only in the spectrum relevant, it also impacts the opacity and other fundamental parameters of the stars (e.g. Marigo et al., 2013). The frequency of M and C stars is metallicity dependent (Battinelli & Demers, 2005; Cioni, 2009), a dependency on age is discussed (Feast et al., 2010; Kacharov et al., 2012).

Given this importance of the C to M star ratio it is very interesting to investigated whether the SBF spectrum exhibits C star features and how dominant these are. We therefore use the DR1 spectra from the X-shooter spectral library (XSL; Chen et al., 2014) for a comparison. Most of these spectra cover the wavelength range from 3000 to 10 200 Å, much more than the MUSE wavelength range. The wavelength coverage is an important advantage of XSL over other libraries, because it allows to compare the spectra over the full MUSE wavelength range. The XSL resolution of 10 000 is much higher than needed, we therefore broaden the XSL spectra with a Gaussian line-spread function of 2.5 Å to bring them to the MUSE resolution.

From the XSL DR1 database[2] we obtained the spectra of 'M-type' and 'carbon-related' stars. For most of the M-type stars we obtain the metallicity, effective temperature and surface gravity values from Chen (2013).

For the comparison of the SBF spectrum with the XSL spectra we mask sky and emission lines (as in Fig. 5.3) and missing parts of the XSL spectra. To avoid numerical issues we normalise the SBF and the stellar spectra by their mean values. We compute a reduced χ^2 via:

$$\chi^2_{\mathrm{red}} = \frac{1}{\mathrm{DOF}} \sum_i \frac{\left[F^{\mathrm{SBF}}_{\mathrm{data}}(\lambda_i) - P(n, x_i, \boldsymbol{a}) \cdot F_{\mathrm{XSL}}(\lambda_i)\right]^2}{\varepsilon^2(\lambda_i)}. \tag{5.7}$$

Where the degrees of freedom (DOF) are the number of unmasked spectral pixels, x_i maps the wavelength array into the interval $[-1, 1]$ and $P(n, x, \boldsymbol{a})$ is the sum of the first $n + 1$ Legendre polynomials $P_i(x)$

$$P(n, x, \boldsymbol{a}) = \sum_{i=0}^{n} a_i P_i(x), \qquad x \in [-1, 1]. \tag{5.8}$$

[2] Available from http://xsl.u-strasbg.fr/

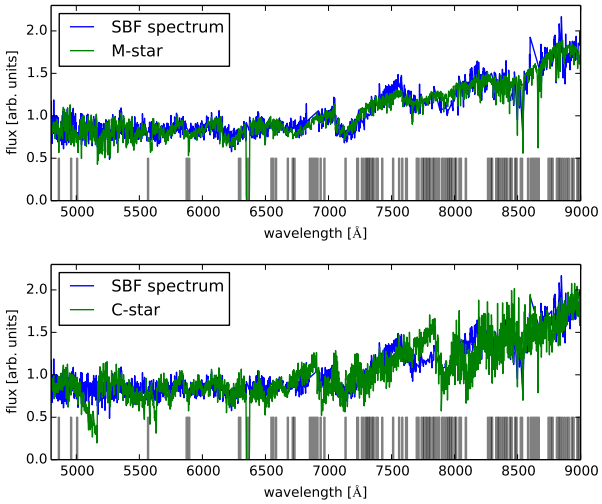

Figure 5.4: The SBF spectrum of NGC 5102 is shown in blue. Top panel: The best-fitting M-type stellar spectrum from the XSL DR1 library is shown in green. Most of the dominant spectral features, including the molecular bands are well represented by the M-type stellar spectrum, meaning that M giants are the dominant type of stars contributing to the SBF signal of this galaxy. Bottom panel: One of the best-fitting C-type spectra from the XSL library is compared to the SBF spectrum. This plot shows that the SBF spectrum of NGC 5102 is not dominated by C-type stars. However, there are some features that are reminiscent of C-stars features. Most prominent the feature between 7600 and 7900 Å. Grey regions are masked sky and emission lines and regions where the XSL spectrum is missing.

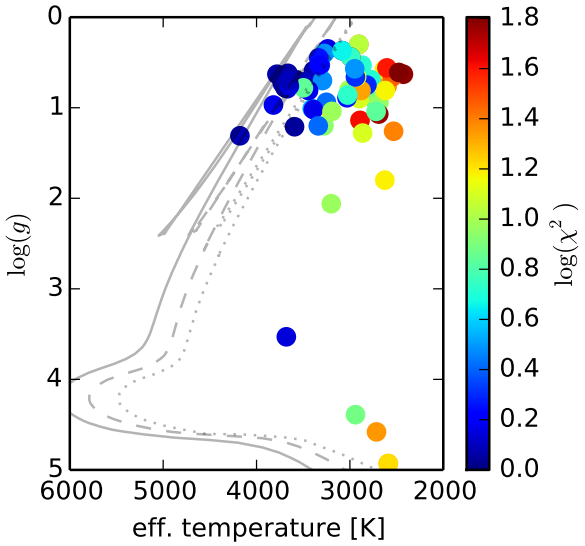

Figure 5.5: For all XSL M-type stars with temperature and surface gravity values their ability to describe the NGC 5102 SBF spectrum is shown in terms of $\chi^2_{\rm red}$. To guide the eye we plot in grey the 10 Gyr old isochrones with [Fe/H] of -0.5 (solid line), 0.0 (dashed line) and +0.5 (dotted line). This plot reveals that a warm M-giant is the best-fitting type of star to the SBF spectrum of NGC 5102.

The coefficients a_i of the multiplicative Legendre polynomial are determined such that the $\chi^2_{\rm red}$ is minimized. We find that $n = 11$ is needed to correct continuum differences between the observational SBF spectrum and the XSL stellar spectra. The error ε in equation 5.7 is a smoothed version of the P_1 spectrum (see equation 5.6), using a 100 pixel running mean for smoothing.

We find that the M-type spectra reproduce the SBF spectrum much better than the C-type spectra. The best-fitting M-type spectrum is shown in Fig. 5.4. All dominant molecular features are very well traced by the M-type stellar spectrum. We emphasize that below 5500 Å the stellar flux is strongly increased by the multiplicative polynomial. In this region the match between the SBF spectrum and the M-type stellar spectrum gets poorer. The best-fitting spectrum from the carbon related XSL spectra is the only S-type spectrum, where C/O = 1.0. In Fig. 5.4 we also show one of the best-fitting C-type spectra. It is immediately obvious that the C-type spectrum provides a much poorer fit to the SBF spectrum. However, some of the features that are not well represented by the M-type spectrum have corresponding features in the C-type stellar spectrum. We therefore fitted a linear combination of the best-fitting M-type and a good fitting C-type spectrum to the SBF spectrum. In a χ^2 sense this fit is only a marginal improve over the M-type spectrum fit. This means that statistically a C-type spectrum is not needed to explain the SBF spectrum of NGC 5102. However, if we assume that there must be C-stars in NGC 5102, than the SBF spectrum allows only for an about 5% luminosity weighted contribution of those stars.

Given that a M-type spectrum is a quite good representation of the SBF spectrum we compute the $\chi^2_{\rm red}$ for all M-type stars for which we have metallicity, effective temperature and surface gravity values. In Fig. 5.5 we plot the $\chi^2_{\rm red}$ as a function of effective temperature and surface gravity. We see that the best-fitting M-type spectra are those of warm giant stars. The temperature of the best-fitting stars are in the range 3500 to 4000 K, the surface gravity is much less constraint. The constraints on the metallicity are even poorer, spectra with $-1.5 \lesssim$ [Fe/H] $\lesssim 0.0$ provide good fits.

5.5 Modelling the SBF spectrum of simple stellar populations

Many stellar population synthesis codes are described in the literature and many authors made their models (e.g. Bruzual & Charlot, 2003; Maraston, 2005; Coelho et al., 2007; Mollá et al., 2009; Vazdekis et al., 2010, 2012) or even their codes (e.g. Leitherer et al., 1999; Le Borgne et al., 2004; Conroy et al., 2009) public. None of these provide model SBF spectrum predictions. Therefore we had to compute our own model predictions. We name our models Stellar Populations for All Applications (SPAA).

5.5.1 Stellar evolution models

We use PARSEC isochrones as input to our stellar population synthesis code. The PARSEC (Bressan et al., 2012) stellar evolution code is a revised version of the former Padova stellar evolution codes. Bressan et al. (2012) update the stellar input physics by using the solar composition from Grevesse & Sauval (1998) with some elemental abundances taken from Caffau et al. (2011). The stellar evolution models are computed for stars in the mass range $0.1 \leq M/M_{\odot} \leq 12$ and with chemical compositions in the range $0.0005 \leq Z \leq 0.06$. The helium abundance of a solar scaled model is computed from the metal abundance Z following $Y = 0.2845 + 1.78Z$. PARSEC traces the stellar evolution from the pre-main-sequence up to the onset of the TP-AGB evolution with the first thermal pulse.

The evolution of TP-AGB stars is traced with the dedicated COLIBRI code (Marigo et al., 2013). The COLIBRI calculations are initialised with the parameters of the PARSEC stellar model at the first thermal pulse. There are two different approaches to modelling TP-AGB evolution: 'full models' that solve the time-dependent equations of stellar structure and 'synthetic models' that use analytic relations (calibrated against full model predictions) to describe the evolution between two thermal pulses. For a discussion of the strengths and weaknesses of both models we refer the reader to Marigo et al. (2013). COLIBRI is somewhere in between, calculating the equation of state, opacities and nuclear reation rates on the fly and using fitting function for e.g. the efficiency of the third dredge-up (for the details we refer to Marigo et al., 2013). We use the COLIBRI PR 16 extension to include the AGB stars in the isochrone predictions (Rosenfield et al., 2016; Marigo et al., 2017). We do not include circumstellar dust predictions in the isochrones.

5.5.2 Stellar spectral libraries

We decided to make use of two stellar spectral libraries: the theoretical library of Coelho (2014) and the observational MILES library (Sánchez-Blázquez et al., 2006).

The theoretical stellar spectral library by Coelho (2014) has been computed with the specific aim to be used for stellar population synthesis models. The library consists of opacity distribution functions, model atmospheres, statistical samples of surface fluxes (SED models) and high-resolution stellar spectra (Coelho, 2014), of which only the high-resolution spectra are of interest for the present project.

We shortly summarize the most important features of the computation and refer the reader to Coelho (2014) for the details. The model atmospheres where computed with the Linux port of the ATLAS9 code (Kurucz, 1970; Sbordone et al., 2004), that assumes plane-parallel geometry and local thermodynamic equilibrium (LTE). For stars cooler than 4000 K pre-computed MARCS (Gustafsson et al., 2008) model atmospheres where used as these compute spherically symmetric model atmospheres (especially important for giant stars) with a larger set of molecular opacities (important for cool stars in general). High-resolution spectra are computed with the Linux port of the SYNTHE code (Kurucz & Avrett, 1981; Sbordone et al., 2004) for the wavelength range $2500 \leq \lambda \leq 9000$ Å.

An important feature of the models is that they are corrected for the effect of predicted lines. Predicted lines are weak absorption lines that mainly affect the pseudo-continuum shape in the blue part of the spectrum. Coelho (2014) uses low-resolution SEDs to correct the continuum of the high-resolution spectra in a differential approach (see Section 4.3.3 for a more detailed description).

The coverage of the $\log(g)$ - $T_{\rm eff}$ plane of this stellar spectral library is not regular as it follows the locus of the isochrones (Coelho, 2014). The limiting range of temperature covered is $3000 \leq T_{\rm eff} \leq 25\,000$ K, the range of surface gravity is $-0.5 \leq \log(g) \leq 5.5$ and four solar scaled chemical compositions are provided for $[{\rm Fe/H}] = [-1, -0.5, 0.0, 0.2]$. All SSP models that are based on the Coelho (2014) theoretical stellar spectra are labelled SPAA/Coelho in this paper. The same stellar spectra are also used in a forthcoming paper by Coelho (priv. com.) to predict SSP spectra.

We also use the observational MILES stellar spectral library (Sánchez-Blázquez et al., 2006) as input for our SSP model spectra. The MILES stellar spectral library consists of 985 stars, where the selection of stars is optimised for stellar population synthesis. The stars were observed with the 2.5 m Isaac New-

ton Telescope and the covered wavelength range is $3525 \leq \lambda \leq 7500$ Å. Special attention has been paid to avoid flux losses due to differential atmospheric refraction and to guarantee a good flux calibration (Sánchez-Blázquez et al., 2006). The spectral resolution of the MILES stellar spectral library has been independently assessed by several authors, consistently finding a FWHM resolution of 2.55 Å (Prugniel et al., 2011; Beifiori et al., 2011; Falcón-Barroso et al., 2011).

The stellar parameters for the stars in the MILES stellar spectral library are derived by Cenarro et al. (2007) following the procedure described in Cenarro et al. (2001). In summary for field stars the parameters are based on an extensive literature search and an iterative procedure to homogenise these values. For cluster stars the three quantities metallicity, temperature and surface gravity are obtained from scaling relations: the metallicity is tied to the metallicity scale of Carretta & Gratton (1997), temperatures are derived from colour–temperature relations (Alonso et al., 1996, 1999) and surface gravities are derived by matching the stars to isochrones (from Girardi et al. (2000)) in the M_V–$T_{\rm eff}$ plane.

We found that the spectra in the MILES library are not scaled to common flux units, meaning that a hot star can have less flux than a cooler star. I decided to follow the flux calibration Prugniel & Soubiran (2001) use for the ELODIE library: they scale the flux of the stars to 1 at 5500 Å. I do the same for all MILES stars. I then multiply with the flux of a theoretical PHOENIX spectrum (Husser et al., 2013) of similar surface gravity, effective temperature and chemical composition at the same wavelength. All SSP models that are based on the empirical MILES stellar spectra are labelled SPAA/MILES in this paper.

5.5.3 Synthesis of single-burst stellar populations

We implemented the widely used isochrone synthesis approach (e.g. Charlot & Bruzual, 1991; Bruzual & Charlot, 2003; Coelho et al., 2007; Conroy et al., 2009; Vazdekis et al., 2010, 2012) to compute the SSP model spectra. The isochrone synthesis approach consists of a summation over all points i of an isochrone of given age t and chemical composition, parametrized by the iron abundance [Fe/H]

$$F_{\rm SSP}(t, [{\rm Fe/H}]) = \sum_i \rho_i(m_i) F([{\rm Fe/H}], T_{{\rm eff},i}, \log(g_i)). \tag{5.9}$$

$F([{\rm Fe/H}], T_{{\rm eff},i}, \log(g_i))$ is the spectrum of a star with the specified parameters, $\rho_i(m_i)$ is the IMF weight, integrated over a small mass interval around m_i

$$\rho_i(m_i) = \int_{m_i - \Delta m_{i,{\rm low}}}^{m_i + \Delta m_{i,{\rm up}}} \xi(\log m)\, {\rm d}\log m \tag{5.10}$$

$$\Delta m_{i,{\rm low}} = \left| \frac{m_i - m_{i-1}}{2} \right|. \tag{5.11}$$

We use a Chabrier (2003) IMF

$$\xi(\log m) = \begin{cases} 0.158 \cdot \exp\left[-\frac{(\log m - \log 0.079)^2}{2 \cdot 0.69^2} \right] & \text{if } \log m \leq 0 \\ 0.0443 \cdot m^{-1.3} & \text{else.} \end{cases} \tag{5.12}$$

5.5.4 Validation of our SSP library

For the validation of our SSP models we use as comparison the MIUSCAT (Vazdekis et al., 2012) SSP library, with a Kroupa (2001) universal IMF and BaSTI isochrones. We had to make the compromise of using a different IMF than Chabrier (2003) for the comparison, because the MIUSCAT models have not implemented this IMF. However, the Kroupa (2001) universal IMF and the Chabrier (2003) one are reasonably similar so that we do not expect these small differences to influence the comparison of the SSP spectra.

In Fig. 5.6 we compare a young 1 Gyr and an old 10 Gyr solar metallicity population of our SPAA/MILES models to the corresponding MIUSCAT and Coelho (priv. com.) SSP models. Fig. 5.7 plots the same comparison for our SPAA/Coelho models. For the 10 Gyr population we see that the residuals are overall small, but some scatter is seen at the blue end. We emphasize that these residuals in the blue part decrease significantly when we compare our SPAA/Coelho model to the Coelho (priv. com.) model and the SPAA/MILES model to the MIUSCAT model. This meas that these residuals are driven by differences in the stellar spectral libraries.

For the 1 Gyr population we see a persistent trend in the residual spectrum continuum slope, with our models predicting higher fluxes in the blue part of the spectrum and lower fluxes in the red part. Also the Balmer lines in the SPAA models are deeper than in the Coelho (priv. com.) model. This trend is seen in the comparison with both SSP libraries, but much stronger for the Coelho (priv. com.) models.

5.5.5 Synthesis of SBF model spectra

The definition of SBF is given in equation 9 of Tonry & Schneider (1988) and reads:

$$\bar{L} = \frac{\sum_i n_i L_i^2}{\sum_i n_i L_i} \tag{5.13}$$

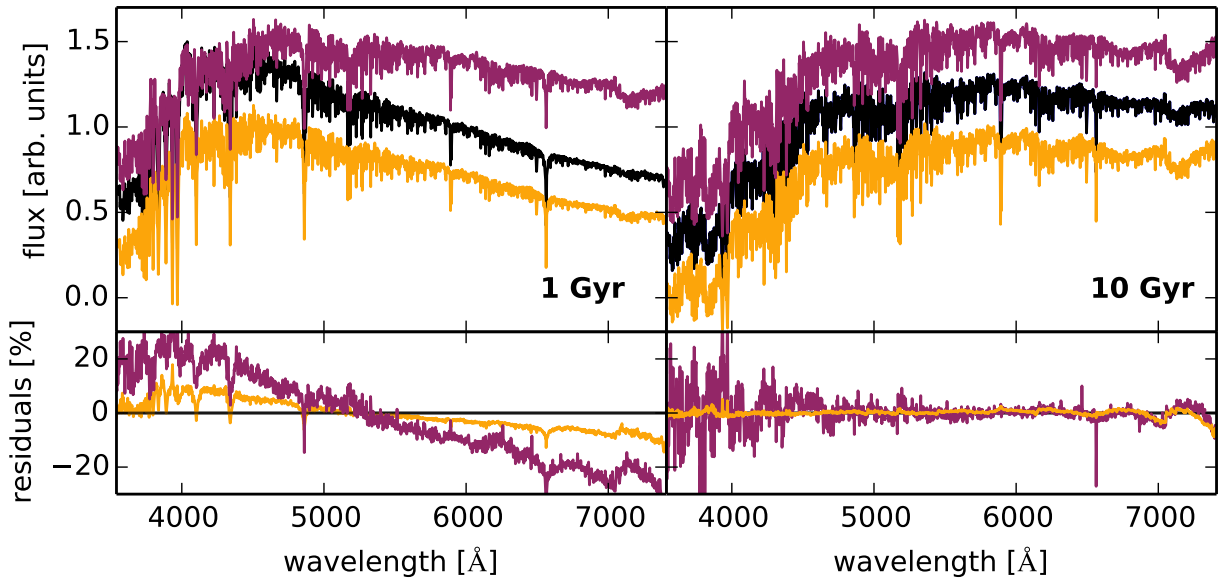

Figure 5.6: Comparison of our SPAA/MILES SSP library (black) to the Coelho (priv. com.) SSP library (violet) and the MIUSCAT SSP library (orange) for two ages. The spectra are convolved to a common resolution of 2.5 Å FWHM and interpolated to a common wavelength grid. The spectra have been normalised with the scalar mean value and for better visibility the Coelho and MIUSCAT spectra are offset by ±0.3 respectively. The bottom panel shows the difference spectrum divided by the SPAA/MILES spectrum, colors are the same as in the upper panels.

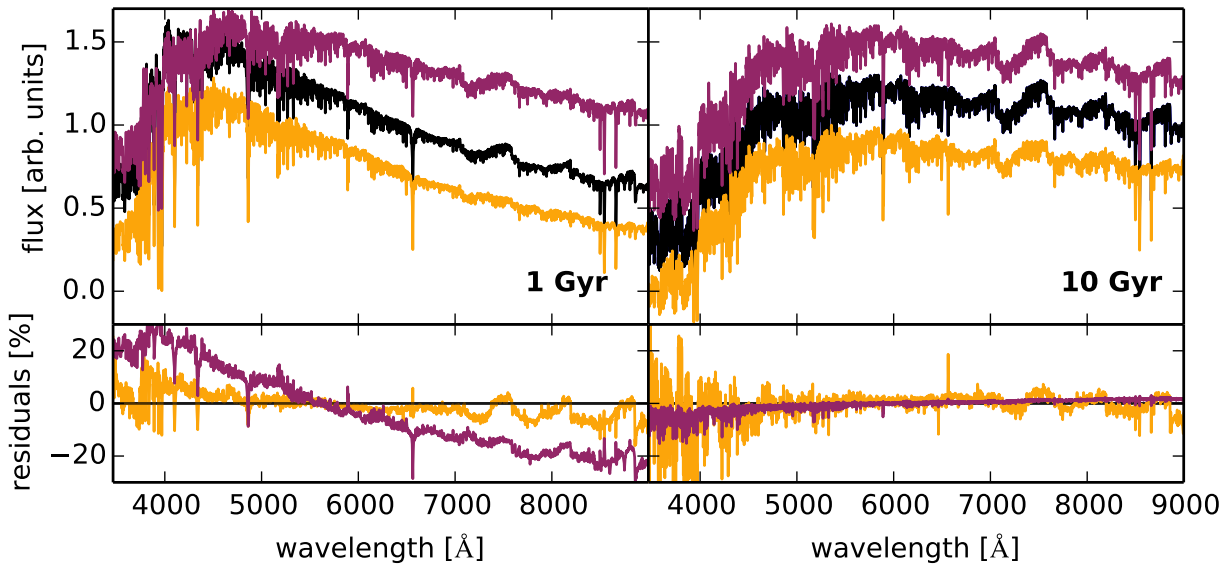

Figure 5.7: The same as Fig. 5.6 but our SPAA/Coelho SSP spectra are compared to the literature models.

where i are the different types of stars, L_i the luminosity and n_i the number of stars of type i. The transition to spectra is simple, by just replacing the luminosity with the spectrum and n can be identified as the IMF weight $\rho_i(m_i)$. Therefore computing theoretical SBF spectra of simple stellar populations is straight forward.

However, SBF spectra of complex stellar populations are no longer linear combinations of the SSP SBF spectra. In order to keep the idea and flexibility of SSPs also in the context of SBF spectra, we compute the numerator and denominator of equation 5.13. The denominator is just the integrated spectrum that we already described in equation 5.9. The numerator is then

$$F^{\rm var}_{\rm SSP}(t,[{\rm Fe/H}]) = \sum_i \rho_i(m_i)\left\{F([{\rm Fe/H}],T_{{\rm eff},i},\log(g_i))\right\}^2. \tag{5.14}$$

We call this the variance spectrum.

Any SBF spectrum with a complex SFH $\omega(t,[Fe/H])$ is then computed from the precomputed libraries via

$$F_{\rm SBF} = \frac{\sum_t \sum_{[Fe/H]} \omega(t,[Fe/H]) F^{\rm var}_{\rm SSP}(t,[{\rm Fe/H}])}{\sum_t \sum_{[Fe/H]} \omega(t,[Fe/H]) F_{\rm SSP}(t,[{\rm Fe/H}])}. \tag{5.15}$$

5.5.6 Testing the influence of different ingredients on the SBF spectrum

In this section we compare the SBF spectra with the integrated spectra and highlight the differences between both diagnostics. The other focus is the comparison of the two different SSP libraries we computed, SPAA/MILES and SPAA/Coelho.

In Fig. 5.8 we show the age evolution of the spectra of a solar metallicity population. By comparing the SBF and the integrated spectra of the same age, we see that the SBF spectrum is dominated by much cooler stars than the integrated spectrum. There are two indicators for that: the pseudo-continuum of the SBF spectrum keeps rising with increasing wavelength, while for the integrated spectra the maximum flux is within the plotted wavelength range. Also the appearance of the molecular features around 7000 Å is an indicator that the stars dominating the SBF spectrum are cooler. This nicely visualises that the SBF spectrum is dominated by the cooler giant stars.

In the previous section we already discussed the differences of the integrated model spectra of the SPAA/Coelho and SPAA/MILES libraries. Here we concentrate on the SBF spectrum. The SPAA/Coelho models predict much stronger molecular features than the SPAA/MILES models. This is tentatively already seen in the integrated spectra, where the SPAA/Coelho models exhibit a molecular absorption dip at $\lambda > 7000$ Å. This is amplified by the SBF spectrum and the different molecular features are visible at lower wavelengths.

The metallicity evolution of a 5 Gyr old stellar population is shown in Fig. 5.9. The metallicity evolution of the SBF spectrum in the SPAA/MILES models is interesting. We see that the molecular features are kicking in at the transition from [Fe/H] $= -1.0$ to -0.5. While also the metal poor population show many metal absorption lines there are no molecular features seen. In the SPAA/Coelho library the transition is much smoother. In accordance with the generally stronger molecular features in the SPAA/Coelho SBF models already the [Fe/H] $= -1$ model has some weak molecular features. With increasing metallicity these become stronger.

This is caused by the fact that with increasing metallicity the giant branch temperature becomes cooler and at some point molecules can form.

In order to quantify the differences between the two models we compare the root mean square (RMS) of the difference spectrum in four different wavelength sections of ~ 1000 Å length. In Fig. 5.10 we plot this for the wavelength range $5500 \leq \lambda \leq 6500$ Å for the integrated and the SBF spectrum. From the comparison of the integrated spectra we see that the RMS increases with increasing age. This is a systematic trends that we observe independently from wavelength. An exception to this are the 1 and 2 Gyr spectra at [Fe/H] $= -1.0$, where the SPAA/Coelho model predicts much stronger molecular bands than the SPAA/MILES models. The best agreement between the two libraries is seen for spectra with [Fe/H] $= -0.5$. In the comparison of the SBF spectra we see similar trends, however, at slightly higher RMS values.

In Fig. 5.10 the residuals increase with the age of the SSP. This might be counter-intuitive when looking at Figs. 5.6 and 5.7. However, in those plots especially the continuum mismatch is dominating. For the limited wavelength interval we are considering here the continuum slope differences are not important. The residuals are mainly driven by differences in the line strengths. For the 1 Gyr integrated spectrum (left panel of Fig. 5.10) the most important mismatch is the Mgb feature, for older populations a blend of a Ca I and a Fe I line at $\sim 6462,7$ Å is the most important difference. These are the single one most important features that drive the RMS in Fig. 5.10. Apart from that small differences in the many metal lines increase with age and increase the noise in the residual spectrum between the SPAA/MILES and the SPAA/Coelho models.

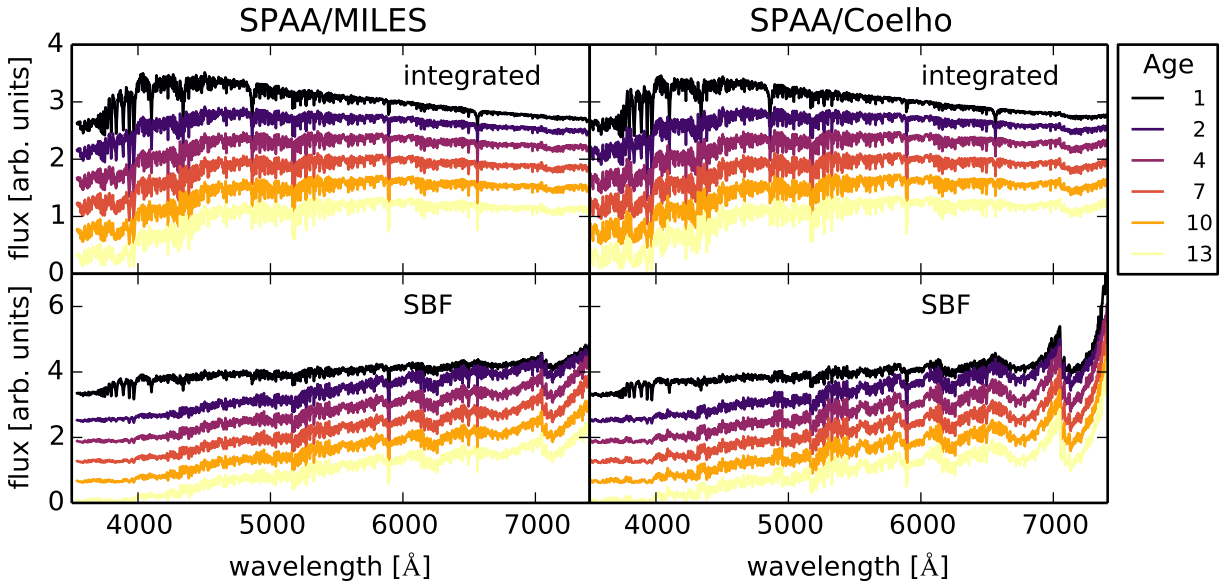

Figure 5.8: The age evolution of the model SSP spectra of a solar metallicity population. The left hand panel shows the SPAA/MILES models, the right hand panel the SPAA/Coelho ones. The top row plots the age evolution of the integrated spectrum, the bottom row the evolution of the SBF spectrum. We find that the SPAA/Coelho library predicts stronger molecular bands than the SPAA/MILES models. The ages are given in Gyr.

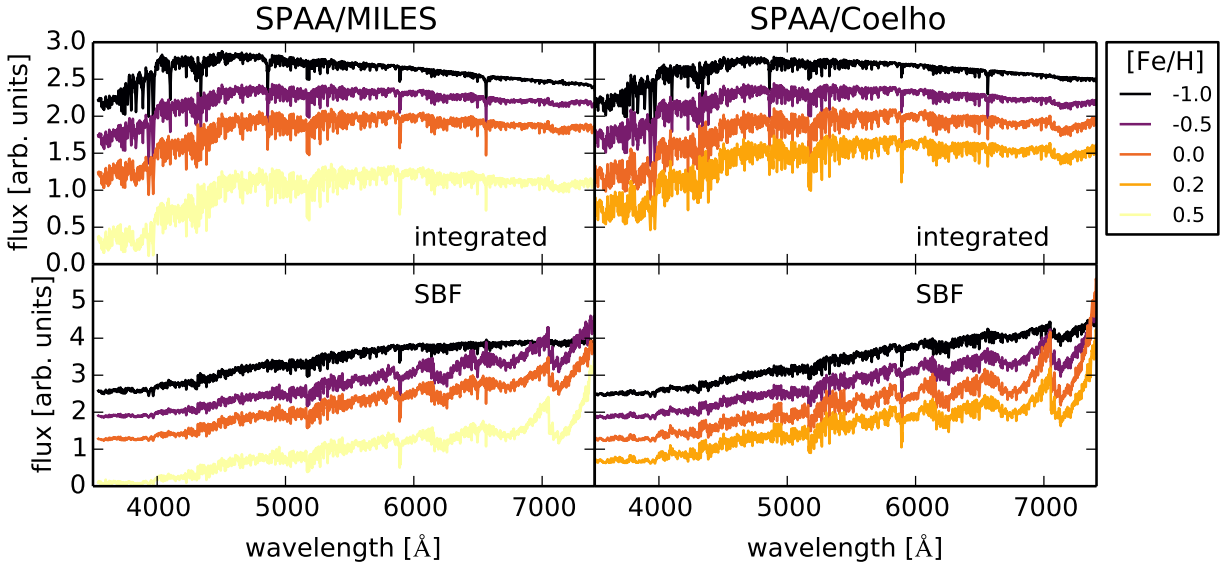

Figure 5.9: Metallicity evolution of a 5 Gyr old stellar population. Panel positions are as in Fig. 5.8. SPAA/MILES models cover the metallicity range $-1.0 \leq [\mathrm{Fe/H}] \leq +0.5$ in steps of 0.5. SPAA/Coelho models have $[\mathrm{Fe/H}] = -1.0, -0.5, +0.0, +0.2$.

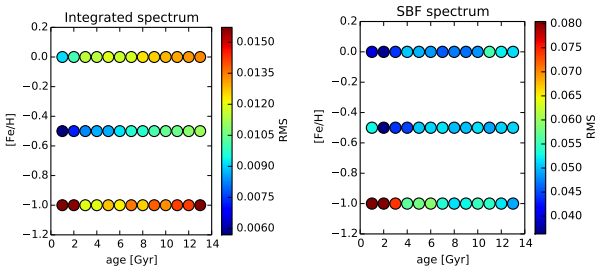

Figure 5.10: Comparison of the SPAA/MILES and the SPAA/Coelho spectral libraries. The colour of the points gives the RMS of the difference spectrum of the two model spectra in the wavelength range $5500 \leq \lambda \leq 6500$ Å. In the left plot we compare the integrated spectra, in the right plot the SBF spectra. The colour scale is truncated at the 95th percentile.

The differences between the SBF spectra (right panel of Fig. 5.10) are mainly caused by stronger molecular features the SPAA/Coelho SSP models predict. The situation is slightly different in the [Fe/H] $= -1$ models. For the 1 and 2 Gyr populations the SPAA/Coelho predicts molecular features, that are not seen in the SPAA/MILES models. For the older populations continuum differences drive the residuals.

We conclude that the integrated spectra agree reasonably well. The SBF spectra exhibit more pronounced differences. As these are the first SBF spectra in the literature we cannot judge which prediction matches better.

5.6 Star formation history determination

In this section we describe the derivation of the star formation history (SFH) and luminosity weighted ages and metallicities for NGC 5102. We start in Section 5.6.1 with fitting the spatially *integrated* spectrum. As explained in Section 5.5.5 complex population SBF spectra are not a linear combination of SSP SBF spectra. This means that standard full spectrum fitting codes cannot be used to fit the SBF spectrum. We therefore explain in Section 5.6.2 how we use the *SBF* spectrum to further constrain the SFH.

5.6.1 Fitting the integrated spectrum

We measure the SFH from a spatially integrated spectrum of NGC 5102. In order to allow a consistent comparison with the SBF spectrum we use the same spatial region that is used in the SBF analysis to compute the integrated spectrum. Therefore we add up the spectra at the unmasked spatial positions [see Fig. 5.1(d)].

We determine the SFH using the full spectrum fitting code PYPARADISE Husemann et al. (2016) an extended PYTHON version of the PARADISE code (Walcher et al., 2015). The determination of the SFH is a two step process: We start with describing the determination of the fiducial best-fit kinematic and SFH solution. Following we describe the bootstrapping to constrain the degeneracy of the SFH.

The initial fit

PYPARADISE starts with logarithmically rebinning the data and template spectra on the same velocity grid. The data spectrum and every template spectrum are individually normalised by their running mean pseudo-continuum. The running mean is computed with a width of 100 pixels, masking the strong absorption/emission lines Hα λ 6563 and Hβ λ 4861, the [S II] emission lines at $\lambda\lambda$ 6716, 6731 and the strong [O I] sky line at λ 5577.

We fit three different wavelength regions of the spectrum: Hβ [4800, 5500], Hα [6100, 6900] and Ca II-triplet [8450, 8800]. The continuum normalisation is derived from a slightly broader wavelength range, we use an additional 150 Å interval on both sides to avoid edge effects. For the fitting we mask nebular and strong sky emission lines. PYPARADISE fits the kinematic and the SFH history successively and iterates this loop. The line-of-sight velocity distribution (LOSVD) is parametrized by a Gaussian and obtained from a Markov-Chain Monte Carlo (MCMC) run, while keeping the SFH fixed. With the best-fit LOSVD the SFH is redetermined via a non-negative least-squares (NNLS) fit. We iterate this loop three times, because tests indicated that this is sufficient to converge to a stable solution. Finally the fiducial best-fit kinematic and SFH solution are saved. The uncertainties in the LOSVD are derived from the final MCMC run. Since we corrected the radial velocity in the data cube during the data reduction the LOSVD is in our case mainly the velocity dispersion. We still do allow for small velocity shifts because different libraries have slightly different wavelength solutions.

Bootstrapping the SFH

The uncertainties and degeneracies in the SFH are determined via a bootstrapping algorithm. We use 5000 bootstraps. In every bootstrap run the input spectrum is disturbed with random errors, assuming Gaussian deviations, with the width given by the error spectrum. The LOSVD is randomly chosen from

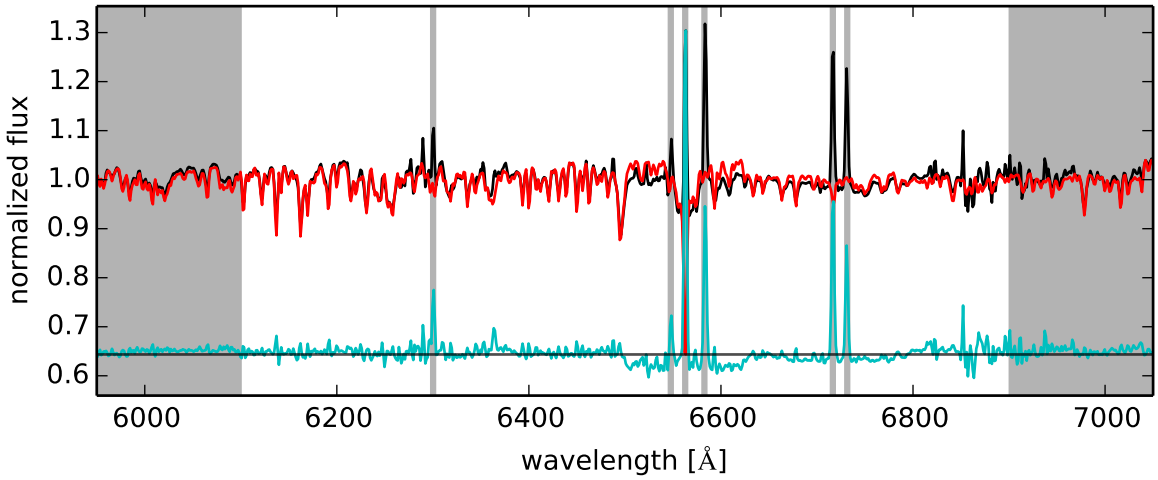

Figure 5.11: The collapsed NGC 5102 MUSE spectrum around the Hα feature is shown in black. The best-fitting combination of SPAA/MILES models is plotted in red. Residuals are plotted in cyan. The grey areas are masked during the fit, nebular lines are not included in the model fit.

the (Gaussian) distribution determined in the fiducial fit. The number of template spectra is randomly reduced to 80% of the input SSP library. In every bootstrap the best-fit SFH is again determined via an NNLS fit, the corresponding weights and the luminosity weighted age and metallicity are saved. We emphasize that by definition all bootstrapped SFHs have the same χ^2-value, i.e. are equally well representing the observed spectrum.

Results from integrated spectrum fitting

With the above detailed strategy we fit the data using our two different sets of SSP-models. For the fit with the SPAA/MILES models we fit only the two intervals Hβ and Hα in common between data and model. For the SPAA/Coelho models we fit all three intervals Hβ, Hα and Ca II-triplet.

Fig. 5.11 shows the fit of the Hα wavelength range with the SPAA/MILES models. The shown fit is a good representation of the observed spectrum. The resulting distribution of light weighted ages and metallicities is shown in Fig. 5.12. In this wavelength interval we measure an age of 2.6±0.3 Gyr and [Fe/H] = -0.3 ± 0.1. These values are in agreement with those measured by Mitzkus et al. (2017) in the same spatial region.

The integrated spectrum fits to the other wavelength intervals and the SPAA/Coelho library are shown in the Appendix in Figs. 5.19 for Hβ with SPAA/MILES and 5.21 for Hβ, 5.23 for Hα and 5.25 for Ca II with SPAA/Coelho. The corresponding 2D distribution of age and metallicity are shown in Figs. 5.20, 5.22, 5.24 and 5.26.

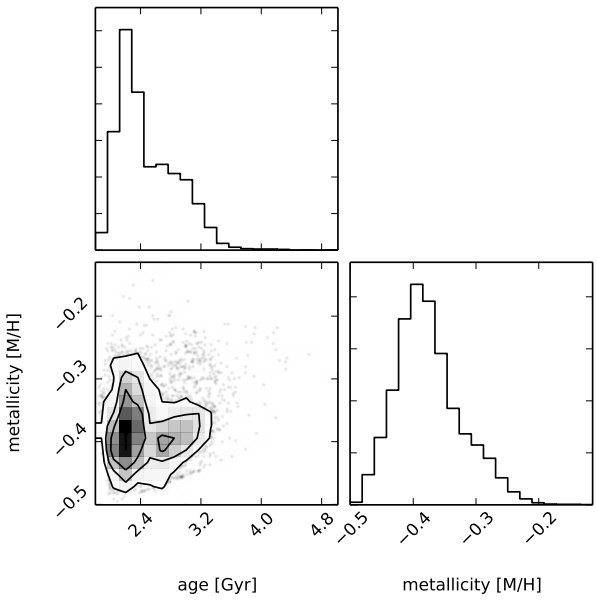

Figure 5.12: The distribution of luminosity weighted ages and metallicities, as obtained by fitting the Hα region with the SPAA/MILES models.

5.6.2 Additional constraints from the SBF spectrum

So far we have only used the *integrated* spectrum to derive the SFH, a technique that is well established. In this section we explain how the SBF spectrum is used to further constrain the SFH.

The bootstrapping provides 5000 different SFHs that all fit the integrated spectrum equally well (in

a χ^2 sense). We now test whether all these models represent the SBF spectrum equally well. Therefore we compute the SBF model spectrum for every of the 5000 bootstraps following equation 5.15 and using the weights assigned to the SSP spectra by pyparadise. We then compute the SBF-spectrum reduced $\chi^2_{\rm red}$ via equation 5.7, where $F_{\rm XSL}$ has been replaced by $F^{\rm SBF}_{\rm model}$. We use a third order multiplicative Legendre polynomial to account for continuum mismatch. In Fig. 5.13 we compare the NGC 5102 SBF spectrum to the best-fitting SBF spectrum model obtained from bootstrapping the Hα wavelength range with the spaa/MILES models.

As already discussed in Section 5.4 the SBF spectrum has in the blue parts a noisy appearance and higher fluxes than the stellar spectra. The slight upturn towards the short wavelength cut-off is also not seen in any of the SSP models (see Fig. 5.13) and mostly accounted for by the multiplicative polynomial. By looking at other SBF model spectrum realisations from the bootstrapping we found that this upturn can even disturb the fit in the red part. Another common feature is that the SBF model flux around the Mgb feature ($\sim$ 5150 to 5200 Å) is lower than observed. We therefore mask the SBF spectrum below 5500 Å for the further analysis.

We stress that we use different wavelength ranges for the fit of the integrated spectrum and computation of the $\chi^2_{\rm red}$ from the SBF spectrum. In Fig. 5.13 for both spectra the masked regions are grey shaded.

For comparison we plot in Fig. 5.14 the model from the same bootstrapping of the *integrated* spectrum that fits the SBF spectrum worst. We recall that by definition both models fit the integrated spectrum equally well and the plotted integrated spectrum models appear quite similar. The differences between the two SBF model spectra in Figs. 5.13 and 5.14 are striking. The worst fitting model predicts too strong molecular bands. The light weighted ages and metallicities for the best (worst) model are however, not drastically different with an age of 3.0 Gyr (3.0) and a metallicity of [Fe/H] = −0.5 (−0.3). Given these significant differences between the two model spectra we hope to better constrain the SFH of NGC 5102 with the additional information from the SBF spectrum.

For the other fit intervals and models we show the best-fitting SBF spectrum with the corresponding integrated spectrum model in the Appendix in Figs. 5.19 for the Hβ interval with spaa/MILES and 5.21 for the Hβ, 5.23 for the Hα and 5.25 for the Ca II interval with spaa/Coelho.

To quantify the SBF spectrum constraints on the SFH we use the $\chi^2_{\rm red}$ to compute the probability that the SBF model spectrum represents the data SBF spectrum. We start with scaling the $\chi^2_{\rm red}$

$$\chi^2_{\rm norm} = {\rm DOF}\frac{\chi^2_{\rm red}}{\min(\chi^2_{\rm red})}. \tag{5.16}$$

The $\min(\chi^2_{\rm red})$ is the minimum $\chi^2_{\rm red}$ in one bootstrap sample. The scaling ensures that the best-fitting model has $\chi^2_{\rm norm}$ = DOF. We use the χ^2-statistic to compute the probability p that, even for a correct model, any observation would have a χ^2 value larger than $\chi^2_{\rm norm}$.

$$p(\chi^2_{\rm norm}, {\rm DOF}) = 1 - P\left(\frac{\rm DOF}{2}, \frac{\chi^2_{\rm norm}}{2}\right) \tag{5.17}$$

$$P(a,x) = \frac{\int_0^x e^{-t}t^{a-1}{\rm d}t}{\int_0^\infty e^{-t}t^{a-1}{\rm d}t} \qquad (a>0) \tag{5.18}$$

In equation 5.18 we are repeating the definition of the incomplete gamma-function, following equations. 6.1.1 and 6.2.1 in Press et al. (1992).

Equipped with the probabilities for the different SFHs we are able to modify the probability distribution of luminosity weighted age and metallicity. In Fig. 5.15 we show the probability distribution obtained by convolving the integrated spectrum bootstrapping PDF (Fig. 5.12) with the SBF spectrum probabilities.

By comparing the two distributions of light weighted ages and metallicities in Fig. 5.12 from the integrated spectrum and in Fig. 5.15 with the additional constraints from the SBF spectrum we see that the 2D distribution is now much more peaked. In the marginalised age distribution the two maxima are now well separated and quite narrow. The marginalised metallicity distribution has a number of maxima.

For the other fits we show the comparison of the two distributions (integrated spectrum bootstrapping and additional SBF constraints) in the Appendix in Figs. 5.20 for the Hβ interval with spaa/MILES and in 5.22 for the Hβ, 5.24 for the Hα and 5.26 for the Ca II interval with spaa/Coelho.

5.7 Discussion

5.7.1 M and C stars in the SBF spectrum

Stellar population models predict that the SBFs are caused by giant stars (e.g. Liu et al., 2000) and the agreement of observed magnitudes and models supports this view. In this work we show for the first time that the SBF spectrum is mainly a pure giant star spectrum, dominated by M-type giants.

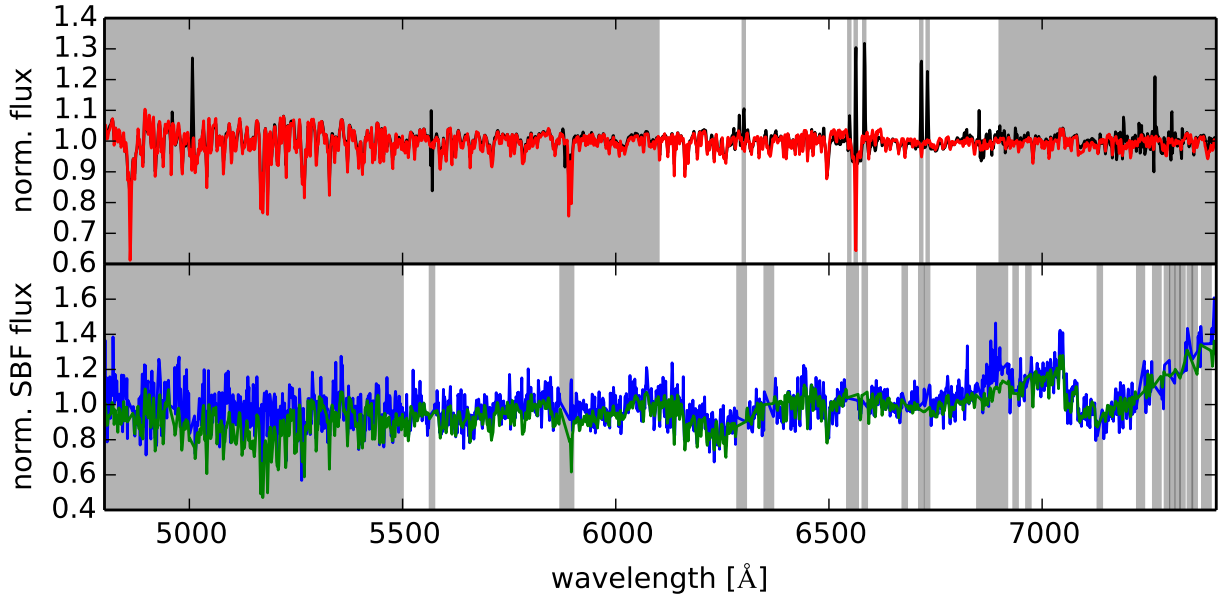

Figure 5.13: The best-fitting SBF model spectrum from the bootstrapping sample SFHs of the Hα wavelength range is compared to the data. In the top panel the integrated NGC 5102 spectrum is shown in black with the integrated spectrum model shown in red. In the bottom panel the NGC 5102 SBF spectrum is shown in blue and the best-fitting SBF model in green. Gray regions are masked during the fit/χ^2 computation.

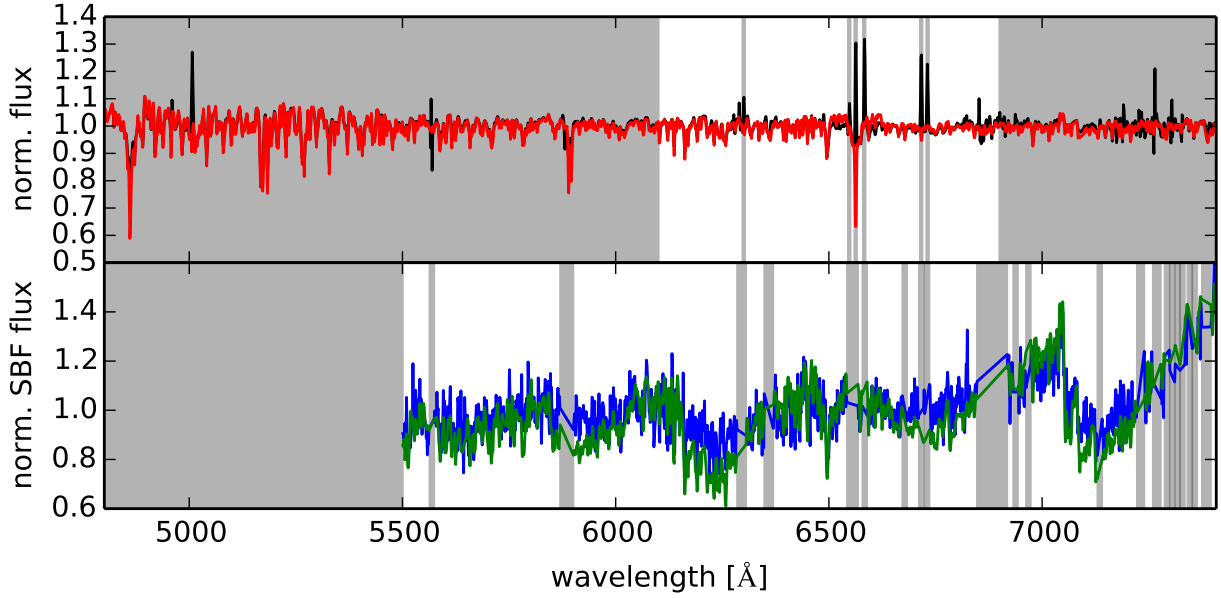

Figure 5.14: As Fig. 5.13, but for the bootstrapping realisation with the poorest fit of the SBF spectrum.

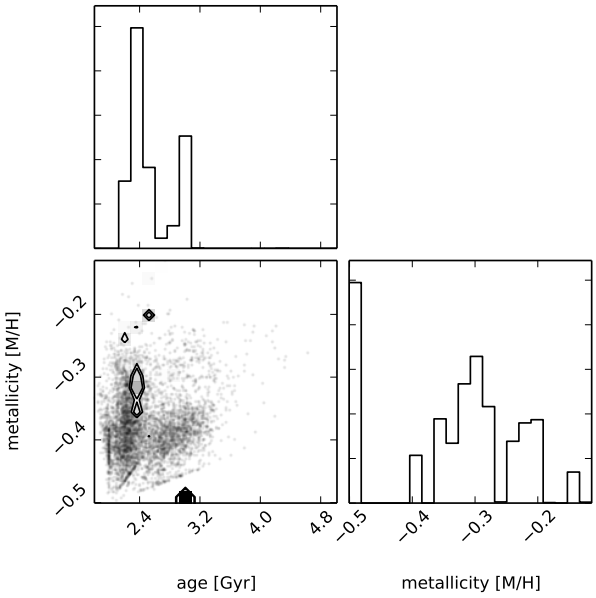

Figure 5.15: The distribution of light weighted ages and metallicities obtained by folding the results from bootstrapping the integrated spectrum with the probabilities from the SBF spectrum comparison.

A surprising finding is that the C-stars contribute at most about 5% percent to the SBF spectrum. For the NGC 5102 population with [Fe/H] ≈ -0.5 the C/M metallicity relation of Cioni & Habing (2003) suggests a ratio of 0.3. The relation by Battinelli & Demers (2005) on the other hand predicts a much smaller ratio C/M = 0.05. These large discrepancies underline once again the uncertainties in our knowledge about TP-AGB stars. C-stars are also expected to be intrinsically brighter than M-type giants, however, it is also unclear to what extend circumstellar dust might obscure the C-stars in the MUSE wavelength range. This complicates the translation of number-count ratios to luminosity ratios. In order to get a better understanding of the C-star population it would be extremely useful to obtain an SBF spectrum in the near infrared, where the dust obscuration is much less of an issue. Also a small number of red super giants could dominate over the C-stars and produce a M-type dominated SBF spectrum.

5.7.2 Lessons learned about the models

Identifying and removing model uncertainties is important because many other conclusions are later based on the results of stellar population synthesis predictions. We computed two model predictions with the same synthesis code, identical isochrones but different stellar spectral libraries. One is based on the observed stellar spectral library MILES (SPAA/MILES), the other one is based on the theoretical stellar spectral library by Coelho (2014) (SPAA/Coelho). In the integrated spectra the main differences are in the young models, where the SPAA/Coelho model seems to be dominated by cooler stars than the SPAA/MILES model. Both of the young SPAA models are cooler than the MIUSCAT models. Apart from that the line strength of the Balmer lines and the discussed Fe I lines (see Figs. 5.6 and 5.7 and Section 5.5.6) are the most deviant spectral features.

The differences in the SBF spectra are more pronounced. Figs. 5.8 and 5.9 reveals that the much stronger molecular absorption bands in the SPAA/Coelho models are the most important difference.

The comparison of the SPAA models to the NGC 5102 spectra reveals that the weaker molecular absorption bands of the SPAA/MILES models fit the SBF spectrum better than the SPAA/Coelho models (see Figs. 5.13, 5.19, 5.21, 5.23). However, the best-fitting SPAA/Coelho model obtained in the Ca II interval (Fig. 5.25) does not over predict the molecular bands in the considered wavelength range.

The SBF spectrum of NGC 5102 is just a single object. In order to put stronger constraints on the models we need more data from galaxies with other mean ages and metallicities. A good test for stellar population models are globular cluster (GC), as these are the objects with the simplest populations we know of. With MUSE SBF spectra can be only obtained for GC in our Galaxy, so the available age range is strongly limited to old populations. Especially the combination of the crowded field spectroscopy (Kamann et al., 2013) and MUSE has offered new means to these tests. Husser et al. (2016) extract spectra for more than 12 000 individual stars in the GC NGC 6397. Such a data set allows a direct comparison of isochrone properties, input spectra, integrated spectra and SBF spectra. To our knowledge such a test has never been done so far.

5.7.3 TP-AGB stars in the stellar population models

In our stellar population models we do not include spectra from carbon rich AGB stars. The reason is that in the observed MILES library no such stars are available and in the theoretical spectral library all stars have solar scaled composition, i.e. have oxygen rich atmospheres. As discussed the ratio of carbon to oxygen stars is not well constraint, but in intermediate-old sub-solar metallicity populations

carbon stars are generally expected. So including these stars is crutial, especially to interpret the SBF spectra, where these stars are amplified.

For the NGC 5102 spectrum we show that carbon stars are not significantly detected. Therefore the use of our population models to interpret the data of this object is justified.

In order to fully exploit the potential of the SBF spectrum to constrain the AGB evolution we would need population models that include stars with C type spectra. The PARSEC isochrone provide the C/O ratio, so this basic information is present. With the spectral libraries the situation is a bit more involved. In observational libraries the AGB phase is typically not well covered over the full parameter range. There are dedicated TP-AGB libraries (Lançon & Mouhcine, 2002) and the upcoming X-shooter spectral library will also include a number of carbon stars (Chen et al., 2014; Gonneau et al., 2016, 2017).

Theoretical stellar libraries provide typically solar scaled or α-element enhanced spectra, i.e. M-type spectra. The modelling of C-type stars is a topic in its own right (Aringer et al., 2009; Nowotny et al., 2011, 2013; Eriksson et al., 2014), so that currently no theoretical library provides both types of spectra. This means that most likely non of the current stellar spectral libraries provides all the information needed. One solution would be to match different libraries. In this discussion we have not even touched the question how valid solar scaled chemical compositions are in modelling AGB stars in general. Another important aspect of AGB evolution is circumstellar dust that can strongly impact the optical spectra of individual stars (González-Lópezlira et al., 2010; Villaume et al., 2015). Therefore the inclusion of detailed TP-AGB spectra in the stellar population models goes beyond the scope of this work. All this underlines that there is significant room for improvements in stellar population models and that SBF spectra provide a good reason to start working on these topics.

5.7.4 Dependence of the age and metallicity on central wavelength and stellar spectral library

As explained we have used (if possible) three different wavelength regions (Hβ, Hα and Ca II-triplet) and two sets of models (SPAA/MILES and SPAA/Coelho) to fit the integrated spectrum and recover the star formation history. In Fig. 5.16 we plot the mean light weighted ages and metallicities from the bootstrapping ensembles of the integrated spectrum fit. The plotted uncertainty intervals are the standard deviation of the bootstrapping ensemble.

There are two things to mention: First the different wavelength intervals that we used give different ages and metallicities. As PYPARADISE normalises the observed spectrum and each template by the running mean, it is not surprising that in different wavelength intervals the mean age and metallicity inferred are different. The second point to mention is that also the different models predict different values. If the models where perfect, this should not happen. Turning this argument around, we find that the models are not yet in agreement.

The full spectrum fitting approach has been validated by different authors. The metallicities recovered by full spectrum fitting are usually found to be in agreement with colour-magnitude diagram studies (Koleva et al., 2008; Zhang et al., 2012; Ruiz-Lara et al., 2015; Kuncarayakti et al., 2016). The recovered ages of galactic Globular Cluster (GC) are sometimes found to bee too young (Zhang et al., 2012), Koleva et al. (2008) attributes this to the presence of blue horizontal branch and blue straggler stars. The results of the full spectrum fitting are dependent on the used stellar library, especially when complex star formation histories are recovered (Koleva et al., 2008; Chen et al., 2010; González Delgado & Cid Fernandes, 2010).

While the full spectrum fitting method and the impact of different stellar libraries has been investigated, we are not aware of studies looking into the question which wavelength range is best suited for the full spectrum fitting. Our results provide a good motivation for such an investigation.

In Fig. 5.17 we plot the mean ages and metallicities obtained from the SHF distributions that include the additional constraints from the SBF fitting. The effect of including the SBF constraints is ambiguous: For the Hβ interval the age discrepancy is reduced, for the Hα interval however, the formerly matching ages are now less concordant.

The fact that the discrepancy between the different wavelength intervals has decreased is to be expected because we always fit the same part of the SBF spectrum. While the integrated spectrum fit did probe different regions, the SBF spectrum probabilities are always derived from the wavelength interval $5500 \leq \lambda \leq 7500$ Å.

5.7.5 Constraining the SFH

In Section 5.6.2 we show that different SFHs that represent the integrated spectrum equally produce at the same time drastically different SBF model spectra. However, in the same section we show that the SBF spectrum does not help to reduce the uncertainty in the derived star formation history of NGC 5102.

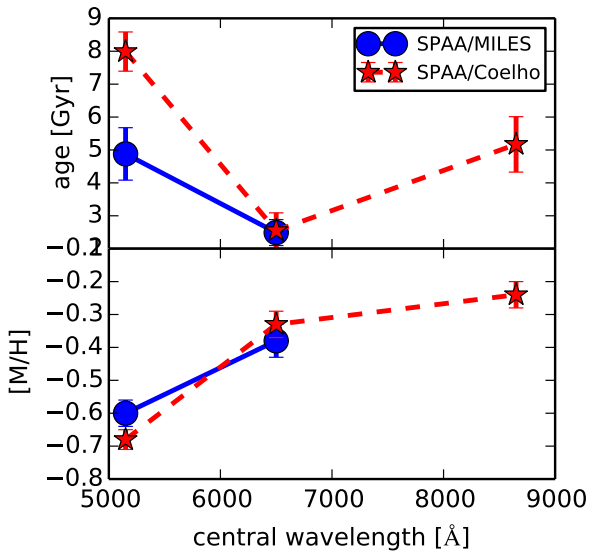

Figure 5.16: We show the mean light weighted ages (top) and metallicities (bottom) obtained from the bootstrapping sample of the integrated spectrum. The fits where done with the two SSP libraries SPAA/MILES (blue dots, solid lines) and SPAA/Coelho (red stars, dashed lines) in up to three different wavelength intervals. Results are shown as a function of the central wavelength of the fitting interval.

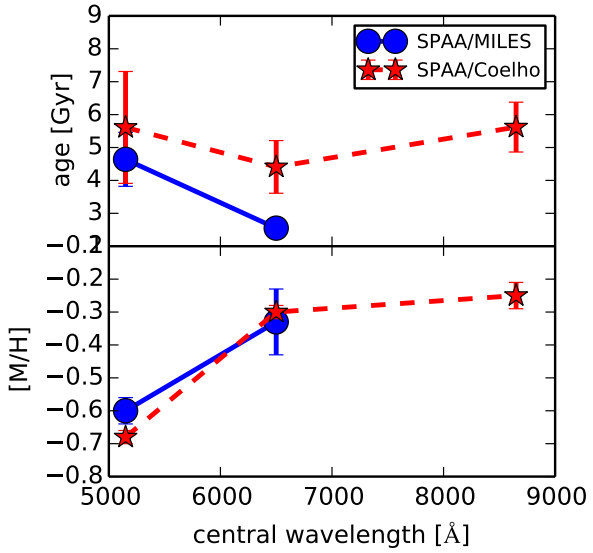

Figure 5.17: We show the mean light weighted ages and metallicities of the combined integrated and SBF spectrum fitting results. Symbols are as in Fig. 5.16.

Therefore we investigated the question if we can expect the SBF spectrum to reduce the spread in the distribution of light weighted mean ages and metallicities. For that we create mock data by using the SPAA/MILES models and two different SFHs: single burst and so called τ-models, i.e. an exponentially declining SHF

$$\mathrm{SFH} \propto \exp(-t/\tau). \tag{5.19}$$

We added Gaussian noise to the mock data with zero mean and dispersion $\varepsilon_{\mathrm{int}} = \langle F(\lambda)\rangle/\mathrm{SNR}$. We assumed that the noise on the SBF spectrum is a factor 10 higher $\varepsilon_{\mathrm{SBF}} = 10 \cdot \varepsilon_{\mathrm{int}}$, roughly the factor we find in our data. We computed a grid of the mock data for different ages/τ-values and SNRs and analysed them with the same code that we used to analyse the MUSE data.

We fit the integrated mock spectrum with the approach detailed in Sections 5.6.1 and 5.6.2. The mean and the standard deviation σ in the light weighted ages and metallicities are computed from the 5000 bootstraps.

We compare the mock SBF spectrum to the bootstrapping results with the method that we described in Section 5.6.2. With the SBF constraints we compute weighted mean ages and metallicities. In Fig. 5.18 we plot the ratio of $\sigma_{\mathrm{SBF}}/\sigma_{\mathrm{int}}$ for the τ-models. From this plot we see that for an SNR ~ 100 in the integrated spectrum (i.e. SNR ~ 10 in the SBF spectrum) the SBF spectrum does not give much additional constraints on the width of the distribution of mean ages. These values are approximately representative for the MUSE data. However, if we increase the SNR (of both spectra!) than the SBF spectrum actually can further narrow down the distribution of ages.

We did the identical analysis with our mock spectra with SSP SFHs. This test leads to the same conclusions and therefore we do not think that this is strongly biased by the assumed SFH.

However, there is an important difference between these mock tests and our observational results. The NGC 5102 SFH distributions that are folded with the SBF constraints are usually quite peaky (see Figs. 5.15, 5.22 and 5.24) and have not much similarity with the original distribution. The exceptions to this are the Hβ wavelength range fitted with the SPAA/MILES models (Fig. 5.20) and the Ca II triplet fitted with the SPAA/Coelho intervals (Fig. 5.26). This is different in our mock models, where the SBF weighted distributions are usually quite similar to those from the bootstrapping of the integrated spectrum. This probably points to problems in the models to reproduce the NGC 5102 SBF spectrum.

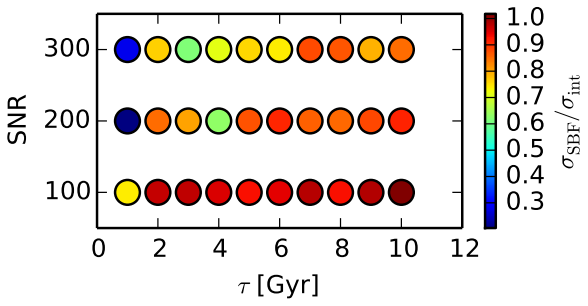

Figure 5.18: For a grid of mock spectra with exponentially declining SFH we investigate whether the SBF spectrum can put stronger constraints on the derived SFH. The colour code of the points gives the ratio of the width of age distribution from bootstrapping the integrated spectrum $\sigma_{\rm int}$ and after convolving this distribution with the probabilities from the SBF spectrum comparison $\sigma_{\rm SBF}$.

5.8 Summary

We have for the first time applied the SBF method to integral field spectroscopy data of the S0 galaxy NGC 5102, observed with the MUSE instrument at the VLT.

We demonstrate that it is possible to apply the SBF method to MUSE data and to obtain SBF *spectra*. To our knowledge this is the first SBF spectrum of a galaxy so far. The complex optics of the MUSE instrument lead to uncertainties in the flux calibration that in the presence of sky lines can prevent SBF measurements. We masked those wavelength regions.

The comparison of the SBF spectra with stellar spectra reveals that M-type giant stars are the strongest contributors to the SBF signal of NGC 5102. A combination of oxigen rich and carbon rich stars does not significantly improve the fit. The light weighted contribution of carbon stars is at most 5%. These are insights into the optical properties of the AGB population that are much more difficult to derive from integrated spectra.

We developed the stellar population synthesis code SPAA that predicts SBF spectra. We have computed SPAA stellar population models in two varieties: based on observed and theoretical stellar spectra. We show that the single burst integrated spectra agree reasonably well.

The SBF spectra reveal that the SPAA models that are based on theoretical spectra predict stronger molecular features. This differences between the population models is hardly seen in the integrated spectrum. This reveals the potential of SBF spectra for highlighting differences in stellar population models. The NGC 5102 SBF spectrum is better represented by the weaker molecular feature models that are based on the observational stellar spectra. To test whether this is generally true we need data from more galaxies, especially over a range of metallicities and ages.

We fit the star formation history of NGC 5102 in three different wavelength regions and with both of our models. The inferred star formation histories do sometimes agree, sometimes they strongly disagree. There are two questions that need to be answered: Why do the two population models disagree on the recovered SFHs? Why do the fit results obtained in different wavelength regions disagree so strongly. Especially the later question is important to understand which spectral region is best suited for population studies.

We investigated whether the SBF spectrum provides some additional constraints on the derived SFHs. From modelling and the NGC 5102 data we find that it is not expected that the SBF spectrum puts tighter constraints on the SFHs.

5.9 Appendix: fit results for different wavelength regions and models

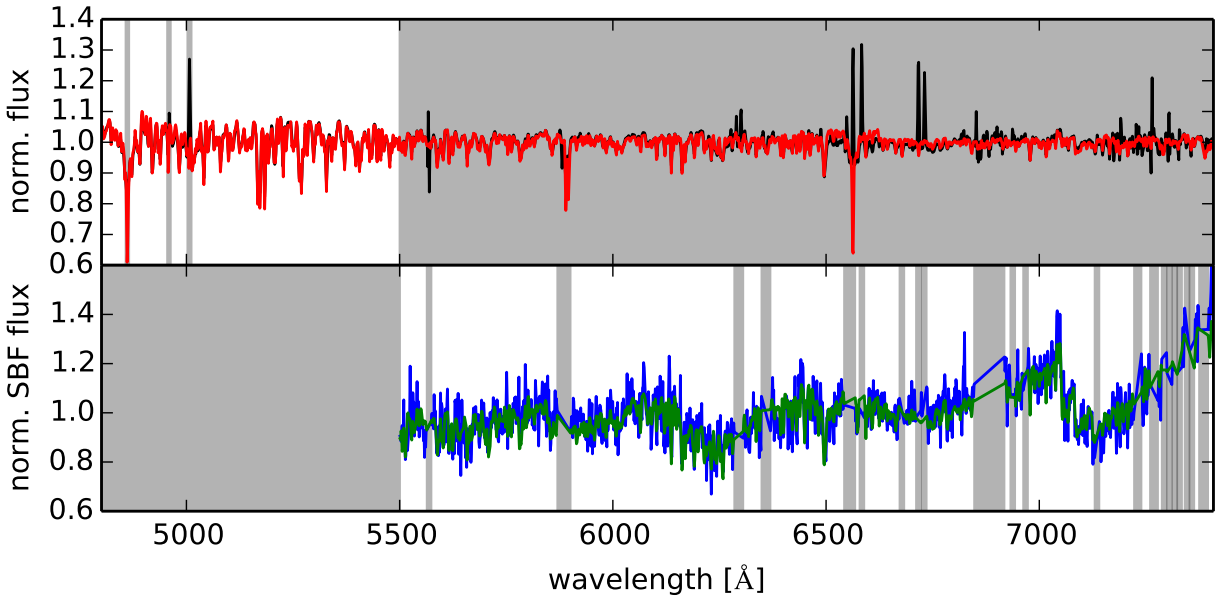

Figure 5.19: The best-fitting SPAA/MILES model SBF spectrum for the Hβ interval is shown. Top panel: The integrated spectrum (black) and the model (red) are plotted. Bottom panel: NGC 5102 SBF spectrum (blue) and the best-fitting SBF model (green) are displayed. Grey regions are masked during the fit/χ^2 computations.

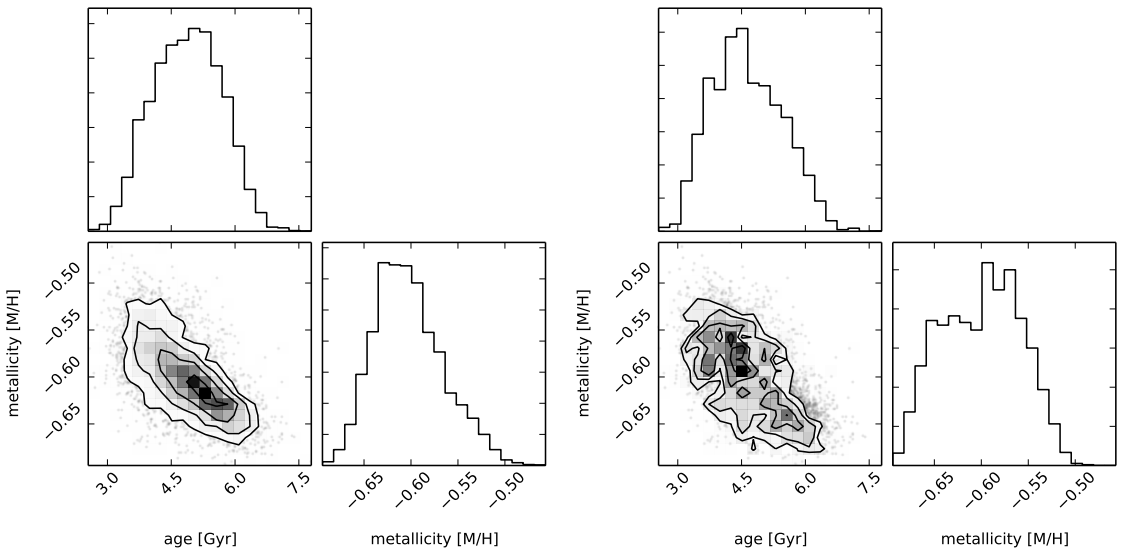

Figure 5.20: Left: The distribution of light weighted ages and metallicities obtained by fitting the Hβ wavelength region with the SPAA/MILES models. Right: The distribution shown in the left panel folded with the probabilities from the SBF spectrum comparison.

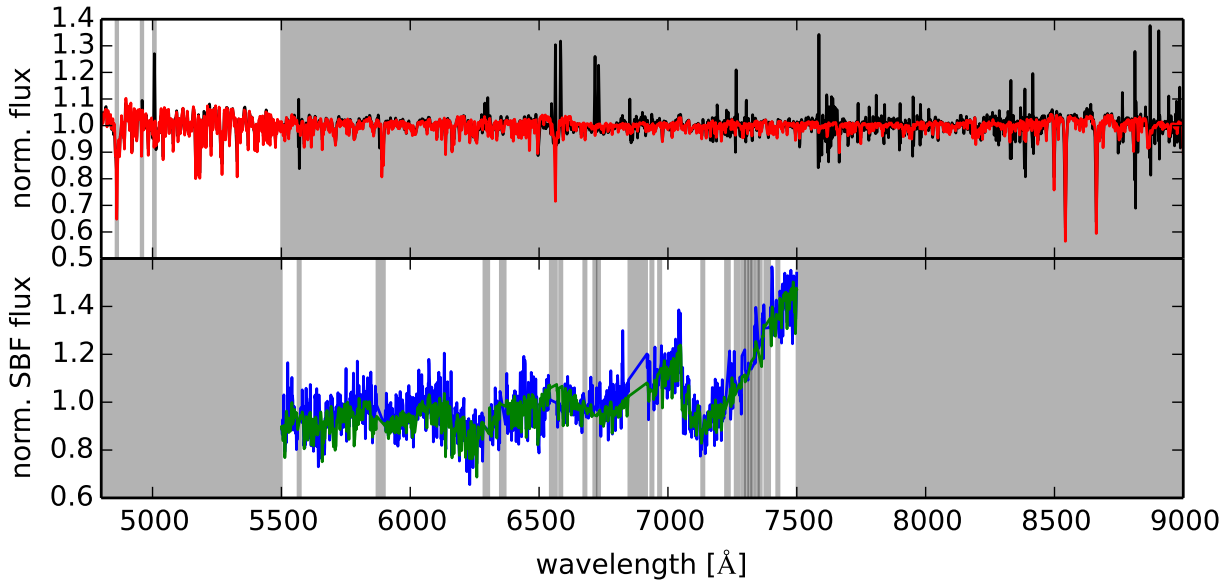

Figure 5.21: The best-fitting SPAA/Coelho model SBF spectrum for the Hβ interval is shown. Panels as in Fig. 5.19

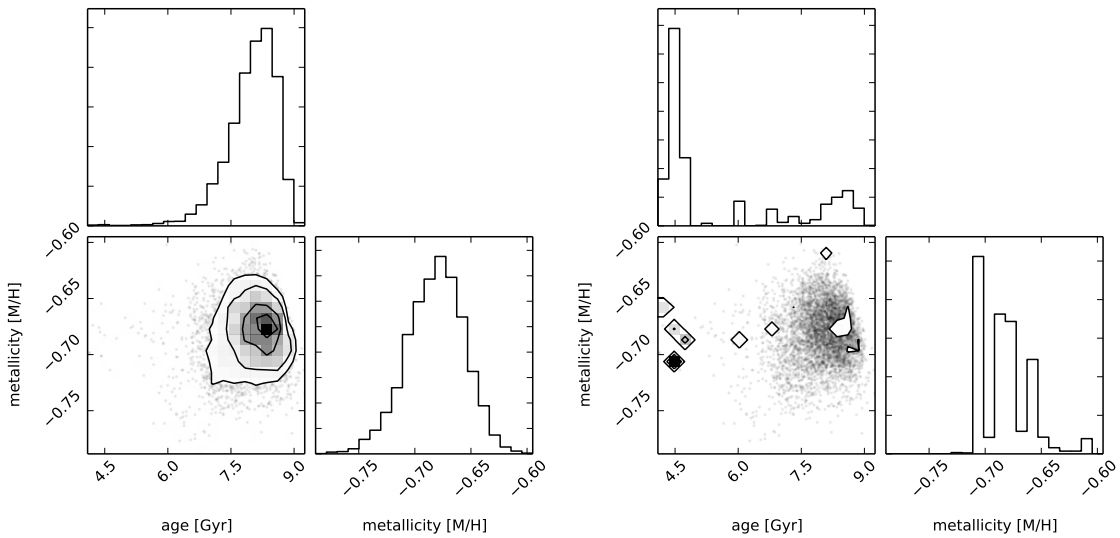

Figure 5.22: Like Fig. 5.20 but for the Hβ wavelength region fitted with the SPAA/Coelho models

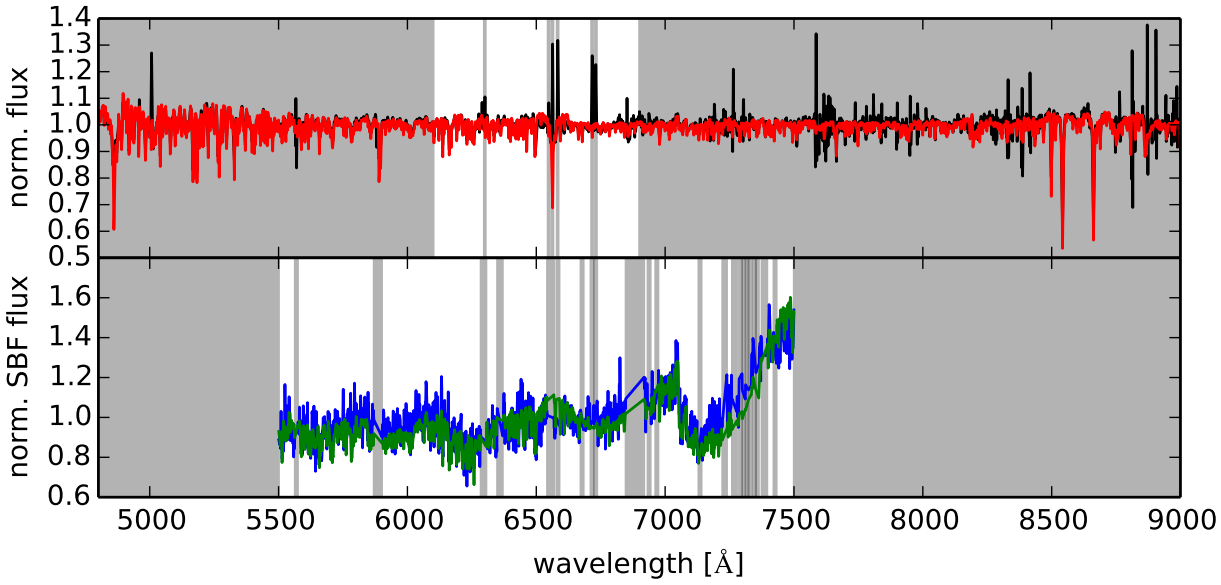

Figure 5.23: The best-fitting SPAA/MILES model SBF spectrum for the Hα interval is shown. Panels as in Fig. 5.19

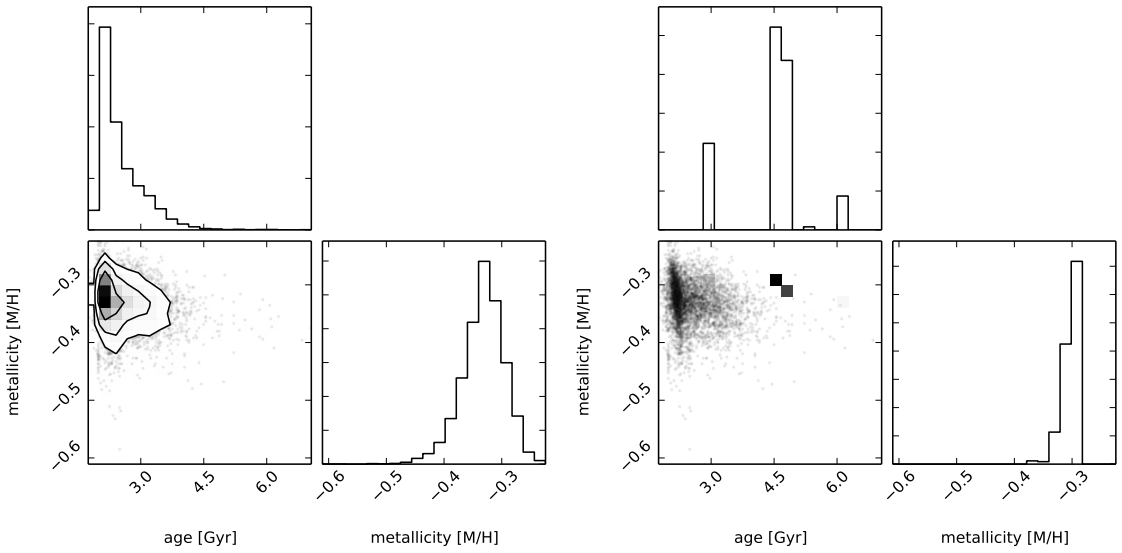

Figure 5.24: Like Fig. 5.20 but for the Hα wavelength region fitted with the SPAA/Coelho models

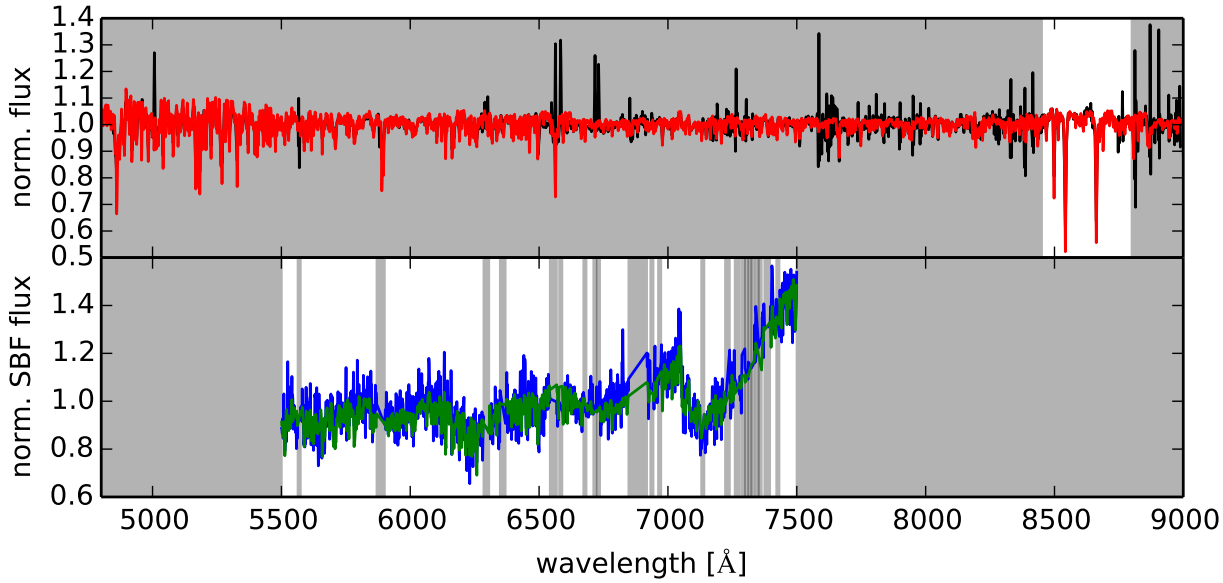

Figure 5.25: The best-fitting SPAA/MILES model SBF spectrum for the Ca II interval is shown. Panels as in Fig. 5.19

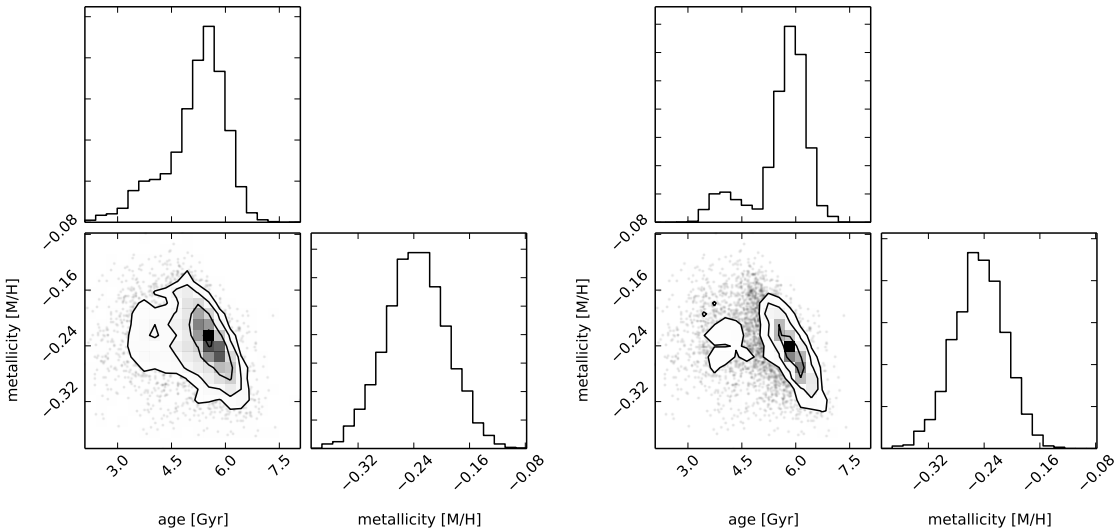

Figure 5.26: Like Fig. 5.20 but for the Ca II triplet wavelength region fitted with the SPAA/Coelho models.

Acknowledgements

This work is based on observations collected at the European Organisation for Astronomical Research in the Southern Hemisphere under ESO programme 60.A-9308(A). We thank Oliver Rieger for implementing the linear spectrum interpolation routine. MM is grateful for financial support from the Leibniz Graduate School for Quantitative Spectroscopy in Astrophysics, a joint project of the Leibniz Institute for Astrophysics Potsdam (AIP) and the Institute of Physics and Astronomy of the University of Potsdam (UP). CJW acknowledges support through the Marie Curie Career Integration Grant 303912.

Bibliography

Ajhar E. A., Tonry J. L., 1994, ApJ, 429, 557
Alonso A., Arribas S., Martinez-Roger C., 1996, A&A, 313, 873
Alonso A., Arribas S., Martínez-Roger C., 1999, A&AS, 140, 261
Aringer B., Girardi L., Nowotny W., Marigo P., Lederer M. T., 2009, A&A, 503, 913
Bacon R., et al., 2010, in Society of Photo-Optical Instrumentation Engineers (SPIE) Conference Series. p. 773508, doi:10.1117/12.856027
Battinelli P., Demers S., 2005, A&A, 434, 657
Beaulieu S. F., Freeman K. C., Hidalgo S. L., Norman C. A., Quinn P. J., 2010, AJ, 139, 984
Beifiori A., Maraston C., Thomas D., Johansson J., 2011, A&A, 531, A109
Bressan A., Marigo P., Girardi L., Salasnich B., Dal Cero C., Rubele S., Nanni A., 2012, MNRAS, 427, 127
Bruzual G., Charlot S., 2003, MNRAS, 344, 1000
Caffau E., Ludwig H.-G., Steffen M., Freytag B., Bonifacio P., 2011, Sol. Phys., 268, 255
Cantiello M., Raimondo G., Brocato E., Capaccioli M., 2003, AJ, 125, 2783
Cappellari M., Copin Y., 2003, MNRAS, 342, 345
Carretta E., Gratton R. G., 1997, A&AS, 121
Cenarro A. J., Gorgas J., Cardiel N., Pedraz S., Peletier R. F., Vazdekis A., 2001, MNRAS, 326, 981
Cenarro A. J., et al., 2007, MNRAS, 374, 664
Chabrier G., 2003, PASP, 115, 763
Charlot S., Bruzual A. G., 1991, ApJ, 367, 126
Chen Y., 2013, PhD thesis, University of Groningen
Chen X. Y., Liang Y. C., Hammer F., Prugniel P., Zhong G. H., Rodrigues M., Zhao Y. H., Flores H., 2010, A&A, 515, A101
Chen Y.-P., Trager S. C., Peletier R. F., Lançon A., Vazdekis A., Prugniel P., Silva D. R., Gonneau A., 2014, A&A, 565, A117
Cioni M.-R. L., 2009, A&A, 506, 1137
Cioni M.-R. L., Habing H. J., 2003, A&A, 402, 133
Coelho P. R. T., 2014, MNRAS, 440, 1027
Coelho P., Bruzual G., Charlot S., Weiss A., Barbuy B., Ferguson J. W., 2007, MNRAS, 382, 498
Conroy C., Gunn J. E., White M., 2009, ApJ, 699, 486
Davidge T. J., 2008, AJ, 135, 1636
Davidge T. J., 2015, ApJ, 799, 97
Deharveng J.-M., Jedrzejewski R., Crane P., Disney M. J., Rocca-Volmerange B., 1997, A&A, 326, 528
Dunn L. P., Jerjen H., 2006, AJ, 132, 1384
Eggen O. J., 1971, QJRAS, 12, 305
Eminian C., Kauffmann G., Charlot S., Wild V., Bruzual G., Rettura A., Loveday J., 2008, MNRAS, 384, 930
Eriksson K., Nowotny W., Höfner S., Aringer B., Wachter A., 2014, A&A, 566, A95
Falcón-Barroso J., Sánchez-Blázquez P., Vazdekis A., Ricciardelli E., Cardiel N., Cenarro A. J., Gorgas J., Peletier R. F., 2011, A&A, 532, A95
Feast M. W., Abedigamba O. P., Whitelock P. A., 2010, MNRAS, 408, L76
Fortney J. J., 2012, ApJ, 747, L27
Gallagher J. S., Faber S. M., Balick B., 1975, ApJ, 202, 7
Girardi L., Bressan A., Bertelli G., Chiosi C., 2000, A&AS, 141, 371
Gonneau A., et al., 2016, A&A, 589, A36
Gonneau A., et al., 2017, A&A, 601, A141
González Delgado R. M., Cid Fernandes R., 2010, MNRAS, 403, 797
González-López lira R. A., Bruzual-A. G., Charlot S., Ballesteros-Paredes J., Loinard L., 2010, MNRAS, 403, 1213
Grevesse N., Sauval A. J., 1998, Space Sci. Rev., 85, 161
Gustafsson B., Edvardsson B., Eriksson K., Jørgensen U. G., Nordlund Å., Plez B., 2008, A&A, 486, 951
Herwig F., 2005, ARA&A, 43, 435
Husemann B., Bennert V. N., Scharwächter J., Woo J.-H., Choudhury O. S., 2016, MNRAS, 455, 1905
Husser T.-O., Wende-von Berg S., Dreizler S., Homeier D., Reiners A., Barman T., Hauschildt P. H., 2013, A&A, 553, A6
Husser T.-O., et al., 2016, A&A, 588, A148
Jensen J. B., Tonry J. L., Luppino G. A., 1998, ApJ, 505, 111
Jensen J. B., Tonry J. L., Thompson R. I., Ajhar E. A., Lauer T. R., Rieke M. J., Postman M., Liu M. C., 2001, ApJ, 550, 503
Jensen J. B., Blakeslee J. P., Gibson Z., Lee H.-c., Cantiello M., Raimondo G., Boyer N., Cho H., 2015, ApJ, 808, 91

Kacharov N., Rejkuba M., Cioni M.-R. L., 2012, A&A, 537, A108
Kamann S., Wisotzki L., Roth M. M., 2013, A&A, 549, A71
Karachentsev I. D., et al., 2002, A&A, 385, 21
Koleva M., Prugniel P., Ocvirk P., Le Borgne D., Soubiran C., 2008, MNRAS, 385, 1998
Kroupa P., 2001, MNRAS, 322, 231
Kuncarayakti H., Galbany L., Anderson J. P., Krühler T., Hamuy M., 2016, A&A, 593, A78
Kurucz R. L., 1970, SAO Special Report, 309
Kurucz R. L., Avrett E. H., 1981, SAO Special Report, 391
Lançon A., Mouhcine M., 2002, A&A, 393, 167
Le Borgne D., Rocca-Volmerange B., Prugniel P., Lançon A., Fioc M., Soubiran C., 2004, A&A, 425, 881
Leitherer C., et al., 1999, ApJS, 123, 3
Liu M. C., Charlot S., Graham J. R., 2000, ApJ, 543, 644
Liu M. C., Graham J. R., Charlot S., 2002, ApJ, 564, 216
Maraston C., 2005, MNRAS, 362, 799
Marigo P., Bressan A., Nanni A., Girardi L., Pumo M. L., 2013, MNRAS, 434, 488
Marigo P., et al., 2017, ApJ, 835, 77
McMillan R., Ciardullo R., Jacoby G. H., 1994, AJ, 108, 1610
Mei S., et al., 2005, ApJS, 156, 113
Mitzkus M., Cappellari M., Walcher C. J., 2017, MNRAS, 464, 4789
Mollá M., García-Vargas M. L., Bressan A., 2009, MNRAS, 398, 451
Nowotny W., Aringer B., Höfner S., Lederer M. T., 2011, A&A, 529, A129
Nowotny W., Aringer B., Höfner S., Eriksson K., 2013, A&A, 552, A20
Pahre M. A., Mould J. R., 1994, ApJ, 433, 567
Pahre M. A., et al., 1999, ApJ, 515, 79
Press W. H., Teukolsky S. A., Vetterling W. T., Flannery B. P., 1992, Numerical Recipes in C: The Art of Scientific Computing, 2nd edn. Cambridge University Press
Pritchet C., 1979, ApJ, 231, 354
Prugniel P., Soubiran C., 2001, A&A, 369, 1048
Prugniel P., Vauglin I., Koleva M., 2011, A&A, 531, A165
Raimondo G., 2009, ApJ, 700, 1247
Raimondo G., Brocato E., Cantiello M., Capaccioli M., 2005, AJ, 130, 2625
Rosenfield P., Marigo P., Girardi L., Dalcanton J. J., Bressan A., Williams B. F., Dolphin A., 2016, ApJ, 822, 73
Ruiz-Lara T., et al., 2015, A&A, 583, A60
Sánchez-Blázquez P., et al., 2006, MNRAS, 371, 703
Sbordone L., Bonifacio P., Castelli F., Kurucz R. L., 2004, Memorie della Societa Astronomica Italiana Supplementi, 5, 93
Scheuer P. A. G., 1957, Proceedings of the Cambridge Philosophical Society, 53, 764
Sodemann M., Thomsen B., 1996, AJ, 111, 208
Taylor E. N., et al., 2011, MNRAS, 418, 1587
Tonry J. L., 1991, ApJ, 373, L1
Tonry J., Schneider D. P., 1988, AJ, 96, 807
Tonry J. L., Blakeslee J. P., Ajhar E. A., Dressler A., 1997, ApJ, 475, 399
Tonry J. L., Dressler A., Blakeslee J. P., Ajhar E. A., Fletcher A. B., Luppino G. A., Metzger M. R., Moore C. B., 2001, ApJ, 546, 681
Tully R. B., Libeskind N. I., Karachentsev I. D., Karachentseva V. E., Rizzi L., Shaya E. J., 2015, ApJ, 802, L25
Vazdekis A., Sánchez-Blázquez P., Falcón-Barroso J., Cenarro A. J., Beasley M. A., Cardiel N., Gorgas J., Peletier R. F., 2010, MNRAS, 404, 1639
Vazdekis A., Ricciardelli E., Cenarro A. J., Rivero-González J. G., Díaz-García L. A., Falcón-Barroso J., 2012, MNRAS, 424, 157
Villaume A., Conroy C., Johnson B. D., 2015, ApJ, 806, 82
Walcher C. J., Coelho P. R. T., Gallazzi A., Bruzual G., Charlot S., Chiappini C., 2015, A&A, 582, A46
Weilbacher P. M., Streicher O., Urrutia T., Jarno A., Pécontal-Rousset A., Bacon R., Böhm P., 2012, in Society of Photo-Optical Instrumentation Engineers (SPIE) Conference Series. p. 84510B, doi:10.1117/12.925114
Worthey G., 1993, ApJ, 409, 530
Zhang Y., Han Z., Liu J., Zhang F., Kang X., 2012, MNRAS, 421, 1678
Zibetti S., Charlot S., Rix H.-W., 2009, MNRAS, 400, 1181
van Dokkum P. G., Conroy C., 2014, ApJ, 797, 56
van Woerden H., van Driel W., Braun R., Rots A. H., 1993, A&A, 269, 15
van den Bergh S., 1976, AJ, 81, 795

6 Conclusions and outlook

In this thesis MUSE integral field spectroscopy data of the nearby S0 galaxy NGC 5102 were analysed. Measuring the stellar kinematics revealed that NGC 5102 is a 2σ galaxies that hosts two counter rotating stellar discs. Modelling the kinematics I discovered that this galaxy is dark matter dominated at all radii. The total matter density slope of this galaxy is shallower than in more massive galaxies, confirming a trend of decreasing slop with decreasing stellar mass. I used the same data-set to measure the first Surface Brightness Fluctuation (SBF) spectrum from a galaxy. This spectrum is dominated by giant stars of spectral type M, the expected signatures of carbon rich stars are not seen. I showed that dedicated stellar population models are able to reproduce the SBF spectrum. Important topics for future work are the better modelling of the thermally pulsating asymptotic giant branch star phase and measuring an SBF spectrum of a galaxy with an old population would complement the work presented in this thesis.

6.1 Conclusions

In this thesis I used integral field spectroscopy to probe the stellar population and dynamics of the nearby low-luminosity S0 galaxy NGC 5102. The work consists of two main parts: Firstly, I measured the kinematics and the modelled of the dynamics to infer the gravitational potential of this galaxy. Secondly, I applied the SBF method to integral field spectroscopy and measured the first SBF spectrum.

The stellar dynamics are interesting as they trace the evolution of the mass build-up of a galaxy and its gravitational potential, revealing the dark matter contribution. Studying the kinematics of NGC 5102 from MUSE observations is interesting for two reasons: Firstly, MUSE provides a large field of view with an unprecedented data quality. Secondly, NGC 5102 is a low-mass S0 galaxy that probes a mass that is at the edge of the mass ranges covered by the larger surveys ATLAS^{3D} (Cappellari et al., 2011) and CALIFA (Sánchez et al., 2012). I can therefore test scaling relations obtained from these surveys on a single object, but with very good data quality and I exclude systematic problems with the analysis software that might have been missed in lower-quality data.

The SBF method amplifies the signal of the brightest stars in a population and is therefore well suited to study Red Giant Branch (RGB) and Asymptotic Giant Branch (AGB) stars. So far this has been done using photometry only. However, the information content of SBF magnitudes in a few bands is limited, age metallicity and distance degeneracies limit the usability for population studies. The development of the integral field spectrograph MUSE, that combines a wide $1 \times 1\,\mathrm{arcmin}^2$ field of view with a spatial sampling of 0.2 arcsec allows for the first time to apply the SBF method to Integral Field Spectroscopy (IFS) data. This combines the sensitivity of the SBF method to evolved stars with the physical information content of spectra and enables more detailed population studies.

6.1.1 The dynamics of NGC 5102 reveal: counter rotating discs are embedded in dark halo

We measured the line-of-sight velocity distribution of NGC 5102 from the MUSE data. For the first time these data revealed that the velocity dispersion map exhibits two off-centre peaks along the major axis meaning that NGC 5102 is a 2σ galaxy. The velocity field indicates that the sense of the rotation reverses

towards the outer parts. We were able to kinematically decompose the two counter rotating components and therefore explained the two off-centre peaks in the velocity dispersion with the presence of the counter rotating discs.

Fitting the stellar population of NGC 5102 we found steep age and metallicity gradients in the centre of the galaxy. The galaxy centre is made of younger stars with higher metallicity. It would be very interesting to see if this population gradient is connected to the two counter-rotating stellar discs. However, the spectral resolution of MUSE did not permit this exercise.

Comparing our findings with published H I gas rotation curves we discovered that the gas co-rotates with the central component. This is typically found in counter rotating galaxies, often also the counter rotating disc has a younger age. The open question remains whether this is also true for NGC 5102. Looking at the scaling of the age and metallicity gradients as compared to the rotation map this might well be, however, we could not provide the final proof for this speculation.

We used the stellar kinematics to probe the gravitational potential of NGC 5102 using Jeans Anisotropic Modelling (JAM). We parametrized the stellar mass distribution using the muti-Gaussian expansion method applied to HST imaging data. We prepared two self-consistent JAM models, one with a spatially constant mass-to-light ratio, one with the mass-to-light ratio from the population fitting. None of these models can explain the observed kinematics. The inclusion of a Navarro, Frenk & White (NFW) dark matter (DM) halo immediately solved the strong discrepancies. This is the strongest hint for the need of a DM halo obtained with the JAM method on the basis of a single galaxy so far. The high DM fraction inside one effective radius we inferred for NGC 5102 confirms the trend of increasing DM fraction with decreasing stellar mass.

We investigated the shape of the DM halo by using a generalized NFW halo, that has a free inner halo slope. The results were difficult to interpret, because the Initial Mass Function (IMF), the DM halo slope and the DM fraction are degenerate. However, the indication was that a steeper than NFW halo slope fits the data better. A steeper DM halo leads to an IMF that is lighter than Salpeter, a result that is expected for lower mass galaxies.

A more robust result is the determination of the logarithmic total (i.e. luminous plus dark) matter slope. We found a logarithmic slope of -1.75 ± 0.04, shallower than an isothermal halo with -2. Slightly steeper than isothermal halo slopes have been found with similar methods for higher mass galaxies. Our results strongly confirm a tentative indication that the total mass halo slope gets shallower with decreasing mass.

6.1.2 Stellar population synthesis with SPAA: SBF model spectra

In order to predict SBF spectra I developed the stellar population synthesis code SPAA. There are two objectives for the development of the SPAA code: the first and for this work important objective is to predict SBF spectra, the second is to prepare a tool that is flexible and can be used for other stellar population synthesis tasks and with different input data in the future.

SPAA implements the isochrone synthesis approach. As input I used the PARSEC isochrones, because they provide a detailed modelling of the thermally pulsating Asymptotic Giant Branch (TP-AGB) phase. Two different stellar spectral libraries were used: the observed MILES stellar spectra and the fully theoretical stellar spectral library by Coelho (2014). Because observed as well as theoretical stellar spectral libraries have their own strengths and weaknesses, I decided to use both varieties.

Stellar spectral libraries are sampled more sparsely than the isochrones, so that it is necessary to interpolate the stellar spectral library. I used a novel linear interpolation method to interpolate in the effective temperature surface gravity plane that is fast, but non-standard. My tests indicated that this interpolation works very well, when the input-grid of spectra is sampled sufficiently.

I validated the SPAA results by comparing to two other stellar population libraries, the MIUSCAT and the unpublished Coelho (priv. com.) library. The integrated SPAA Single-burst Stellar Population (SSP) spectra are in good agreement with the models from the other libraries. The only exceptions are the young, 1 and 2 Gyr old, spectra. For these ages SPAA model spectra seem to be hotter than the spectra in the two other libraries. The effect seems to be stronger for SPAA models based on the theoretical spectra by Coelho (2014), than for the SPAA models based on the observed MILES spectra.

The intercomparison of the SPAA spectra revealed differences between the two sets of model SBF spectra (based on observed and on theoretical stellar spectra) that are hardly seen in the integrated spectra. The SSP models that are based on the theoretical spectral library predict generally stronger molecular features than the models that are based on the MILES stars. This confirmed on the one hand that SBF spectra provide new diagnostics to probe stellar population models. On the other hand this clear difference in

the predictions made by the two sets of model spectra can be tested with observations.

6.1.3 SBF spectra: amplifying giants in unresolved populations

The SBF method measures pixel to pixel brightness variations in CCD images of galaxies, caused by the statistical sampling of the stellar population in every pixel. This is a powerful image analysis technique, measuring precise distances and being very sensitive to the most luminous stars. The sensitivity to bright evolved stars, combined with spectral information, provides valuable insights into the RGB and TP-AGB population. To explore this potential I have translated the SBF method from an image analysis to a spectroscopic analysis tool. The wide-field integral field spectrograph MUSE provides imaging spectroscopy and allows to apply the SBF method to these data. To my knowledge this is the first time that the SBF method has been applied to the several thousand pseudo-images of an IFS observation.

MUSE is much more complicated than any imaging instrument, combining 24 identical IFUs and more than 1000 different light paths (in every of the 24 IFUs the light is sliced into 48 pseudo slits). In this thesis I proved that even with such a complex instrument SBF can be measured. I found that only at the positions of strong sky lines the residuals from the image slicer system dominate over the fluctuations from the SBF.

By comparing the NGC 5102 SBF spectrum with stellar spectra I showed that the SBF spectrum is dominated by M-type giant stars. To my knowledge this is the first observational proof that the SBFs are actually caused by giant stars. So far this claim was based on stellar population modelling. Stellar population models predict that a fraction of the TP-AGB stars have carbon rich atmospheres and have spectral type C. I did not find significant contributions of these stars in the SBF spectrum.

This shows that the SBF spectrum amplifies the signal from the RGB and AGB stars. Especially modelling the evolution of TP-AGB stars suffers from large uncertainties. Combining these two facts shows that the SBF spectrum is much better suited for constraining TP-AGB evolution in unresolved stellar populations than an integrated spectrum. Especially the combination of the integrated and the SBF spectrum offers new ways to constrain stellar population models.

I also used stellar population models to compare the NGC 5102 SBF spectrum with proper population models. For integrated spectra the Star Formation History (SFH) is typically derived by a weighted linear combination of SSP models. This approach does not work for the SBF spectrum, because the SBF spectrum of a complex stellar population cannot be represented as a linear combination of SSP models. I therefore decided to take a two step approach: First I derived the SFH on the integrated spectrum, I then used the derived SFH to compute the corresponding SBF spectrum. Since the SFH is degenerate, I employed a bootstrapping to explore the parameter space that is compatible with the observed integrated spectrum. For every SFH I computed an SBF spectrum.

The comparison of the NGC 5102 SBF spectrum with the model SBF spectra revealed that models with weaker molecular features are in better agreement. Typically the SPAA/MILES models predict weaker molecular features, while there are a few SFH realisations where also the SPAA/Coelho SBF models fit the data well. Based on this single object, I concluded that the SPAA/MILES spectra provide the better SBF model spectra.

From the bootstrapping I obtained a distribution of luminosity weighted ages and metallicities. The SBF spectrum provides an additional constraint that I used to reduce the degeneracy of the SFH. However, the SBF spectrum constraints led to peaky, but on average equally broad distributions. Tests with mock spectra indicated that a reduction of the SFH uncertainties cannot be expected. However, the peaky distribution is probably caused by template mismatch. I concluded that the SBF spectrum does not further constrain the star formation history. This result might be expected, as the SBF spectrum is dominated by the brightest stars in the population, but these are typically not representative for the full star formation history.

6.2 Outlook

In this thesis I have shown that it is possible to measure SBF spectra from MUSE data and highlighted how these can be used to investigate the stellar population and test stellar population models. These are just the first steps of exploring this new technique. In the following I mention future directions for the use of SBF spectra.

6.2.1 Testing stellar population models

SBF spectra can also be obtained from Galactic Globular Clusters (GCs). These objects are one of the standard benchmark tests for stellar population synthesis models. For most GCs precise *HST* photo-

metry exists, meaning that precises colour-magnitude diagrams are available. At the same time the crowded field spectroscopy (Kamann et al., 2013) applied to MUSE observations of a GC provides thousands of spectra for stars, with the faintest stars being on the main-sequence (Husser et al., 2016). The same MUSE observation can be used to measure SBF and integrated spectra of the GC.

This amount of data from a single object brings us into a position where we can compare stellar population synthesis predictions simultaneously to CMDs, integrated spectra and SBF spectra. At the same time we can compare the input spectra of the stellar population synthesis code to the individual stellar spectra extracted with the crowded field spectroscopy. This massive model data comparison approach has the potential to pinpoint uncertainties in an unprecedented way.

I found that the luminosity weighted ages and metallicities recovered by fitting different wavelength intervals can be quite different. This would be another topic to investigate. There are at least two ways to investigate this: with the help of mock spectra where the input ingredients are known or by fitting spectra from star clusters and galaxies. Such an investigation could answer key questions: Which wavelength interval is best suited for recovering the parameters of a stellar population? Are the differences in recovered age and metallicity due to the presence of a complex stellar population or is the same effect seen in single burst populations? Also the differences in the age and metallicity obtained with the two different stellar population libraries need further investigation.

6.2.2 Including TP-AGB star spectra in the stellar population models

The sensitivity of SBF to AGB stars has been long known and hence was used to investigate TP-AGB star models (Cantiello et al., 2003; Raimondo et al., 2005; Raimondo, 2009; González-López lira et al., 2010). SBF spectra provide new means to these tests, as much more physical details are encrypted in the spectra than in a few magnitudes and colours. Therefore one important step forward is the inclusion of detailed TP-AGB models in the SBF spectrum models. The treatment of AGB star spectra in published stellar population libraries is inhomogeneous: while the widely used MILES population models (Vazdekis et al., 2010) do not have a special TP-AGB treatment, Conroy et al. (2009) for example include TP-AGB star spectra.

The PARSEC isochrones I use in SPAA provide the atmospheric C/O ratio. The bottleneck are the stellar spectral libraries: the two that are used as input to SPAA do not have spectra of stars with spectral type C. For the observed MILES stars no carbon stars are explicitly marked in the parameter file. However, there is a dedicated library of observed average AGB stars spectra (Lançon & Mouhcine, 2002). The spectra need to be averaged, because individual AGB star spectra are very diverse and not useful for stellar population properties. This library still suffers from an incomplete metallicity sampling. The X-shooter spectral library, once completed, will provide a number of carbon star spectra (Gonneau et al., 2016, 2017) and hopefully advance the situation.

The theoretical stellar spectral libraries compute typically solar scaled chemical compositions and have therefore no C-type stellar spectra. However, there are dedicated theoretical carbon star libraries (Aringer et al., 2009; Nowotny et al., 2011, 2013; Eriksson et al., 2014), but they need to be carefully matched to the main stellar spectral library.

TP-AGB stars have strong stellar winds and mass-loss. This leads to circum-stellar dust shells that can enshroud the star and lead to significant reddening for individual stars. At the same time the absorbed energy will irradiated in the infrared. Therefore also the inclusion of circum-stellar dust is important, especially when interpreting infrared light of galaxies (Villaume et al., 2015).

6.2.3 Future observations

NGC 5102 was observed for this feasibility study, because it has bright SBF in the I-band and is therefore well suited to detect the fluctuations. The bright SBFs are caused by the young population in NGC 5102, meaning that a strong contribution from AGB stars is expected, maybe even red super-giant stars are contributing to the SBF signal. This means that modelling the stellar population of this galaxy is very challenging and so is the interpretation of the measured SBF spectrum. Therefore the next target to obtain SBF spectra from should be one with a purely old stellar population. These old populations are expected to be much less affected by model uncertainties and therefore the interpretation of the measured SBF spectrum should be much easier. The drawback is that in such a galaxy the SBF are fainter, meaning that the observations are more difficult.

Having a target that is easy to observe and one that is assumed to be simple to model, it would be interesting to extend the range of ages and metallicities. Especially the metallicity has a strong influence on the SBF stellar population model spectra. In the range from $-1.0 \leq [\mathrm{Fe/H}] \leq 0.0$ I showed that the strength of the molecular bands increases with metal-

licity. At the same time I showed that the two SPAA models disagree on the strength of the molecular features and the tension is increasing with metallicity. Comparing the models in this range to observations will be an interesting test of the models.

6.2.4 SBF spectra in the infrared

MUSE covers the spectral range from 4750 to 9300 Å. However, many of the interesting molecular features of C-type stars are slightly further in the infrared. Especially the wavelength range up to 2 μm is very interesting. There are many of the CN molecular features in this wavelength range that are typical for the appearance of Carbon stars. Additionally, these stars tend to be even redder than M-type giants and are therefore expected to have a higher signal in the infrared part of the spectrum.

Ground-based SBF measurements in the infrared are limited to about 2 μm, because at longer wavelength the sky brightness starts to become so high that it is impossible to measure SBFs with ground-based telescopes.

Currently there is no IFS instrument operating in the infrared that is comparable to MUSE in terms of field of view and spatial sampling. If the SBF technique can be applied to the much smaller IFS that are currently operating in the infrared is an open question. The other bottleneck are the skylines. Already with the MUSE data it is obvious that the skylines have a severe impact, especially at longer wavelength. To summarise: infrared SBF spectra are scientifically very interesting, but observationally also very challenging to obtain.

Measuring SBF spectra from MUSE data has been a very challenging task. However, the resulting spectrum provides interesting new insights into the giant star population of NGC 5102. These results open up many possibilities for future investigations, like the questions on stellar population synthesis and infrared SBF spectra that I have discussed.

Bibliography

Aringer B., Girardi L., Nowotny W., Marigo P., Lederer M. T., 2009, A&A, 503, 913

Cantiello M., Raimondo G., Brocato E., Capaccioli M., 2003, AJ, 125, 2783

Cappellari M., et al., 2011, MNRAS, 413, 813

Coelho P. R. T., 2014, MNRAS, 440, 1027

Conroy C., Gunn J. E., White M., 2009, ApJ, 699, 486

Eriksson K., Nowotny W., Höfner S., Aringer B., Wachter A., 2014, A&A, 566, A95

Gonneau A., et al., 2016, A&A, 589, A36

Gonneau A., et al., 2017, A&A, 601, A141

González-Lópezlira R. A., Bruzual-A. G., Charlot S., Ballesteros-Paredes J., Loinard L., 2010, MNRAS, 403, 1213

Husser T.-O., et al., 2016, A&A, 588, A148

Kamann S., Wisotzki L., Roth M. M., 2013, A&A, 549, A71

Lançon A., Mouhcine M., 2002, A&A, 393, 167

Nowotny W., Aringer B., Höfner S., Lederer M. T., 2011, A&A, 529, A129

Nowotny W., Aringer B., Höfner S., Eriksson K., 2013, A&A, 552, A20

Raimondo G., 2009, ApJ, 700, 1247

Raimondo G., Brocato E., Cantiello M., Capaccioli M., 2005, AJ, 130, 2625

Sánchez S. F., et al., 2012, A&A, 538, A8

Vazdekis A., Sánchez-Blázquez P., Falcón-Barroso J., Cenarro A. J., Beasley M. A., Cardiel N., Gorgas J., Peletier R. F., 2010, MNRAS, 404, 1639

Villaume A., Conroy C., Johnson B. D., 2015, ApJ, 806, 82

Acknowledgements

Over the last years I have put a lot of afford into this thesis, starting with writing the observing proposal, doing all the work behind the presented results and finally writing the thesis. However I would not be at the point where I am now without the support from many persons.
First and foremost I am very thankful to Jakob Walcher for supervising me. Neither Jakob nor I where experts on surface brightness fluctuations at the beginning of the project, but together we paved the way for spectroscopic SBF. Jakob, you never lost the hope that this project will finally be successful, with your positive statements on the status of the work and the scientific benefits you provided me from time to time a very important motivation to carry on and to bring this project to this state. I also appreciate the regular tea meetings, that helped a lot in discussing day-to-day difficulties and solving all the minor and major problems on the way.
My special thank goes to Martin Roth for initiating this project and his contributions getting it funded. Martin, I will never forget the two observing runs we had at the Calar Alto Observatory. This unique chance to actually do the observations with a large telescope gave me invaluable insights into integral field spectrographs, their raw data and the data reduction. This is important background knowledge for the work I have done.
I thank Lutz Wisotzki and the 'Galaxies and Quasar' group for 'adopting' me and providing a vital and inspiring scientific home to me. I acknowledge the many opportunities to present and discuss my work and the critical questions and the feedback that improved my work. I am grateful to Omar Choudhury for many fruitful discussions and especially for introducing me to PYPARADISE and helping with troubleshooting. I have benefited from Peter Weilbacher's insights about the MUSE data reduction pipeline and his help with the noise data cubes.
I spent three very productive and inspiring months at the Sub-department of Astrophysics at Oxford University. I am very thankful to Michele Cappellari for supervising me during that time, introducing me to the galaxy dynamics topic and all the time he has spent to understand, advise and discuss my work.
Last but not least I thank my family for their continuous support over the last years. Especially my wife Anja for being so patient with me, especially when I was occupied with work and had less time for my family than I wish I had had. I thank my daughter Tabea for her wonderful smiles when I returned home. I am grateful my brothers Andreas and Benjamin and my parents for their various supports.

Erklärung

Gemäß §12 der Promotionsordnung der Mathematisch-Naturwissenschaftlichen Fakultät der Universität Potsdam vom 18. September 2013 erkläre ich, dass diese Arbeit an keiner anderen Hochschule eingereicht sowie selbstständig von mir und nur mit den angegebenen Mitteln angefertigt wurde.

Potsdam, den 4. Oktober 2017